PPPL-4254 PPPL-4254

Passive Spectroscopic Diagnostics for Magnetically-confined Fusion Plasmas

B.C. Stratton, M. Bitter, K.W. Hill,
D.L. Hillis, and J.T. Hogan

July 2007

Prepared for the U.S. Department of Energy under Contract DE-AC02-76CH03073.

Princeton Plasma Physics Laboratory
Report Disclaimers

Full Legal Disclaimer

This report was prepared as an account of work sponsored by an agency of the United States Government. Neither the United States Government nor any agency thereof, nor any of their employees, nor any of their contractors, subcontractors or their employees, makes any warranty, express or implied, or assumes any legal liability or responsibility for the accuracy, completeness, or any third party's use or the results of such use of any information, apparatus, product, or process disclosed, or represents that its use would not infringe privately owned rights. Reference herein to any specific commercial product, process, or service by trade name, trademark, manufacturer, or otherwise, does not necessarily constitute or imply its endorsement, recommendation, or favoring by the United States Government or any agency thereof or its contractors or subcontractors. The views and opinions of authors expressed herein do not necessarily state or reflect those of the United States Government or any agency thereof.

Trademark Disclaimer

Reference herein to any specific commercial product, process, or service by trade name, trademark, manufacturer, or otherwise, does not necessarily constitute or imply its endorsement, recommendation, or favoring by the United States Government or any agency thereof or its contractors or subcontractors.

PPPL Report Availability

Princeton Plasma Physics Laboratory:

http://www.pppl.gov/techreports.cfm

Office of Scientific and Technical Information (OSTI):

http://www.osti.gov/bridge

Related Links:

U.S. Department of Energy

Office of Scientific and Technical Information

Fusion Links

Passive Spectroscopic Diagnostics for Magnetically-Confined Fusion Plasmas

B. C. Stratton[1], M. Bitter[1], K. W. Hill[1], D. L. Hillis[2], and J. T. Hogan[2]

[1]Princeton Plasma Physics Laboratory, Princeton University, Princeton, NJ 08543

[2]Oak Ridge National Laboratory, Oak Ridge, TN 37831

ABSTRACT

Spectroscopy of radiation emitted by impurities and hydrogen isotopes plays an important role in the study of magnetically-confined fusion plasmas, both in determining the effects of impurities on plasma behavior and in measurements of plasma parameters such as electron and ion temperatures and densities, particle transport, and particle influx rates. This paper reviews spectroscopic diagnostics of plasma radiation that are excited by collisional processes in the plasma, which are termed 'passive' spectroscopic diagnostics to distinguish them from 'active' spectroscopic diagnostics involving injected particle and laser beams. A brief overview of the ionization balance in hot plasmas and the relevant line and continuum radiation excitation mechanisms is given. Instrumentation in the soft X-ray, vacuum ultraviolet, ultraviolet, visible, and near-infrared regions of the spectrum is described and examples of measurements are given. Paths for further development of these measurements and issues for their implementation in a burning plasma environment are discussed.

Accepted for publication in Fusion Science and Technology (May 2007).

I. Introduction

A. Overview

Magnetically-confined fusion plasmas, such as those produced by tokamaks, stellarators, reversed-field pinches, and magnetic mirrors, always contain measurable amounts of impurity ions in addition to the ions of hydrogen isotopes or helium which constitute the bulk of the plasma ions. These impurity ions are present due to sputtering and desorption processes involving material surfaces in contact with the edge plasma. These include divertor plates, limiters, the vacuum vessel walls, and radio frequency antennas. The presence of impurities leads to enhanced energy loss from the plasma and to reduction in the density of the bulk plasma ions, which can reduce the fusion reactivity. Thus, spectroscopic measurements of the line and continuum radiation emitted by impurities are important in order to understand and minimize the effects of impurities on plasma performance. Spectroscopy of impurity ions and working gas atoms is also used to measure plasma parameters such as the electron temperature and density, ion temperature, particle transport, and particle influx rates. These spectroscopic measurements play an important role in fusion research.

The subject of this review paper is spectroscopic diagnostics of plasma radiation that is excited by collisional processes in the plasma, which is often termed ‘passive’ spectroscopy to distinguish it from ‘active’ spectroscopy involving injected particle and laser beams. (Active spectroscopy is covered in another paper in this issue.) Line and continuum radiation from hot, magnetically confined, plasmas is emitted over a large wavelength range; for the majority of diagnostic applications it is approximately 0.1-1000 nm (~1-12,000 eV photon energy). This includes the near-infrared, visible, ultraviolet, vacuum ultraviolet, extreme ultraviolet, and soft x-ray regions of the spectrum. These spectral regions are defined as used in this paper in Table I.

Different types of instrumentation are used to make measurements in these regions of the spectrum, and there is overlap near the ends of the wavelength regions. Thus, it is convenient to group the discussion of specific spectroscopic techniques by wavelength region and by measurement technique as it applies to either the core or edge region of the plasma. This approach is used in the organization of this paper. Table II gives an overview of the primary measurement techniques and the quantities measured by each one; the relevant section for each technique is also listed. This review can not discuss all implementations of a particular spectroscopic measurement. Instead, representative examples which illustrate the principle of the measurement are given, along with references to other work. The emphasis is on recent developments and issues for implementation of passive spectroscopic diagnostics on burning plasmas such as the International Thermonuclear Experimental Reactor (ITER).

The remainder of this introduction is devoted to a brief overview of the ionization balance in hot plasmas and the relevant line and continuum radiation excitation mechanisms. This overview is relevant to the spectroscopic techniques discussed in the remainder of this paper and serves to orient the reader. In some cases it is expanded upon later in the discussion of a specific spectroscopic measurement. MKS units are used, except that temperatures are given in electron volts, as is customary in plasma physics. This overview is necessarily brief. The books by Griem[1] and Thorn, Litzén, and Johansson[2] provide good introductions to the general principles of plasma spectroscopy. Much useful specific discussion of the spectroscopy of magnetically confined fusion plasmas is found in the older review articles by Isler[3], de Michellis and Mattioli [4, 5], McWhirter and Summers[6], and Peacock[7, 8].

B. Ionization Balance

Plasma ions are conveniently classified as low-, medium-, or high-Z elements. The working gas ions in most experiments are hydrogen isotopes (hydrogen, deuterium, and tritium) or helium. Typical low-Z impurities are lithium, beryllium, boron, carbon, and oxygen. Carbon originates from graphite tiles used as a wall material in high heat load areas while oxygen is desorbed from surfaces inside the vacuum vessel. Lithium, beryllium, and boron are used to control the edge density by reducing hydrogen ion recycling and also reduce oxygen contamination of the plasma. The most common medium-Z impurities are transition metals, such as iron, chromium, and nickel, which originate from the stainless steel and Inconel alloys used for the vacuum vessel and other components close to the plasma edge. High-Z metals such as molybdenum and tungsten are used in some devices as limiter or divertor materials, and may be used in future burning plasma experiments such as ITER. Other elements can be introduced for diagnostic purposes by gas puffing or laser ablation of solid materials. In present-day experiments, low-Z elements are typically present in concentrations of 1% or more of n_e, while medium- and high-Z elements are present in much smaller concentrations, typically 0.1% or less. Advances in wall-conditioning techniques in the last two decades have greatly reduced the importance of oxygen as a low-Z impurity.

Magnetically confined plasmas have relatively low particle densities of 10^{18}-10^{21} m^{-3} and high electron temperatures ranging from a few tens of eV to 15 keV. The optical depth is low (i. e., the plasma is transparent to radiation) over most of the spectrum so the particles and radiation field and are not in thermodynamic equilibrium. Note, however, that the optical depth of Ly_α and Ly_β line emission from hydrogen and deuterium is significant in some divertor plasmas and it plays a role in the MARFE phenomenon, a localized thermal collapse at the edge of the main plasma[9-12]. Radiation transport of Ly_α will play an important role in the ITER divertor.

In the absence of significant particle flows, the steady state distribution of ion charge states in the plasma is determined by the balance between ionization and recombination processes. This approximation is known as coronal equilibrium. Because the electron and ion temperatures are of the same magnitude, ionization and recombination rates due to electron collisions are usually much larger than those due to ion collisions. The primary ionization process is electron impact, with multi-step ionization (excitation followed by ionization) being important in some cases. The dominant recombination processes are radiative recombination (electron capture followed by photon emission) and dielectronic recombination. Dielectronic recombination is a two-step process in which an electron is captured into an excited state of the ion with simultaneous excitation of a bound electron. The resulting system is energetically unstable; it then stabilizes by autoionization (no net recombination) or by emission of radiation, which leads to recombination. Three body recombination is typically negligible at the low densities of the core plasma, but it can be quite important in the divertor plasma (see Section V.E.2) or in the MARFE phenomenon[13]. Charge exchange recombination can play an important role in determining the ionization balance when large densities of neutral hydrogenic atoms are present, such as during high-power neutral beam injection for plasma heating or at the plasma edge where the density of thermal neutral atoms can be significant.

The electron impact ionization and recombination rates from ionization state z, I_z and R_z, are related to the cross sections for these processes by

$$I_z = n_z n_e \langle \sigma_I v \rangle = n_z n_e S_z \tag{1a}$$

and

$$R_z = n_z n_e \langle \sigma_R v \rangle = n_z n_e \alpha_z \tag{1b}$$

where n_z is the density of ions in the ground state of ionization state z, n_e is the electron density, σ_I and σ_R are the cross sections for ionization and recombination, v is the electron velocity and the angular brackets denote an average over an electron velocity distribution, usually taken to be Maxwellian. S_z and α_z are the ionization and recombination rate coefficients, which are the averages of the cross sections over the electron velocity distribution. The rate coefficients are calculated from atomic theory and are experimentally checked in some cases. Analytic expressions can be used when detailed calculations are not available. Large databases of atomic data for fusion plasma spectroscopy have been assembled; the ADAS[14] database is an example. (For a review of the status of atomic data for fusion plasma spectroscopy, see Summers *et al.*[15].) Because the ionization and recombination rates are proportional to n_e, the distribution of ions among the charge states in coronal equilibrium is given by ratios of the ionization and recombination rate coefficients:

$$\frac{n_{z-1}}{n_z} = \frac{\alpha_z}{S_{z-1}} \tag{2}$$

Calculations of the fractional abundances of the ionization states as a function of T_e for various elements are given in the literature. Carbon is fully ionized for T_e above a few hundred eV, while many kilovolt electron temperatures are required to fully ionize iron and to reach the higher ionization states of krypton.

The distribution of impurity ions from the relatively cold plasma edge to the hot core region can be described by a set of coupled impurity continuity equations:

$$\frac{\partial n_z}{\partial t} = -\nabla \bullet \Gamma_z + n_e\left[-n_{z-1}S_{z-1} - n_z S_z + n_{z+1}\alpha_{z+1} - n_z\alpha_z\right] \tag{3}$$

where Γ_z is the flux of particles in ionization state z. Particle sources and sinks are not explicitly shown but must be included in these equations when they are important, such as at the plasma edge. Note that with $\frac{\partial n_z}{\partial t} = 0$ and $\Gamma_z = 0$ for all z, these equations reduce to the coronal equilibrium conditions. Particle motion is very rapid along the field lines compared to motion perpendicular to the field lines. Thus, the ion spatial distribution in the plasma core can usually be treated as a one-dimensional problem, with the spatial coordinate being the direction perpendicular to the field lines. (In the edge region, local sources and sinks of ions can play a major role in determining the ion spatial distribution.) For example, the flux surface coordinate, ρ (equivalent to r/a for a circular cross-section tokamak), is often used as the spatial coordinate.

Because T_e usually peaks near the magnetic axis of the plasma, ionization states of a given element occur in a shell-like structure with higher ionization states in the core region and lower ionization states near the edge. In hot plasmas with T_e greater than ~1 keV, low-Z elements are fully ionized over most of the plasma volume, with the partially-ionized charge states concentrated at the plasma edge. Medium-Z elements exist primarily in the hydrogen- and helium like ionization states in the core, while high-Z ions retain significant numbers of electrons in the core region. This can be seen in Figs. 1-3, which show the steady state radial distributions of carbon, iron, and krypton ions versus normalized minor radius, r/a, in a JET tokamak plasma in coronal equilibrium with an electron temperature on axis, $T_e(0)$, of 10 keV[16]. The assumed T_e and n_e profiles are shown in Fig. 4. The calculation was done using the SANCO code[17], which solves Eqs. 3. Carbon is fully-ionized except for the region within a few cm of the edge. Iron is predominantly in the helium-like, hydrogen-like, and fully stripped ionization states in the core. Krypton is predominantly in the lithium-like, helium-like, and hydrogen-like ionization states in the core.

In general, radial motion of the ions cannot be neglected because it occurs on the same time scale as ionization and recombination in the core region. Thus, the coronal equilibrium assumption of $\Gamma_z=0$ is not valid and a model of the ion radial transport is required. It is common to write Γ_z as a sum of diffusive and convective terms:

$$\Gamma_z = -D_z(r)\nabla n_z(r) + v_z(r) n_z(r) \tag{4}$$

where $D_z(r)$ is a diffusion coefficient and $v_z(r)$ is a convective velocity. Neoclassical ion transport can be written in this form with $D_z(r)$ and $v_z(r)$ depending on the background plasma parameters. However, the observed transport in tokamaks and other magnetically-fusion plasmas is often much faster than predicted by neoclassical theory. Typical observed values of the transport parameters are D=0.1-1.0 m^2/s and v=0-10 m/s with the assumption that the transport does not depend on ion charge state. Experiments have shown that the diffusion coefficient is often hollow, not constant, as a function of radius with core values about an order of magntidue lower than in the outer half of the plasma.

Carbon, iron, and krypton radial distributions calculated assuming, for simplicity, $D_z=1.0$ m^2/s and v=0 are also shown in Figs. 1-3.[16] Comparison with the coronal equilibrium calculations shows that ion distributions are radially shifted by transport. In the core region, the density of a given ionization state occurs at a higher temperature with transport compared to coronal equilibrium. The ion shells are also broader, as expected when diffusion is important.

C. Line Radiation

The radiance or brightness, B_{jk} (photons/s-m^2-ster), of the line due to the transition from level j to level k of an atom or ion can be written

$$B_{jk} = \frac{1}{4\pi} \int n_z n_j A_{jk} ds \tag{5}$$

where n_j is the fraction of the total level population of the atom or ion in level j, A_{jk} is the radiative decay rate from level j to level k, and the integration path is the optical line of sight through the plasma. The total level population is normalized to unity:

$$\sum_j n_j = 1 \tag{6}$$

where the summation is over all levels j of the atom or ion.

In the core of low-density, hot plasmas, the dominant level population mechanisms are electron-impact excitation and de-excitation and radiative decay. As a result, the level populations are determined by the collisional-radiative equations:

$$\frac{dn_j}{dt} = n_e \sum_k n_k C_{kj} - n_e \sum_k n_j C_{jk} + \sum_{k>j} n_k A_{kj} - \sum_{k<j} n_j A_{jk} \tag{7}$$

where C_{kj} is the electron impact excitation or de-excitation rate coefficient for the transition from level k to level j. These rate coefficients are averages of the cross sections over a Maxwellian electron velocity distribution. Since the electron impact rate coefficients depend on T_e, n_j depends on T_e and n_e, and thus on the location of the ion in the plasma.

Although electron impact is usually the dominant excitation and de-excitation mechanism, other processes can be important in some situations and must therefore be included in Eqs. 7. Proton-impact excitation and de-excitation can be significant when the energy separation of the levels is small, as for transitions between the levels of a fine-structure multiplet. Population of levels resulting from charge exchange recombination is important when the spectrometer line of sight passes through a neutral beam; this is the basis of the active spectroscopic diagnostics discussed in the following article. Charge exchange due to thermal neutrals can be important for passive spectroscopy in some cases, such as for certain lines emitted near the plasma edge where the density of thermal neutrals can be large. Likewise, population of levels due to dielectronic recombination is important in the soft x-ray spectroscopy of highly-ionized medium-Z impurities. This is discussed in Section IV of this paper.

The level populations respond rapidly to changes in n_e and T_e, so a steady-state solution ($dn_j/dt=0$) to Eqs. 7 may be used in most situations. At the values of n_e found in magnetically-confined plasmas, most of the population is in the ground level or in metastable levels (levels that can not decay directly to the ground state by electric dipole radiation and thus have long lifetimes). For systems with no metastable levels, the populations of the upper levels of the intense resonance lines (lines with large values of A_{jk} and where the lower level is the ground level) often used for plasma diagnostics are determined by the balance between electron impact excitation from the ground level to and radiative decay to the ground level, i. e., these processes dominate in Eqs. 7. This is called the coronal approximation:

$$n_j = \frac{n_e n_g C_{gj}}{A_{jg}} \tag{8}$$

where g denotes the ground level. Using Eq. 5 and the approximation $n_z \approx n_g$, the line brightness is then

$$B_{jg} = \frac{1}{4\pi} \int n_e n_z C_{gj} ds\,. \tag{9}$$

Thus, n_z can be determined from the measured line brightness if the spatial profiles of n_e and T_e are known from other measurements. The total density of an impurity species can then be determined from n_z for one or more ionization states obtained from resonance line radiances and Eqs. 3. This provides a straightforward way of deducing the core impurity inventory of a magnetically-confined plasma from the measurement of the radiances of a few resonance lines of each ion. These lines occur in the VUV, EUV, and soft x-ray regions of the spectrum. The coronal approximation does not apply to transitions between excited levels or to magnetic dipole transitions between levels in the ground configuration of an ion. It is also not applicable when processes other than electron impact excitation and radiative decay are important; this is often the case in the edge region. In these cases, a full collisional-radiative model (Eqs. 7) must be used to calculate the line intensities. Finally, cascade effects are important for some lines excited primarily from the ground state and can included in a collisional-radiative model to obtain effective excitation rates to be used with Eqs. 8 and 9.

There are many examples in the literature of the measurement and modeling of the intensities and spatial profiles of spectral lines for the determination of impurity concentrations, radiative power losses, and impurity transport parameters. (Older papers are cited in the review papers mentioned earlier.) A good example of recent work that clearly discusses the method and atomic physics requirements is the study of high-ionized molybdenum radiation from Alcator C-Mod tokamak plasmas by Rice *et al.*[18].

In hot, low-density plasmas, spectral line shapes are almost always determined by Doppler broadening, which is large compared to the natural line width. (An exception can be lines from cold, high density regions such as the region in front of divertor target plates, for which Stark broadening can be significant.) The Doppler-broadened line shape is Gaussian:

$$\frac{I(\lambda-\lambda_0)}{I_0}=e^{-(2\sqrt{\ln 2}\frac{\lambda-\lambda_0}{\Delta\lambda_D})^2} \tag{10}$$

where I_0 and λ_0 are the peak line intensity and peak wavelength. $\Delta\lambda_D$ is the line Full Width Half Maximum (FWHM) given by

$$\frac{\Delta\lambda_D}{\lambda_0}=7.7\times10^{-5}\sqrt{T/A} \tag{11}$$

where T is the temperature (eV) and A is the atomic mass number of the emitting species. Thus, measurements of the Doppler width of spectral lines from ions provide a way of measuring the plasma ion temperature (T_i). Examples of this widely-used diagnostic technique are given below.

Wavelengths and corresponding atomic and ionic energy levels for spectral lines have been extensively tabulated. Two useful compilations for the spectroscopy of magnetically-confined plasmas are: Reader *et al.*[19] for neutral atoms and ions up to the fourth ionization stage and Kelly[20] for lines below 200 nm of all ionization stages of the elements from hydrogen through krypton. These data are available on-line. There are several other useful web-based line lists[21-24].

D. Continuum Radiation

The continuum radiation emitted by low-density, hot plasmas is the result of two types of inelastic electron-ion collisions: collisions that cause transitions between two continuum states of the electron (free-free transitions), emitting bremsstrahlung; and collisions that cause transitions between a continuum state of the electron and a bound state (free-bound transitions), emitting recombination radiation. The theory of bremmstrahlung and recombination radiation is treated in detail by Griem[1] and by Karzas and Latter.[25]

The bremmstrahlung power density per unit photon energy interval (W-m^{-3}-eV) can be written

$$\frac{dP_{ff}}{dE} = 1.54 \times 10^{-38} n_e Z^2 \bar{g}_{ff} \frac{e^{-E/T_e}}{\sqrt{T_e}} \tag{12}$$

where E is the photon energy, Z is the ion charge, and $\overline{g}_{ff} = \overline{g}_{ff}(E, T_e, Z)$ is the free-free transition Gaunt factor averaged over a Maxwellian electron velocity distribution. To obtain the total bremmstrahlung emission, this expression must be summed over all ions present in the plasma. If the nuclear charge is completely screened, the total bremmstrahlung power density per unit energy interval is

$$\frac{dP_{ff}^{Total}}{dE} = 1.54 \times 10^{-38} n_e^2 Z_{eff} \overline{g}_{ff} \frac{e^{-E/T_e}}{\sqrt{T_e}} \tag{13}$$

where the effective ion charge is defined as

$$Z_{eff} = \sum_Z \frac{n_Z Z^2}{n_e} \tag{14}$$

with the summation extending over all ionization states of all species. (This expression neglects the very weak dependence of $\overline{g}_{ff}$ on Z.) Z_{eff} is a measure of the impurity content of the plasma, with $Z_{eff}=1$ for a pure hydrogen plasma. Thus the factor Z_{eff} in Eq. 13 is the enhancement of the bremsstrahlung emission due to impurities over that from an hydrogen plasma. Z_{eff} is a useful quantity because it enters into the determination of the hydrogen isotope dilution caused by the presence of impurities and because it appears in the expression for the plasma resistivity. Values for $\overline{g}_{ff}$ are tabulated in reference 25. In the soft x-ray region (1-10 keV), $\overline{g}_{ff} \approx 1$ and in the visible region (E=1-2 eV), $\overline{g}_{ff} \approx 2\text{-}5$.

The expression for the power density per unit photon energy due to recombination radiation is more complex because summation over electron transitions from the continuum to all bound states of the ions is required. Using a hydrogenic approximation for the bound levels gives

$$\frac{dP_{fb}}{dE} = 1.54\times10^{-38} n_e Z^2 \overline{g}_{fb} \frac{e^{-E/T_e}}{\sqrt{T_e}} \beta(Z,T_e) \tag{15}$$

where $\overline{g}_{fb} = \overline{g}_{fb}(E,Z_i,T_e,n)$ is the Maxwellian-averaged free-bound Gaunt factor[25], and the factor $\beta(Z,T_e)$ is a complex expression incorporating the summation over possible transitions, assuming a hydrogenic approximation for the bound levels with principal quantum number n.[26] Note that Eq. 15 is similar to Eq. 12 with the additional factor of $\beta(Z_i,T_e)$ and the substitution of $\overline{g}_{fb}$ for $\overline{g}_{ff}$. This makes it possible to write the total continuum radiation, bremmstrahlung plus radiative recombination, in terms of the expression for bremmstrahlung:

$$\frac{dP_{total}}{dE} = \gamma(T_e,Z_i)\frac{dP_{ff}}{dE} \tag{16}$$

where $\gamma(T_e,Z_i)$ is an enhancement factor.[26] As a result of energy conservation, the radiative recombination spectrum has steps at the ionization energies of the various energy levels of the ion; i. e., recombination into the ground level produces only photons with energies greater than the ionization energy. Recombination radiation is therefore negligible in the visible region of the spectrum, so $\gamma(T_e,Z)$=1 and the continuum is pure bremmstrahlung as given by Eqs. 12 and 13. Thus, measurement of the visible continuum intensity can provide a useful measurement of Z_{eff}, as discussed below. In the soft x-ray region, recombination radiation dominates and $\gamma(T_e,Z_i)$>1 except for low-Z elements at high T_e, for which bremmstrahlung is the main source of continuum radiation.[26]

The relative contributions of line radiation, bremsstrahlung and recombination radiation to the iron spectrum in the soft x-ray region are shown in Fig. 5.[27] This calculation was done using the IONEQ code[28] assuming T_e=2 keV, $n_e=10^{20}$ m^{-3}, and an iron density of 10^{18} m^{-3}. It is clear that the lines are grouped into a few spectral regions and dominate the emission where they occur. (The line spectrum is not fully-resolved on the scale of this plot; the peaks actually consist of many closely-spaced lines.) Recombination radiation dominates the continuum except at very low energies, where bremmstrahlung is important. Also shown for comparison is the continuum emission from hydrogen; it is considerably weaker than the iron emission and bremmstrahlung dominates. This is because the total power emitted due to recombination radiation scales as Z^4 so even a small amount of a medium-Z element such as iron can dominate the total continuum emission. The strong T_e dependence of the continuum radiation in the soft x-ray region is evident in Fig. 5; thus, measurement of the slope of the continuum in the soft x-ray region can be used as a T_e diagnostic as discussed in Section III.B.

II. Core Impurity Measurements

A. UV, VUV, and EUV grating spectroscopy

1. Principles of UV, VUV, and EUV Grating Spectroscopy

Plasma spectroscopy in the UV, VUV, and EUV regions is most commonly performed using spectrometers based on diffraction gratings. These gratings consist of a plane, spherical-concave, or toroidal-concave substrate ruled with a large number of grooves, which may be either equally-spaced or variably-spaced to reduce abberations and to produce a flat focal surface. The groove structure results in diffraction of light into one or more spectral orders according to the grating equation[2]:

$$m\lambda = d(\sin\alpha + \sin\beta) \tag{17}$$

where λ is the wavelength of the light, d is the groove spacing, m is the spectral order number, and α and β are the angles of incidence and diffraction measured with respect to normal to the grating surface. The groove density of the grating, $1/d$, is usually given as the number of grooves per mm.

At wavelengths longer than approximately 200 nm (the UV and visible spectral regions), plasma spectroscopy is usually performed with spectrometers based on plane gratings and focusing mirrors or lenses[2]. A widely-used configuration is the Czerny-Turner spectrometer, in which a concave mirror collimates light from the entrance slit onto the grating and a second concave mirror focuses the diffracted light from the grating onto the image plane. Mirror and grating coatings with reflectivity values above 90% at near-normal-incidence are used to achieve high efficiency in these instruments. At wavelengths below 200 nm (the VUV and EUV spectral regions), the reflectivity of most coatings falls significantly below 90%, resulting in low efficiency for instruments requiring three reflections. Thus, spectroscopy below 200 nm is most often performed using spectrometers based on concave gratings because only a single reflection is required: the concave grating acts as both a diffracting and focusing element. In the VUV region (30-200 nm), concave grating spectrometers can operate at near-normal-incidence because coating reflectivities are typically greater than 50%. At wavelengths shorter than 30 nm, normal-incidence reflectivities are low and instruments designed to operate at grazing incidence are used. The transmission of air falls sharply below 200 nm, requiring a vacuum spectrometer. For some applications, the short-wavelength cutoff of normal-incidence spectrometers can be extended by purging with gaess such as nitrogen or helium. The short-wavelength cutoff of available window materials requires vacuum instruments below 105 nm.

The theory of traditional spherical-concave grating spectrometers is given by Samson[29] and Samson and Ederer[30]. The basic concept is that of the Rowland circle: if the center and tangent of a concave grating are placed tangent to a circle of diameter equal to the radius of curvature of the grating, light from a point source on the circle, such as the entrance slit, is focused onto the circle. The focusing properties of the grating are those of a spherical mirror that is illuminated off-axis. The focal surface is therefore curved. For grazing incidence illumination, there is significant astigmatism so a point on the entrance slit is imaged into a curved line in the direction perpendicular to the dispersion direction. Modern designs often use toroidal grating substrates to compensate the astigmatism and/or variable groove spacing to correct abberations and to produce a flat focal surface which matches planar electronic detectors[31-33].

It is desirable to record a portion of the spectrum with good time resolution during a single discharge. Thus, multi-element detectors such as photodiode arrays and charge coupled devices (CCDs) are widely used in present-day plasma spectroscopy. These detectors can be one- or two-dimensional. One-dimensional detectors typically have 512-2048 elements (pixels) oriented in the spectrometer dispersion direction and are capable of time resolution of 10 ms or less. An input window limits the usable sensitivity of standard photodiode arrays and CCDs to the region above 200 nm. At shorter wavelengths (VUV and EUV regions), an image intensifier consisting of a microchannel plate coupled to a phosphor screen is used to convert the input light to visible light, which is then coupled to the photodiode array or CCD. The input surface of the microchannel plate is usually coated with a photocathode for improved quantum efficiency. Phosphor screens can also be used to convert the short wavelength light to visible light. Where high time resolution of a single spectral line is required, single channel detectors such as photomultiplier tubes and photodiodes are used. Detailed discussion of detectors for the UV, VUV, and EUV regions is given in references 34 and 35.

2. Spherical and Toroidal Concave Grating Spectrometers

Concave grating spectrometers with multichannel detectors have been built for the VUV and EUV regions[31, 33, 36-48], and are now standard diagnostics on all nearly all MFE experiments. We discuss a few representative examples.

A widely used instrument is the SPRED spectrometer[31]. A toroidal grating images light from the entrance slit onto an array detector, as shown in the optical schematic of Fig. 6. An angle of incidence of 71° onto the grating provides good reflectivity for wavelengths down to 10 nm. The toroidal grating does not have the astigmatism of a concave grating used at grazing incidence, so the image height is well-matched to that of the detector pixels, resulting in high throughput compared to spherical-concave grating designs. The grating grooves are curved, producing a flat image plane that is well matched to an image intensifier. With a 450 g/mm grating, the spectrum in the 10-110 nm region is imaged onto a 25 mm photodiode array detector in the focal plane with 0.2 nm resolution. An example of a SPRED spectrum of this spectral region from the PDX tokamak is shown in Fig. 7.[31] The 10-110 nm spectral region is useful for identifying the impurity species present in the plasma because all elements have strong lines in this region. In a more recent application of the same principles, Biel *et al.*[33] have designed a group of four overview flat-field spectrometers covering the 2.5-160 nm region.

The SPRED spectrum of Fig. 7 shows a group of poorly resolved lines in the 10-30 nm region. These lines are due to $\Delta n=0$ transitions of transition metal (iron, chromium, nickel, and titanium) ions and $\Delta n>0$ transitions of carbon and oxygen ions. The prominent lines can be observed, but a more detailed study of the spectrum in this region requires higher resolution. To achieve this, the SPRED instrument can be operated with a 2100 g/mm grating, which covers the 10-32 nm region with 0.04 nm resolution[49]. Along similar lines, Kondo, *et al.* used a flat-field concave grating spectrometer covering the 10-40 nm region on Helitron-E[40]. High resolution can also be obtained by placing a multichannel detector on the Rowland circle of a spherical concave grating grazing incidence spectrometer. The detector is moved along the Rowland circle to allow observation of a 3-10 nm wide spectral region in a single discharge. High resolution spectra in the 1.5-36 nm region were obtained with two such instruments on the PLT tokamak[37, 38]. More recently, Beiersdorfer, *et al.*[39] have obtained high resolution spectra in the 1-6 nm region using a grazing-incidence, flat-field spectrometer on NSTX. Fig. 8 shows two spectra from this spectrometer. In Fig. 8a the K-shell lines of H- and He-like boron, carbon, and oxygen are well-resolved; Fig. 8b shows lines of H- and He-like nitrogen and $\Delta n>1$ transitions of highly-ionized iron.

For some applications, such as measurement of the ion temperature from Doppler broadening of lines or study of impurity spatial distributions, simultaneous spectral and one-dimensional spatial resolution is desirable. In the VUV region this can be achieved using the imaging properties of normal-incidence and near-grazing incidence spectrometers by limiting the entrance slit height and using a two-dimensional detector. The spatial profile of the emission is recorded in the direction perpendicular to the plane of dispersion. We mention two examples of instruments of this type. Yamaguchi, *et al.*[43] have obtained time- and spatially-resolved spectra in the 15-105 nm region from the GAMMA10 tandem mirror using an aberration-corrected grating at a 51° angle of incidence. Morita and Goto[48] have measured the spatial distributions of the H I Ly_{α} and C III 97.7 nm lines in the LHD stellarator using a spatially-resolving 3-m normal incidence spectrometer equipped with a two-dimensional CCD detector to observe the 30-310 nm region.

In the EUV region, it is possible to perform coarse one-dimensional spatial imaging using the large astigmatism of a spherical concave grating at grazing incidence[50, 51]; however, large-area detectors or multiple detectors are required. Spatial resolution can also be obtained by using a toroidal mirror at grazing incidence between the plasma and entrance slit of a conventional grazing incidence spectrometer to rapidly scan the plasma image across the entrance slit.[52] This technique has also been applied in the visible and VUV regions using a rotatable plane mirror in which sends light to Czerny-Turner and normal incidence spectrometers via focusing optics.[44]

3. Radiometric Calibration

A radiometric calibration is needed to obtain quantitative measurements of impurity densities from VUV and EUV spectra. This is complicated by the limitations of available absolute light sources for this spectral region. Two techniques commonly employed are: 1) branching ratios of spectral lines; and 2) synchrotron radiation emitted by electron storage rings.

The branching ratio technique relies on the fact that the ratio of the intensities of two spectral lines due to transitions from the same upper level of an atom or ion depends only on the probabilities of the transitions from that level, which are constant, and can be accurately calculated or measured in many cases.[53] This allows the radiometric calibration of a UV/visible spectrometer, which is straightforward to perform using calibrated lamps, to be transferred to a

VUV/EUV spectrometer. This technique has the advantage that it can be performed *in situ*, but it has the disadvantage that the number of useable lines pairs is limited by the available impurity elements, blending of lines with those emitted by other species, and the low intensity of the visible line in many cases.

The spectral distribution and absolute intensity of the synchrotron radiation emitted by relativistic electrons in a storage ring can accurately calculated[30]. There are a number of storage rings world-wide with beamlines set up for calibration work. This technique has the advantage that the emission is continuum, so a detailed calibration curve can be obtained. Also, with typical electron energies of several hundred MeV up to several GeV, strong signals can be obtained down to wavelengths of 1-5 nm. A complication can be the presence of more than one spectral order in the data, but this can be corrected for by the use of filters and by varying the spectral distribution of the emission by changing the electron energy.[54] Synchrotron radiation is highly polarized in the plane of the electron orbit. Since the grating transmission depends on the polarization of the incident light, the spectrometer must be calibrated with the grating grooves perpendicular and parallel to the electron orbit[55, 56]. The results are then averaged to obtain the calibration for the unpolarized light emitted by the plasma. The details of using synchrotron radiation to calibrate VUV and EUV spectrometers are given by a number of authors (see, e. g., references 36, 37, and 55-58).

A less-widely used technique for calibration of VUV and EUV spectrometers is the use of argon mini-arc[59] and high-current hollow cathode[60] secondary-standard radiometric sources. For example, Danzmann *et al.*[60] have described a high current hollow cathode lamp which can be used as a radiometric source for the 13-60 nm region.

4. Plane Grating and Transmission Grating VUV/EUV Spectrometers

The instrumentation described so far is based on a concave grating as the diffracting and imaging element. Instruments of this type are used as general-purpose spectrometers on all MFE devices. More recently, VUV and EUV grating spectrometers based on planar and transmission gratings have also been developed for specific applications. Two of these instruments are described in this section.

Soukhanovskii, *et al.*[61] have built a compact polychromator for measurements of VUV lines in tokamak divertor and scrapeoff regions. It utilizes a plane grating, input and output grid collimators, and a P45 phosphor screen to convert the emission to visible light, which is transmitted via an optical fiber to a remotely-located photomultiplier tube. The layout of the instrument is shown in Fig. 9. These instruments are constructed of high-vacuum materials and can be baked to 150° C. They are also sufficiently compact that groups of them could be deployed inside the vacuum vessel to provide spatially-resolved measurements of the divertor and scrapeoff regions, to which access is often difficult or impossible using conventional concave grating spectrometers viewing the plasma through ports on the vacuum vessel. A prototype was successfully used to measure the time evolution of the C IV 155.0 nm line on the CDX-U spherical torus.

Blagojevic, *et al.*[62] have developed an imaging transmission grating spectrometer for the 1-30 nm range, which has been tested on the CDX-U and NSTX spherical torus experiments. Light passes through an entrance slit, a perpendicular imaging slit, and then through the transmission grating, as shown in Fig. 10. The diffracted light is imaged onto a P45 phosphor screen deposited on a fiber optic faceplate, which serves as a vacuum interface. An image intensifier amplifies the visible light emitted by the phosphor, which is then imaged onto a 2-D

CCD array. The spatially-resolved spectrum in the 2-20 nm range measured with 0.6 nm resolution on CDX-U is shown in Fig. 11. This instrument provides good spatial resolution and adequate spectral resolution for the relatively simple spectrum of carbon and oxygen lines typically found in this region. A common feature of this instrument and the plane grating instrument described in the previous paragraph is that a phosphor screen is used to convert VUV or EUV emission into visible light, which allows the use of a variety of visible light detectors. This is discussed in detail by Soukhanovskii, *et al.*[63].

B. VUV and EUV Filtered Detector Spectral Line Measurements

An alternative to grating spectrometers is the use of filtered detectors to measure the time evolution of the intensities of individual spectral lines. The spectral resolution of this technique is poor compared to that possible with spectrometers, but it can be applied where the spectrum consists of a few well-separated, intense lines. Compared to a grazing incidence spectrometer with a multichannel detector, the filtered detector approach has the advantages of higher optical throughput and thus higher time resolution with good signal-to-noise ratio. It is also simpler to implement spatially-resolved measurements with filtered detectors than with grazing-incidence grating spectrometers. Here we discuss several examples of this technique.

In most MFE plasmas, the 1.8-4.1 nm spectral region contains only the relatively simple spectrum of the H- and He-like lines of boron, carbon, and oxygen, as seen in Fig. 8a. These lines are useful monitors of the low-Z impurity content of the plasma. Hokin, Fonck, and Martin[64] have measured the time evolutions of the intensities of the C^{4+} 4.03 nm, C^{5+} 3.37 nm, O^{6+} 2.17 nm, and O^{7+} 1.89 nm lines on the MST reversed field pinch using a Ross filter spectrometer. Four different filters composed of two thin foils of different materials are used.

Their transmission curves are shown in Fig. 12. (The composition of each filter is given in Table I of reference 64.) For each filter, the *K* absorption edge is at a slightly shorter wavelength than one of the lines of interest so that the transmission is several percent or greater at the wavelength of the line. The filters are coupled to four surface barrier diodes, all viewing the same plasma volume. The individual filters do not isolate a single spectral line, but the four signals can be used to form a system of four equations in four unknowns, which can be inverted to yield the individual line intensities assuming that the contribution to the signal of the high-energy continuum radiation transmitted by the filters is negligible. This is a valid assumption since the T_e of the MST plasmas was less than 500 eV. In hotter plasmas, a grazing incidence mirror could be used to eliminate the high energy continuum. Filtered detectors coupled to a grazing incidence mirror may be useful in the high neutron flux environment of a burning plasma since the detectors could be located remotely where they could be well-shielded and could be easily replaced what they fail due to neutron damage.

Arrays of filtered detectors can provide spatial resolution. For example, Stutman, *et al.*[65] built an array of filtered surface barrier diodes to observe the radial distributions of the C^{4+} 4.03 nm line, the C^{5+} 3.37 nm line, and O^{5+} lines in the 12.0-16.0 nm region in the CDX-U spherical torus. *M*-edge filters made of silver, palladium, and zirconium were used to isolate the lines. The spatial distributions and time evolutions of the line intensities were used to study fast MHD events.

Filtered detectors can also used in the VUV region by exploiting the *L* absorption edges of aluminum and silicon. Suzuki, Peterson, and Ida[66] have used such detectors to measure the spatial profile of oxygen emissions from plasmas produced by the Compact Helical System stellarator. Survey spectra showed that the 55.5-76.0 nm region is dominated by lines from O^{3+}

and O^{4+}. A thin aluminum foil was coupled to a 20-element absolute extreme ultraviolet (AXUV) photodiode array. These arrays do not have the dead layer that makes conventional silicon photodiodes insensitive to VUV radiation and therefore achieve high quantum efficiency in the VUV region[67]. A multilayer foil is used to eliminate higher energy soft x-ray photons. Soukhanovskii, *et al.*[68] have built a similar system, which was used to measure the radial profiles of C^{4+} 4.03 nm or O^{4+} 15.0 nm emission in order to study impurity transport on the CDX-U spherical torus. Gray, *et al.*[69] have also built a VUV filtered detector array based on AXUV photodiodes. It utilizes cultured quartz and magnesium fluoride filters to measure radiative power losses due to H Ly_α and C^{3+} radiation in the 120-155 nm region during disruptions in DIII-D.

C. Multilayer Mirror/Detector EUV Measurements

Spatially-resolved, high time resolution measurements of line intensities are often required for studies of MHD activity, incoherent fluctuations, and impurity transport. The brightest impurity lines available for these studies are found in the EUV region. However, while the grazing-incidence grating spectrometers generally used in this region have high spectral resolution, they have low optical throughput because the effective area of the grating at grazing incidence is small. This limits the time resolution possible with these instruments. In addition, it is difficult to build grazing incidence spectrometers with many spatial channels. Thus, other types of high throughput, spatially-resolving instruments are needed for these measurements in the EUV region. One approach is to use filtered detectors, as discussed in the previous section. Another approach is to use synthetic multilayer mirrors (MLMs), which are diffracting elements that can be used at near normal incidence in the EUV region.

A MLM is a periodic structure of alternating layers, each consisting of a high-Z reflecting layer and a low-Z spacer layer, deposited on a substrate. Plane substrates are most commonly used. The theory of MLMs is discussed by Underwood and Barbee[70]. A MLM diffracts incident radiation according to the Bragg relation:

$$m\lambda = 2d\sin\theta \tag{18}$$

where m is the order of refraction, d is the sum of the thicknesses of the two component layers, and θ is the Bragg angle measured from the surface. Thus, the MLM acts like the natural crystals used in soft x-ray spectroscopy. With a *2d* spacing of a few tenths of a nanometer, diffraction efficiencies of a few tens of percent can be obtained at normal incidence in the EUV region. The number of layers determines the achievable bandpass, which is typically 0.3-1.0 nm at wavelengths below 20 nm. As an example, the measured reflectivity and line shapes in the 9-18 nm region for a planar Mo/B_4C MLM with 75 layers and 2d=18.74 nm are shown in Fig. 13.[71] Peak reflectivities of 20-30% are obtained, with a bandpass of 0.7 nm.

Several MLM spectrometers have been built or designed for MFE experiments[72-75]. We discuss two recent examples that illustrate possible applications of MLM spectrometers. Stutman *et al.*[74] built a MLM spectrometer to perform impurity transport studies by measuring the emission from impurity pellets on the Large Helical Device. Fig. 14 is a schematic of the spectrometer. A series of grids collimates the incoming radiation onto a Ni/C MLM. The intense long-wavelength background light is blocked by a Ti/Parylene-*N* filter. The diffracted light is detected by a two-stage microchannel plate with a CsI photocathode. Fig. 15 shows the measured time evolution of the Mg H_α 4.55 nm line from an injected pellet containing magnesium. The high level of background light is attributed to the B^{4+} 4.86 nm line. Stutman, *et al.*[75] have also designed a telescope for very rapid imaging of C^{5+} at 3.37 nm (Ly_{α}) or 18.2 nm (H_{α}) for fluctuation studies. A MLM fabricated on a spherical concave mirror serves as both a focusing element and a diffracting element. Single mirror or Cassegrain (two-mirror) telescopes were designed. The detector could be either an intensified CCD camera or a two-dimensional array of photodiodes. This system is predicted to have sufficient optical throughput to allow imaging with good signal-to-noise ratio at several hundred kHz digitization rate, allowing it to be used for fluctuation studies.

D. Visible Bremsstrahlung Measurements

As discussed in the introduction, continuum radiation in the visible part of the spectrum is entirely due to bremsstrahlung in the hot core region of the plasma. The bremsstrahlung intensity is therefore related to the effective ion charge, Z_{eff}, n_e, and T_e, by Eq. 13. For visible radiation, T_e is much greater than the photon energy, so the exponential factor in this expression is unity. The remaining T_e dependences, $T_e^{-1/2}$ and the T_e dependence of the free-free Gaunt factor, are weak, so the visible bremsstrahlung intensity is primarily proportional to $Z_{eff}n_e^2$. Thus, Z_{eff} can be deduced from measurements of the visible bremsstrahlung emissivity when n_e and T_e are independently measured. A challenge is that the bremsstrahlung emission is weak compared to line and edge molecular band radiation in the visible, so care must be taken to choose a spectral region free of such radiation and to avoid contamination of the signal with visible light from other sources, such as reflections inside the vacuum vessel. An accurate radiometric calibration is required; this is done with standard calibrated light sources.

The first visible bremsstrahlung Z_{eff} measurement was performed on the JIPP T-II tokamak by Kadota, Otsuka, and Fujita[76]. They used an absolutely calibrated visible spectrometer to measure the bremsstrahlung radiance profile at 523.0 nm by scanning the spectrometer field of view on a shot to shot basis. This profile was Abel inverted to obtain the bremsstrahlung emissivity profile and the Z_{eff} profile was deduced from it using n_e and T_e measured by Thomson scattering. These measurements showed that Z_{eff} peaked on the plasma axis in high density plasmas. The spectrometer was scanned around 523.0 nm to verify that there were no lines within the spectrometer bandpass of 0.5 nm. This spectral region is commonly used for visible bremsstrahlung measurements.

This initial Z_{eff} measurement has all of the features of contemporary measurements, except that instead of a spectrometer, interference filters are usually used to isolate the bremsstrahlung emission. This allows higher optical throughput, resulting in a better signal to noise ratio, and makes it straightforward to build arrays of detectors or imaging systems to allow the spatial profile of the emission to be measured with good time resolution in a single discharge. An early example of the use and radiometric calibration of filter/detector arrays for spatially-resolved visible bremsstrahlung measurements is the system used on TFTR by Ramsey and Turner[77]. A more recent example of this approach is the system used on LHD by Nozato, *et al.*[78,79]. The diagnostic consists of 84 optical fibers with focusing lenses viewing the plasma horizontally at different elevations above and below the midplane, an interference filter with 5 nm bandpass centered at 521.5 nm, and a photomultiplier tube for each spatial channel. The system has been used to study impurity transport by observing the emission from injected impurity pellets.

An example of an imaging measurement of visible bremsstrahlung on the Alcator C-Mod tokamak is given by Marmar *et al.*[80] A plane mirror inside the vacuum vessel is used to provide a wide-angle, toroidal field-of-view in the plasma midplane. Relay lenses bring the image out to an interference filter, with 3 nm bandpass centered at 536 nm, and then to a 2048 pixel linear CCD. The detector is typically operated at a frame rate of 1 kHz to provide good time resolution. The measured spatial resolution is approximately 1 mm. The outer wall of the vacuum vessel is covered with black passivated stainless steel, which acts a viewing dump to minimize the contribution of reflected light to the signal. Fig. 16 shows the time evolutions of $T_e(0)$, $n_e(0)$, and $Z_{eff}(0)$ in deuterium and helium discharges. As expected for high density discharges, the Z_{eff} values are low (close to 1 and 2 for the deuterium and helium discharges, respectively). When Z_{eff} is low, the bremsstrahlung measurement provides a sensitive measurement of n_e due to the n_e^2 dependence of the emission. Because the diagnostic has excellent spatial resolution, this allows study of strong n_e gradients. An example is given in Fig. 17 which shows n_e profiles deduced from bremsstrahlung measurements at two times during an H-mode discharge. At the earlier time, the n_e profile is flat in the core region, with the sharp gradient at the edge characteristic of H-mode discharges. At the later time, the core density has peaked due to the development of an internal transport barrier. The values of n_e deduced from the bremsstrahlung measurements are in good agreement with the Thomson scattering measurements, as shown in Fig. 17.

Carolan *et al.*[81] have performed two-dimensional imaging of the visible bremsstrahlung emission from MAST plasmas using tangentially-viewing imaging optics, an interference filter, and a 1024 × 1024 pixel CCD camera. The image is binned into superpixels to yield a 128 × 128 pixel image at 128 Hz frame rate. Fig. 18 shows an example of an image of a MAST plasma in visible bremsstrahlung radiation. The figure also shows the Z_{eff} profile in the midplane obtained by Abel inversion of the midplane radiance profile and use of Thomson scattering measurements of T_e and n_e.

A recurring issue for filter-based visible bremsstrahlung measurements is the possible contamination of the signal by lines or molecular bands. When designing the visible bremsstrahlung diagnostic for a specific MFE experiment, the filter wavelength and bandpass are usually chosen using survey spectra to identify a clean spectral region. However, it is not always possible to routinely monitor the spectrum to check for unexpected lines or bands that occur only in certain operating regimes. Thus, spectroscopic measurements of visible bremsstrahlung emission have the advantage that interfering lines and molecular bands can be easily identified. It is straightforward to implement such measurements using modern high-throughput spectrometers and CCD detectors. An example is the system used by Meister, *et al.*[82] on the ASDEX Upgrade tokamak. Two arrays of tangentially-viewing sightlines viewing the core and edge regions of the plasma are fiber-optically coupled to spectrometers with CCD detectors. Both systems are radiometrically calibrated using a calibrated integrating sphere light source that is placed inside the vacuum vessel during shutdown periods, so that the data from both systems can be reliably combined to produce radial profiles of the emission. Fig. 19 shows a spectrum from the edge-viewing system. One strong line and several weak lines can be seen. However, the spectrum has several clean regions where the signal is only bremsstrahlung. The spectrum is fit to the expected λ^{-2} dependence of the bremsstrahlung emission to obtain the bremsstrahlung intensity, as shown in the figure.

Another approach to bremsstrahlung measurement is to use the optics and detectors of the Thomson scattering diagnostics available on most MFE experiments, as has been done by Röhr *et al.*[83] and Steuer *et al.*[84] on ASDEX and by Orsitto *et al.*[85] on the FTU tokamak. This approach is attractive because the equipment is already available and because the high-throughput optics and sensitive avalanche photodiode detectors of Thomson scattering diagnostics are well-suited to measurement of the weak bremsstrahlung emission. Many modern Thomson scattering diagnostics are based on Nd-YAG lasers which emit in the near-IR region at 106.4 nm with pulse lengths of ~10 ns and repetition rates of ~100 Hz. The time periods between laser pulses can be used for bremsstrahlung measurement by splitting the avalanche photodiode signal into a DC-coupled preamplifier in addition to the AC-coupled circuit used for the Thomson scattering measurement. Thomson scattering utilizes broadband interference filters to spectrally resolve the scattered laser light. Thus, spectral scans are needed to determine which Thomson scattering channels are free of line and molecular band radiation. A check can be made by comparing the Z_{eff} values obtained from different channels of the Thomson scattering diagnostic. This problem could be alleviated by implementing a dedicated narrowband filter for bremsstrahlung measurements, although this has not been done to our knowledge. It is also possible to correct for the contribution of the edge neutral emission by independently monitoring the D_α emission, as has been done on the MST reversed field pinch[86].

E. Issues for Core Spectroscopy of Burning Plasma Experiments

Implementation of core plasma spectroscopy diagnostics for a future burning plasma experiment (BPX) such as ITER faces a number of challenges. Many of these issues affect not only spectroscopy but other optical diagnostics as well. For example, windows and conventional solid-core optical fibers can not be used on or near the vacuum vessel because the high neutron and gamma radiation environment will cause a large loss of transmission due to darkening and it will lead to spurious signals caused by radiation-induced luminescence. Spectroscopic diagnostics must therefore view the plasma directly or reflecting optics located near the first wall must be used to collect light. Mirrors in close proximity to the plasma will experience erosion due to charge exchange neutral atoms escaping from the plasma. A potential solution to this problem is the use of monocrystalline metal mirrors or thin metallic film coatings on metallic substrates[87]. A more difficult problem is loss of reflectivity due to coating of mirror surfaces by impurity atoms (e. g., Be, C, and W) lost from the plasma. This appears to be unavoidable for mirrors near the first wall so *in situ* cleaning techniques must be developed[87]. A significant amount of work has been done on these problems. Because these issues are relevant to many diagnostics, they are covered in another article in this issue. However, there are some problems specific to the implementation of VUV, EUV, and soft x-ray spectroscopic diagnostics on a BPX. These problems and possible solutions are discussed in this section.

Design studies by Peacock, *et al.*[88] and Hawkes, *et al.*[89] point out the problems and some potential solutions for the implementation of VUV and EUV spectrometers viewing the main plasma on ITER. The microchannel plate image intensifiers, photodiode arrays, and CCD detectors used in VUV and EUV instruments are sensitive to neutron and gamma radiation and therefore must be well-shielded to avoid excessive noise in the BPX environment[90]. The neutron and gamma signals are seen as an increase in the overall background level of the data. This reduces the useful dynamic range of the signal and the shot noise associated with it degrades the quality of the spectrum. These effects are seen in present day experiments for high power Deutrium operation and were seen during D-T operation on TFTR and JET. For grazing incidence spectrometers, effective shielding is difficult due to streaming of neutrons and gammas down the beamline onto the detector, which is nearly in line with the entrance aperture.

Streaming can be reduced by the use of mirrors to deflect the input beam to the spectrometer. Barnsley, *et al.*[91] and Coffey, *et al.*[92] have prototyped this concept for the installation of a SPRED spectrometer on ITER by coupling the spectrometer on JET to the vacuum vessel via a long beamline with a gold-coated, spherical mirror used at a 15° angle of incidence. This allows the spectrometer to be located in a well-shielded bunker while reducing neutron and gamma streaming through the entrance aperture. The reflectance of gold at 15° is 40-60% above the short wavelength cutoff at 10 nm, so it is well matched to the 10-110 nm spectral region observed by the spectrometer. The mirror matches the divergence of the beamline to that of the spectrometer. The JET installation is shown in Fig. 20. Erosion and deposition should be negligible since the mirror is located far from the plasma. The mirror box also provides a direct view of the plasma for a soft x-ray spectrometer and a plane mirror provides a view for a fiber-optically coupled visible spectrometer. Fig. 21 shows spectra before and after the spectrometer was relocated from being close to the vacuum vessel with no shielding to the shielded bunker. The reduction in radiation-induced noise is at least an order of magnitude, even though the discharge for which the spectrometer was shielded had twice the neutron rate of the earlier one. In this installation, the beamline apertures were much larger than required to enclose the beam path. Optimized shielding would reduce the noise by an additional factor of 100, for overall noise reduction at the level required for ITER. Ebisawa, *et al.*[93] have shown how mirrors can be used to allow a VUV spectrometer to view the ITER divertor plasma.

An alternative to the use of mirrors is to deflect the input light to the spectrometer using hollow optical fibers in the EUV region. These fibers are inefficient, but the high intensity of EUV lines may make their use possible. An EUV spectrometer based on this principle was built and tested by Parsignault *et al.*[94]. The input fibers consist of seven holes in a high lead content glass rod. The spectrometer uses a toroidal mirror together with a plane grating to disperse the radiation and image it onto a CCD detector, providing spectral coverage of 5-20 nm in seven spatial channels.

Because VUV and EUV spectrometers are directly connected to the vacuum vessel, tritium retention in the spectrometer will be an issue for a BPX. The microchannel plate image intensifiers used in present day instruments have a large surface area and therefore retain significant quantities of tritium. The tritium beta decay can trigger electron avalanches in the microchannel plate, leading to spurious signals. This was observed in the JET experiments described above[92]. Thus it is desirable to find alternative means of converting VUV and EUV light to visible light for detection by photodiode arrays and CCD detectors. One possibility is the use of pixilated phosphor screens, as developed by Rodríguez-Barquero *et al.*[95]. The screen consists of a microcapillary array plate made of borosilicate glass with uniformly distributed 50 μm diameter holes. The holes are filled with grains of P45 phosphor powder, which has good quantum efficiency in the soft x-ray and EUV regions.

The use of a remotely-located beam diverting mirror and a shielded spectrometer is a good approach to implementing a non-imaging, spectrometer with a small acceptance cone on a BPX. However, when a wide field of view is required for imaging instruments, the first mirror must be located close to the first wall. To minimize the effects of erosion and coating, Stutman, *et al.*[96] have proposed the use of transmission diffracting optics, such as transmission gratings or Fresnel zone plates, to diffract a portion of the plasma light out of the plasma view to a shielded detector.

Because transmission gratings and zone plates for the VUV and EUV regions are freestanding structures made of refractory metals such as tungsten or tantalum, their optical properties should not be significantly affected by erosion and deposition if they are located behind a small aperture. Fig. 22 shows a conceptual layout of a transmission grating spectrometer viewing the ITER divertor[96]. The spectrometer is similar to that described earlier[62], and it provides simultaneous spectral and spatial resolution in the EUV region. Light from the divertor region is imaged onto the transmission grating by crossed narrow slits in a shield wall. The diffracted light is detected by a phosphor screen and the visible light emitted by the phosphor is transmitted by hollow optical fibers to a remotely-located, shielded detector. Hollow optical fibers that are not subject to radiation-induced transmission loss and luminescence have been recently developed and could be used for this purpose[97, 98]. The effects of erosion and deposition on the optical properties of a transmission grating viewing the ITER divertor in this configuration are predicted to be small[96]. In addition, because only a small portion of the grating is exposed to the particle flux from the plasma, it could be moved periodically to expose a fresh surface. Because they are used at normal incidence, transmission gratings are relatively insensitive to misalignment. Similar transmission grating spectrometers could be built for the VUV region[99, 100]. As an alternative to transmission gratings, Fresnel zone plates or micropatterned Fresnel mirrors could be used to disperse and deflect the light from the plasma[101, 102].

Multilayer mirror spectrometers such as those discussed earlier could also be used in a BPX. The mirror surface would have to be protected from erosion and deposition by a grid collimator and thin filter. Tests have shown that the peak reflectivity of multilayer mirrors is not strongly degraded by neutron exposure[103]. However, there is a small (1-2%) shift in the Bragg peak. The tests were conducted at high temperature so it is not clear if this shift is a neutron damage effect or a thermal effect. More work is needed to understand this.

III. Moderate and Low Resolution Soft X-ray Measurements

A. Introduction – Soft x-ray diagnostics

Soft x-ray (SXR) diagnostics diagnose the core of hot plasmas with electron temperatures above 1 keV[104-107]. Three basic types of SXR diagnostic have been developed. The pulse-height-analysis spectrometer (PHA)[26, 107] is a photon-counting detector which measures the overall SXR spectrum (typically 1-50 keV) with moderate energy resolution. It is used to determine T_e and impurity concentrations. The x-ray crystal spectrometer (XCS) measures K-shell spectra of impurity ions with high resolution. The spectra are used to determine T_i from Doppler broadening and the plasma rotation velocity from the Doppler shift, T_e from line ratios, and the impurity ionization balance from relative intensities of lines from various charge states[108]. X-ray imaging systems (XIS) [105, 109-111] or SXR arrays are one-dimensional cameras that measure the distribution of the SXR emission intensity across several chords of a poloidal cross section. The emissivity profiles are useful for MHD mode identification, fast measurement of electron temperature profiles, providing information on the safety-factor profile, measurement of electron heat thermal diffusivity, measurement of impurity concentrations and transport; and measurement of the toroidal rotation velocity. These cameras achieve crude energy resolution via absorber foils and the energy dependence of the detector quantum efficiency. The PHA and XIS diagnostics are described in this section and the high-resolution x-ray spectrometer is described in Section IV. Detailed discussion of tomography based on XIS data is given in another paper in this issue.

B. Pulse Height Analysis

1. The Soft X-ray spectrum

The PHA diagnostic uses one or more energy-resolving detectors to measure the spectrum of x-rays from a highly collimated (small cross-sectional area) beam emitted by the plasma, typically over the range of photon energies from 1 keV to 30-100 keV. In addition to measurement of T_e, the PHA diagnostic can be used to determine the presence of non-thermal electron distributions if they exist, identify medium-Z impurities from the energies of their lines, and to determine the concentration of low- and medium-Z impurities in the plasma. The PHA diagnostic has been employed on a number of magnetic fusion research devices[26, 107, 112-124].

Measurement of the parameters listed above can be understood from Fig. 5 and the x-ray spectrum measured by a PHA system viewing a horizontal central chord of the Tokamak Fusion Test Reactor (TFTR) shown in Fig. 23. The energy resolution of PHA detectors is typically 250 eV FWHM at 5.9 keV, so K_α lines of typical metallic impurities, such as Ti, Cr, Fe, and Ni, do not overlap. Since the energy calibration of PHA detectors is typically better than 50 eV, line energies can be determined precisely and the elements can be identified unambiguously. Concentrations of medium-Z impurities are inferred from the absolute line intensities by comparing the measured intensites with intensities calculated using Eqs. 5-7. The calculated intensities of a number of lines for each element are summed since the individual lines are not resolved. As shown from Eqs. 13 and 16, T_e is inferred from the slope of the continuum spectrum on a semilogarithmic plot. Note that the T_e measurement does not require measurement of the absolute intensity. Z_{eff} or concentrations of low-Z impurities, such as C and O, are inferred from the enhancement, γ (Eq. 16), of the absolute intensity of the continuum spectrum relative to that emitted by a pure hydrogenic plasma. Detailed explanations of these measurements are given in references 114 and 120.

Even though the spectrum in Fig. 23 is integrated along a central plasma chord, along which T_e is not uniform but varies significantly, the continuum spectrum is still approximately linear on a semi-logarithmic plot. This is because chord-integrated x-ray spectrum is strongly dominated by emission near the core due to the n_e^2 factor and the exponential factor in Eq. 13. The dashed curve in Fig. 23 represents a modeled bremsstrahlung spectrum assuming parabolic T_e and n_e profile shapes. The inferred central temperature, $T_e(0)$, is very insensitive to the assumed T_e and n_e profile shapes.

Determination of medium-Z impurity concentrations from the characteristic K_α peaks, such as those in Fig. 23, involves comparison of the measured absolute peak intensities with modeled intensities. Since each peak is a sum of intensities from several charge states integrated along a line of sight, the model must include the T_e–dependent charge balance calculations and the line-radiation intensity calculations discussed in Sections I.B and I.C. These modeling techniques are described in references 107, 114, and 120.

Once T_e is determined from the slope of the continuum and medium-Z impurity concentrations are determined from the characteristic K_α line intensities, the concentration of low-Z impurities, such as C and O, can be indirectly inferred from the enhancement, γ (Eq. 16), of the x-ray continuum above the emission from a pure hydrogenic plasma. The enhancement contribution due to medium-Z impurities is subtracted from the total enhancement and the remaining enhancement is assumed to be due to low-Z impurities. The concentrations of these elements can then be estimated with some knowledge of the primary low-Z impurity species and approximate ratios of their concentrations. This can be obtained from EUV and VUV spectroscopy. The total Z_{eff} is then calculated as the sum of the Z_{eff} contributions from all impurities.

2. PHA Instrumentation.

The PHA uses photon-counting x-ray detectors to intercept a highly-collimated beam of x-ray photons emitted from the plasma. Individual photons are absorbed by the semiconductor detector and create ion-electron pairs; the number of ion electron pairs is proportional to the energy of the photon. The electrons are rapidly swept out of the detector by an applied electric field. The charge is collected in a small integrating capacitor, generating a voltage which is proportional to the charge. The voltage is amplified by a preamplifier, resulting in a voltage pulse whose amplitude (pulse height) is proportional to the energy of the original x-ray photon. Typically the amplitudes of the pulses recorded within a given time interval are converted to a histogram of number of x-ray counts as a function of pulse height, or x-ray energy. Usually a number of such histograms, covering contiguous time intervals of duration 10 – 100 ms, are sequentially recorded during a discharge to provide a time history of the x-ray spectra during the discharge. The thermal continuum intensity decreases exponentially with x-ray energy, as illustrated in Fig. 23. Thus, typically three detectors, with foils having different low-energy cutoffs in the x-ray transmission, are employed to accurately measure three or four decades of the x-ray continuum intensity (as seen in Fig. 23) in order to infer T_e. The use of several detectors minimizes distortion of the continuum spectrum, particularly at high energy, because the x-ray flux to each one can be limited to minimize the effects of pulse pileup.

The PHA detectors are Si(Li) (Li-drifted Si) diodes for measurement of x-rays with energies up to about 30 keV. For higher energies, up to 100 keV or a few 100s of keV, high purity Ge detectors (HPGe) are used. The detectors are cooled by liquid nitrogen or by Peltier coolers to reduce the dark-current generated noise to acceptable levels. For higher energy x-rays, which might be produced in lower hybrid current drive or electron cyclotron current drive experiments, a Na(I) scintillator-photomultiplier detector is used.

Conventional PHA systems to date have used analog pulse processing of the detector pulses (amplification combined with shaping/filtering), followed by conversion of the amplitudes of the voltage pulses to a digital signal by a fast Amplitude-to-Digital Converter (ADC), and accumulation of the digital values in a histogramming memory. Two parallel amplifiers are typically used to enable sufficient energy resolution (~230 eV FWHM at 5.9 keV) to allow separation of close lying impurity K_α peaks, while at the same time allowing high count rates for good time resolution and minimizing distortion of the spectrum by pulse pileup[114]. Details of the implementation of conventional PHA systems and examples of measurements can be found in references 26, 107, and 112-124.

3. Recent advances

Several improvements in detector technology and electronic processing techniques in recent years have led to or could lead to significant improvements in PHA capability. Early Si(Li) or HPG detectors required bulky dewars for cooling to liquid-nitrogen temperatures in order to achieve sufficient energy resolution to separate the K_α lines of Ti, Cr, Fe, and Ni. Recently, the application of lower cost detectors capable of working at higher temperatures, such as Peltier-cooled Si-PIN diodes[125] or avalanche photodiodes[123] have significantly simplified the realization of PHA systems. These detectors and new detector designs, with significantly higher count-rate capability than the conventional Si(Li) and HPGe detectors, have enabled major improvements in time resolution capability for the PHA. Shi *et al.*[123] demonstrated on the HT-7 tokamak that an avalanche photodiode detector could be used to measure x-ray continuum spectra and T_e. However, the energy resolution of 0.96 keV FWHM at 5.9 keV was not sufficient to allow separation of metallic impurity K_α lines in order to determine impurity concentrations. Rossington, Walton, and Jakelvic[126] reported development of a large area Si(Li) detector with about one-sixth the capacitance of a typical planar detector of the same area. When used with a low capacitance FET preamplifier, this detector should be able to operate at a count rate 8-10 times higher than that of conventional detectors without sacrificing resolution. Lechner *et al.*[127] described another type of detector, the silicon drift detector (SDD), which can provide excellent energy resolution at counts rates up to several hundred kHz when cooled to -10° C. The SDD can even be operated at room temperature with reasonable energy resolution. The very low detector capacitance and incorporation of a JFET transistor directly on the detector chip contribute to reduced electronic noise and, thus improved energy resolution[128]. Shi *et al.*[129] and Chen *et al.*[130] describe 15-channel vertically viewing and six-channel horizontally viewing PHA systems on the HT-7 tokamak which use SDD detectors to measure T_e and metallic impurity concentrations. An interesting alternative to conventional PHA detectors is to use an x-ray sensitive CCD camera in pulse-couting mode. Such a diagnostic has been used by Liang *et al.* to measure time-integrated two-dimensional images of T_e in the CHS stellarator[131, 132].

Another advance is the application of digital signal processing (DSP) techniques to analyze PHA detector signals. In conventional analog processing PHA electronics, an amplifier with a filter circuit is employed to reduce the electronic noise contribution to the processed pulse in order to allow the pulse height to be precisely measured. A second, faster amplifier is typically employed to inspect for pulse pileup in the slower amplifier and allow inhibition of piled-up pulses. The "slow" amplifier significantly limits the count rate capability and, thus, the time resolution of the PHA measurements. Corrections for other defects in the pulse measurement process which add additional error to the measurement, such as charge trapping, the ballistic defect, and base-line restoration require the introduction of additional analog electronic circuits, which are additional sources of error[133]. These complications in the analog processing circuit can be avoided by digitizing the preamplifier signal and applying digital processing techniques to correct for the errors. Cardoso *et al.*[133] discuss these effects and describe a mixed analog-digital pulse spectrometer. The DSP portion of the spectrometer can make corrections for the measurement defects without requiring additional external analog circuitry. With fast digital processing, high throughput can be maintained.

C. Filter/SXR diode impurity and MHD mode measurements

1. Description of soft x-ray array diagnostic

A typical configuration of a SXR array is illustrated in Fig. 24, which shows two of the SXR arrays on NSTX[134]. Each SXR array consists of a pinhole or slot-hole camera measuring the SXR emission integrated along many chords through the plasma lying in a poloidal plane. In Fig. 24, many individual detectors view the plasma through a common slot aperture, but some implementations of this diagnostic use a single integrated detector array, such as a linear (1-D) photodiode array[135]. In the case of individual detectors, both Si surface-barrier diodes and PIN diodes have been used. For the conventional 1-D x-ray camera, the aperture, detector size, and distance between aperture and detector are chosen to provide a spatial resolution in the plasma of a few cm while maximizing signal. Typical x-ray fluxes onto each detector are 10^9 photons/s or more, allowing microsecond time resolution with good statistics. Although the measured emission profile is chord-integrated, this profile can be inverted to provide local x-ray emissivity as a function of minor radius. An example of signals from several detectors of a SXR array is shown in Fig. 25. Coherent oscillations due to a MHD mode are clearly seen.

More recent implementations of the SXR imaging concept have used 2-D detectors viewing the plasma toroidally through a circular pinhole to provide actual 2-D imaging of the plasma x-ray emission[111] in order to provide information on plasma instabilities and electron temperature, and to provide a constraint on plasma equilibrium calculations[136].

Absorber foils are usually inserted between the plasma and the detector, either to enhance response to particular impurity x-ray lines in the case of impurity diagnosis or to eliminate impurity lines to enhance the sensitivity of the instrument to plasma fluctuations by measurement of the core continuum emssion. The effect of the absorber foil on the x-ray spectrum is to either provide a sharp cutoff at the low energy end of the spectrum, or to emphasize the transmission in a narrow energy band by the use of K- or L-shell absorption edges. The x-ray transmission through a foil is given by

$$T = e^{-\mu(E)d} \tag{19}$$

where E is the x-ray energy, $\mu(E)$ is the energy-dependent absorption coefficient, and d is the foil thickness. Except near an absorption edge, μ can be approximated by $\mu \sim (E_c / E)^{-a}$, where $a \sim 3$. Thus, as the x-ray energy decreases below the “cutoff” energy E_c, given by $\mu\, E_c = 1$, the x-ray transmission decreases sharply, approximately as $exp(-1/E^3)$. The cutoff energy can be selected, e. g., to allow transmission of the higher energy L_α radiation from the H-like charge state, while reducing transmission of the lower energy L_α emission of the lower charge states. In contrast, the x-ray attenuation coefficient increases sharply as the x-ray energy increases across an absorption edge. Thus, filter materials can be selected with an absorption edge to allow transmission of lower energy lines just below the edge, such as those of the He-like and lower charge states, while sharply attenuating lines whose energies are just above the edge, such as those of the H-like ion. An example of the detector sensitivity for a SXR array filtered by two different foils is shown in Fig. 26. Each of these foil sets sharply attenuates x-rays with energies below about 2 keV, and the difference between the signals for two detectors, each using one of these foils, provides a pass band for impurity x-ray lines with energies in the range 4.5 – 5 keV.

The total power absorbed by a SXR detector is

$$I_{\det} = \int_0^{\infty} T_{foil} (P_{cont} + P_{lines}) Eff_{\det} \frac{A\Omega}{4\pi} dE \qquad (20)$$

where T_{foil} is the x-ray energy dependent transmission function of the foils, P_{cont} is the continuum power given by Eq. 16 and P_{lines} is given by Eq. 5, Eff_{det} is the x-ray absorption efficiency of the detector, A is the effective detector area, and Ω is the solid angle subtended by the detector.

2. Impurity measurements

Many researchers have used SXR arrays on MFE devices to measure impurity concentration profiles and to study impurity transport. Some examples are given in references 137-150 .

The technique for these measurements is to compare the measured broadband X-ray emission profile with theoretical simulations which use the measured T_e and n_e profiles to calculate the continuum radiation using Eq. 16 and the line radiation using Eq. 5 summed over all ions emitting line radiation within the range of sensitivity of the detector/foil combination. The impurity profile is inferred by adjusting the model impurity concentration profile so that the calculated emissivity profile matches the measured profile. A good discussion of this technique, as well as a description of the conventional SXR array employed on the TEXT tokamak is given by Wenzel and Petrasso[143]. An interesting recent application of this technique is presented by Shmaenok *et al.*[147] and De Bock *et al.*[148] They describe a spectrally resolving soft x-ray tomography diagnostic on TEXTOR, and tomographic reconstructions of profiles of Ne IX and Ne X. In this system, the x-ray beam from a pinhole camera is diffracted from a MLM (MultiLayer Mirror) and the diffracted light is detected by a 2-D detector.

3. Filter/soft x-ray diode Te measurements

Another application of SXR arrays is measurement of T_e profiles with good spatial and temporal resolution. The principal of the measurement is simple and can be understood by referring to Eqs. 13, 16, and 20[104, 151]. Two detectors filtered by different absorber foils view the same plasma region and measure the x-ray power transmitted through the foils. If the two foils are chosen to have different low energy cutoffs, and the x-ray spectra are primarily continua, with insignificant contributions to the x-ray emission by line radiation, then the ratio of intensities measured by the two different detectors is a well defined function of the electron temperature. By configuring these detector pairs in a fan-like array, as in the typical SXR array system, the T_e profile can be measured with good time resolution. For example, Kiraly *et al.*[152, 153] performed fast two-foil T_e profile measurements on TFTR using a SXR array. The principle of the diagnostic; the method of analysis, including corrections for impurity lines; T_e measurement results; and comparisons with other T_e measurements are described in detail[153]. If impurity lines contribute significantly to the x-ray spectrum, the contributions of these lines to the differently filtered detectors, relative to the contribution from the continuum, will likely be different. Thus, the modeling must include information about the impurity peak energies and intensities in order to infer T_e accurately. Other examples or discussions of the application of SXR arrays for T_e profile measurement are given in references 154-160.

4. MHD mode identification

The most common application of SXR arrays is the observation of MHD phenomena in plasmas and the identification of MHD mode toroidal (n) and poloidal (m) numbers, as shown in Fig. 25. An early application of this technique to MFE plasmas was the study by von Goeler *et al.*[105] of the sawtooth instability and associated $m = 1$ oscillations in the ST tokamak. Since then, SXR arrays diagnostics have been used on many MFE devices to study the effect of MHD modes on plasma gross stability, energy confinement time, and heat transport. There are many other examples in the literature; a few are given in references 81, 110, 134, and 137. A discussion of techniques for MHD mode identification with SX data is given by Kaita and Sesnic[163].

5. Recent advances

Some significant advances have been made in SXR array measurement technology. For example, tangentially viewing pinhole x-ray cameras with a single, fast two-dimensional detector have been used to provide a view of the poloidal cross-section of x-ray emissivity of NSTX. Images from this type of view can be simpler to interpret than that from one-dimensional, slot-hole detector arrays and therefore may lead improved understanding of fast fluctuation phenomena and thermal transport. Both fast CCD detectors[164] and fast gaseous electron multiplier (GEM) detectors with a two-dimensional anode array[165] have been used. Small, one-dimensional detector arrays on a single substrate have enabled construction of compact XIS arrays, allowing several cameras to be used at a single toroidal location for improved radial coverage.

An alternative to conventional soft X-ray diodes has been explored by Delgado-Aparicio *et al.*[166]. A columnar CsI(Tl) scintillator deposited on a fiber-optic faceplate is used to convert soft X-ray radiation to visible light, which is transmitted via optical fibers to remotely-located visible light detectors such as photomultiplier tubes or avalanche photodiodes. Although the quantum efficiency of this detection scheme is lower than for soft X-ray diodes, low-noise signals and high frequency time response (40 kHz) can be achieved through the use of large area detectors. A "three-color" optical array based on this approach has been implemented on NSTX. Three Be foils of different thicknesses filter the soft X-ray emission from each viewing chord to allow fast measurements of the space and time evolution of T_e. Fig. 27 shows the T_e time evolution in the plasma core measured by the optical soft X-ray array and by Thomson scattering[167]. The optical array measurement provides much higher time resolution than Thomson scattering. The optical array measurements are normalized to the Thomson scattering measurements at one time and agreement between the two measurements remains good at later times. This approach has the advantages of being less sensitive to neutron and gamma radiation than SXR diodes and may be easier to implement where space limitations require that the detectors be placed inside the vacuum vessel.

D. Challenges for Burning Plasmas

Application of x-ray PHA and SXR array diagnostics to burning plasmas will be problematic because of the intense DT neutron emission from the plasma. The detectors in these systems view the plasma directly, and thus receive both x-ray emission and the fusion neutron emission. The problems caused by neutrons are twofold: 1) both background noise in the x-ray detectors resulting from the fusion neutrons (and secondary gamma rays[90], and 2) damage to the detector material, reducing its usable lifetime.

At least four factors further compound the background noise problem due to the fusion neutrons. (1) The direct fusion neutrons down-scatter in energy and produce nuclear reactions in the shielding material surrounding the tokamak, effectively increasing the total neutron flux by a factor of approximately five. (2) A sea of background gamma rays results from these nuclear reactions, further increasing the detector background noise level, as well as damage. (3) It is impossible to collimate the fusion neutrons as tightly as the x-ray beams, because the mean free path of the neutrons in any collimation or shielding material is typically several centimeters; thus, the detector effectively accepts neutrons from a larger plasma volume than that of the measured x-ray emission. (4) The detectors for measurement of burning plasmas with T_e of 10 – 15 keV will need to be sensitive to higher energy x-rays. This requires that the detectors be thicker or made of higher-Z material than the present detectors (typically 3-mm thick Si for PHA and 0.3-mm thick Si for SXR arrays), which are optimized for lower energy x-rays emitted by plasmas with T_e of a few keV. Thus, the thicker or higher-Z detectors for burning plasmas would have a proportionally higher response to the neutrons and gamma rays.

Several techniques could allow PHA and SXR array systems to function on burning-plasma devices. These are (1) grazing-incidence x-ray mirrors or mosaic Bragg crystals to deflect the x-ray beam and remove the detector from the path of the streaming neutrons[168]; (2) bundles of glass capillaries[168-171] to increase the effective solid angle of the x-ray source, while partially shielding the nuclear radiation; (3) alternate detector materials or detector types with reduced response to neutrons and gamma rays and/or with higher radiation-damage thresholds[172];

(4) optimization of neutron/gamma-ray collimation and shielding of the detectors; and (5) active rejection or background subtraction of detector events resulting from impinging neutrons or gamma rays. Each of these techniques can reduce, but not eliminate, the background-noise and/or detector-damage problems.

Grazing-incidence x-ray mirrors can deflect the x-ray beam from the streaming nuclear-radiation beam and, thus, reduce the radiation induced noise and detector damage. Grazing-incidence mirrors have been extensively used in x-ray telescopes for imaging astrophysical x-ray sources[173- 176], and considerable development has been done, including measurement and calculation of reflection efficiency, and production of thin, self-supporting mirrors[177-179]. This technique has some limitations because of the small grazing-incidence angles required for efficient reflection of high energy x-ray beams[180]. For example, to diagnose plasmas with T_e of 10 keV, one needs to sample the x-ray spectrum at energies greater than 10 keV, preferably up to several times 10 keV. However, the efficiency for reflection of 10-keV x rays from glass or metallic reflectors is appreciable only at very small grazing angles, typically a few milliradians, and this angle becomes much smaller for higher x-ray energies[180]. Graded index multilayer “supermirrors” have been developed, which can extend the energy range for good reflectivity (20–40%) to values as high as 40 – 70 keV for incidence angles of order 5 mrad[177-179]. With such small deflection angles, the displacement of the x-ray beam is only a few cm for path lengths of several meters. Two or three reflections could enable larger deflections with reduced reflectivity[168]. Thus long, narrow radiation collimators would be required to minimize lateral spread of the radiation beam. Furthermore, the mirror reflectivity is strongly dependent on x-ray energy and deflection angle, so careful calibration of the efficiency of the optics as a function of x-ray energy would be required for reconstruction of the plasma x-ray spectrum in order to do quantitative measurements. For fluctuation measurements, however, only relative variations in x-ray intensity as a function of time need to be measued, so that calibration of the x-ray optics would not be required.

Arrays or bundles of glass capillaries imbedded in a neutron/gamma-ray shield have also been considered as a means of enabling direct x-ray measurements of burning plasmas[168, 169]. Calculations indicate that the SXR signal could be enhanced by about two orders of magnitude, relative to the neutron and gamma ray transmission. These glass capillaries rely on grazing-incidence reflection of the x-rays from the inner surface of the capillary tubes, so that efficient enhancement of x-ray throughput is limited to x-rays of energy up to a few keV.

An alternative technique to the PHA system for sampling the overall spectrum is the use of several relatively broadband crystal spectrometers, each tuned to measure different energy bands. Advantages of this technique are (1) that relatively large deflection angles can be achieved for the x-ray beam, so that the detector can be fully removed from the direct nuclear-radiation beam and (2) the throughput of the monochromators can be increased with x-ray energy to partially compensate for the exponential decrease of the continuum x-ray spectrum with energy. Disadvantages are that (1) x-ray measurement by Bragg diffraction has much lower efficiency than by direct detection by a PHA detector, so that larger diameter x-ray (and streaming neutron) beams must be utilized; (2) it is practical to sample only a few relatively narrow bands of the x-ray spectrum, rather than the full spectrum; and (3) each monochromator must be calibrated in order to provide a reasonable extrapolation to the overall x-ray spectrum. The energy-dispersive PHA detector measures the full, broadband spectrum, so that any impurities with peaks within the measured band can be detected. However a set of monochromators which measure small bands at different points of the spectrum could miss unexpected impurity peaks.

The silicon detectors used in the PHA and SXR arrays are sensitive to radiation noise and damage. The measured neutron fluences for significant degradation of performance are of the order of 10^{14} n/m^2 for Si(Li) detectors and 10^{17} n/m^2 for Si surface-barrier diodes. These radiation-damage thresholds of single crystal Si detectors are far too low for direct use as burning plasma diagnostics. Furthermore, (n,p) and (n,α) nuclear reactions in silicon, and Compton scattering of gamma rays can produce large pulses in SXR diodes, which can significantly degrade the capability to measure fast fluctuations. Thus, the use of alternate detectors has been considered.

Both gas filled proportional counters and scintillator-photomultiplier detectors have higher damage thresholds than do the Si(Li) and HpGe detectors used in conventional PHA systems. However the energy resolution of these detectors is not sufficient to allow separation of K_α lines of typical metallic impurities found in tokamak plasmas. However, well designed proportional counters or GEM (gaseous electron multiplier)[165] detectors might have sufficient energy resolution to measure the spectrum in the 10–100 keV range in order to determine T_e in plasmas with $T_e > 10$ keV.

Cryogenic x-ray detector arrays, such as the microcalorimeter[181-183], transition-edge-sensor (TES) microcalorimeter[184-186], and superconducting tunnel junction (STJ) detector[187], are other alternative x-ray detectors for PHA systems. Since the microcalorimeter detectors do not depend on the charge transport efficiency in a semiconductor, but rely on measuring the thermal rise in a small cryogenic absorber due to absorption of an x-ray, the radiation-damage threshold of these detectors may be considerably larger than that of Si or Ge semiconductor detectors. In the case of the microcalorimeter and TES sensor, the lifetime might actually be more limited by radiation damage of the thermistor which measures the temperature rise of the absorber material. These types of detectors are being developed mainly because of their broad bandwidth, very good energy resolution, of order 4-6 eV FWHM at 6 keV, and high efficiency for x-ray detection. While the maximum count rate of individual sensors is typically only of order hundreds to a few thousand counts per second for high resolution spectroscopy, the total effective count rate can be increased by using arrays of many detectors. A 3x3 STJ array has been operated at a total count rate of 10^5 s^{-1} with energy resolution of 40 eV at E = 277 eV[187]. Larger arrays[188-191] have been realized or are planned[192], and high-Z absorber materials, such as HgTe (ref. 182), Sn (ref. 193), and Bi (refs. 188 and 193) have been used to increase the efficiency of the detectors for high energy x-rays. A drawback of these cryogenic detectors is the need for a cryogenic refrigeration system.

One possible radiation-hard alternative to the Si surface-barrier and PIN diodes used in present SXR arrays, is the gridded ionization chamber (GIC). Such a detector was constructed and tested on the PDX tokamak with favorable results[172]. The grid is required to realize microsecond time resolution. It insures that the measured signal is due to collection of the (fast) ionization electrons only; in a standard ionization chamber, collection of the slower moving ion charge severely restricts the time resolution of the detector. While the GIC has fast time response, a disadvantage is the lower charge produced by x-rays in gaseous detectors (requiring about 30 eV of ionization energy per electron-ion pair) compared with silicon detectors (about 3.6 eV per electron-hole pair).

Reduction of radiation-induced background noise in photon counting x-ray detectors can be achieved by anticoincidence techniques or risetime discrimination[194]. In the anticoincidence scheme, a neutron/gamma-ray detector is placed behind the x-ray detector so that a gamma ray which Compton scatters or a neutron which undergoes small-angle scattering in the x-ray detector is then counted by the neutron/gamma-ray detector. An anticoincidence circuit is then used to inhibit acquisition of pulses in the x-ray detector (produced by the incident neutron or gamma ray) which are coincident with pulses in the n/gamma detector. If the incident nuclear-radiation flux is similar in magnitude to that of the x-ray flux, this type of circuit may introduce significant dead time. The x-ray detector typically has an efficiency of a few percent for detecting the nuclear radiation, while the anticoincidence detector has high efficiency, and will frequently inhibit the x-ray counting electronics.

Risetime discrimination in a proportional counter uses the fact that a soft x-ray produces a localized electron cloud in a proportional counter gas, so that the resulting anode pulse due to the following avalanche has a fast rise time[194]. A gamma ray, on the other hand, generally produces a high energy secondary electron through Compton scattering. This secondary electron produces ionization over a long range track in the gas. Thus the ensuing avalanche has components from different positions in the proportional counter, and the pulse generally has a slower rise time. Electronic circuitry can be used to sense the rise time and selectively reject events with slower risetimes.

A technique for reducing the effects of nuclear radiation noise in SXR diodes is to use a second detector near each diode which is blind to the x-rays, and to subtract the nuclear radiation signal from the x-ray plus nuclear radiation signal. This type of background subtraction can be done effectively for low and medium frequency fluctuations, but is less effective for high frequency fluctuations.

IV. Core High-Resolution X-Ray Crystal Spectroscopy

A. Introduction

The main application of x-ray crystal spectroscopy to diagnostics of MFE plasmas is measurement of the ion temperature and flow velocities in the core of the plasma. These measurements are performed by measuring the Doppler width and shift of x-ray lines emitted by highly-charged ions of medium-Z elements, such as argon, iron, and krypton. These elements may be present as indigenous impurities or are added in small amounts for diagnostic purposes. Of primary interest are the spectra of He-like ions, such as Ar^{16+}, Fe^{24+}, and Kr^{34+}, since the helium-like charge state, which corresponds to a closed-shell electron configuration, is relatively stable and exists for a wide range of electron temperatures. It is therefore possible to observe emission from He-like ions over a wide radial range of the electron temperature profile and to perform measurements of the ion temperature profile over a correspondingly large radial range, as shown in Figs. 2 and 3 for Fe^{24+} and Kr^{34+}. In addition, the electron temperature and ion-charge state distribution can be determined from intensity ratios of the He-like resonance line and the associated dielectronic and inner-shell excited satellite lines from Li-like ions. These measurements are useful to investigations of the ionization equilibrium and ion transport.

The choice of element for a particular experiment is largely determined by the central electron temperature. The elements from argon to nickel are in the He-like charge state for central electron temperatures in the range from 1 to 6 keV, which are typical for present-day tokamak and stellarator experiments. However, for future tokamaks, such as ITER, with anticipated central electron temperatures of 10 keV, krypton will be the best choice.

Measurements of the Doppler-width and Doppler-shift of x-ray lines from medium-Z ions require instruments with resolving power, $\lambda/\Delta\lambda$, of 5000–10000 in the wavelength range from 0.1 to 0.5 nm. Such resolving power has been obtained with curved crystal spectrometers. The limiting factor for the spectral resolution is usually the spatial resolution of the detector, which is about 0.3 mm for the widely used multi-wire proportional counters. This factor essentially determines the dimensions of the spectrometer required to achieve the desired spectral resolution. To a lesser extent, the spectral resolution of existing instruments is also determined by the rocking curve and the focusing errors of the curved crystals.

B. X-ray crystal spectroscopy instrumentation

The early development of x-ray crystal spectroscopy in tokamaks is described by von Goeler *et al.*[115, 195, 196] Very important for this development and the ensuing wide-spread use of crystal spectrometers were the early results from the ST tokamak, which showed that crystal spectrometers could be successfully used to resolve the x-ray line spectra from individual ion charge states. Comparison of the observed spectra with synthetic spectra constructed using theoretical atomic data[198] demonstrated that the radiation from dielectronic recombination was an important component of these ion spectra.

Fig. 28 shows a curved crystal spectrometer used on the PLT tokamak[199]. This spectrometer consisted of a cylindrically bent germanium (220) crystal with a radius of curvature of 2.42 m and a position-sensitive multi-wire proportional counter in the Johann configuration[200]. The angle of incidence of radiation onto the crystal and *2d* spacing of the crystal were chosen to satisfy the Bragg condition (Eq. 18) for wavelengths near 0.185 nm. The instrument had a spectral resolution of 4 eV at 6.4 keV, which was sufficient to resolve lines from different iron charge states, since the energy of the *1s-2p* transition increases by about 40 eV for each L-shell electron removed for charge states from Fe^{17+} to Fe^{24+}. The multi-wire proportional counter made it possible to obtain time-resolved spectra from a single tokamak discharge. From the analysis of the data, it was concluded that coronal equilibrium was satisfied in the central region of the plasma, within the factor of 2 uncertainty associated with the ionization cross sections used in the computations.

The *1s-2p* resonance line of helium-like iron (Fe^{24+}) at 0.185 nm was a prominent feature in the PLT spectra for central electron temperatures above 1.2 keV[199]. Since this line is isolated from other lines, it is well-suited to Doppler broadening measurements. An example of the measured and fitted spectra from a PLT discharge with neutral beam heating is shown in Fig. 29. These measurements were performed with a crystal spectrometer spectrometer having a high spectral resolution of $\lambda/\Delta\lambda = 100000$.[108]

At the time of these PLT experiments, detailed theoretical calculations for the spectra of helium-like ions became available. Several authors[201-203] provided data on the n=2 transitions for the main helium-like lines and the associated dielectronic and inner-shell excited satellites for the complete isoelectronic sequence. More involved calculations[203-206] were performed for the satellite spectra of helium-like iron (Fe^{24+}) for application to solar flare observations. These latter calculations provided theoretical data for the dielectronic satellite transitions $1s2pnl\text{-}1s^2nl$ with n=3–6 and which included, in addition to direct electron impact excitation from the ground state, the population of the n=2 state by electron cascades from higher-n levels, and excitation by inner-shell ionization. To experimentally verify these theoretical predictions, satellite spectra of the Fe^{24+} resonance line were recorded from a series of PLT discharges with different central electron temperatures. The spectra were in good agreement with the theoretical predictions and demonstrated that the line ratios of the dielectronic and inner-shell excited satellites with respect to the helium-like resonance line could be used for the diagnosis of the central electron temperature and measurements of the ionization equilibrium.[207] An example of the measured and calculated spectra is shown in fig. 30; the lines are labeled according to the widely-used nomenclature of Gabriel.[201] Line *w* is the $1s^2$-$1s2p$ resonance line commonly used for ion temperature and rotation velocity measurements.

Following the early work described above, x-ray crystal spectrometers became a standard diagnostic for the core of tokamak plasmas and were used on many experiments.[208-285] We review a few of the key developments.

The early work carried out on PLT and similar work on the TFR tokamak[208-211]demonstrated the importance of understanding the atomic physics of the x-ray spectrum for diagnostic applications. An extensive program to further understand the atomic physics of the x-ray spectrum is being conducted on the Tore Supra tokamak[212] using an upgraded Johann x-ray crystal spectrometer with eight cylindrically bent quartz crystals which can be remotely selected between shots.[213] This spectrometer can be set for observation of the He-like spectra of argon and the intrinsic metal impurities, titanium, vanadium, chromium, manganese, iron, nickel, and copper. The crystal cuts and radii of curvature of the cylindrically bent crystals were chosen so that the Bragg angle and crystal-detector distance remain approximately constant. The spectrometer is also routinely used for measurements of the ion and electron temperatures, and toroidal rotation of plasmas with LH and ICRF heating.[214, 215] An arrangement of x-ray absorbing metal strips in the focal plane facing the plasma makes it possible to distinguish the bremmstrahlung contribution from the background of hard X-ray and gamma radiation and to perform absolute measurements of the concentrations of metal impurities in Tore Supra[216].

On Alcator C-Mod, ion temperature and toroidal rotation velocity measurements are routinely performed by measuring the Doppler width and shift of the *1s-2p* resonance transitions in the He-like and H-like charge states of argon, which is added to each discharge in small amounts. The crystal spectrometers used on Alcator C-Mod are von Hamos type instruments[217]. These instruments are different from the Johann spectrometers used on other tokamaks because the spectral resolution and throughput are determined by an entrance slit with a typical width of 100 μm[218]. The throughput of a von Hamos spectrometer is also limited by the fact that each wavelength is reflected from a different position on the crystal. In contrast, the Johann spectrometer does not employ a slit and each wavelength is reflected from the entire crystal area. Johann spectrometers therefore have much higher throughput than von Hamos spectrometers. However, the x-ray emission on Alcator C-Mod is about 100 times higher than on other tokamaks due to the high electron density and the fact that the emission is proportional to the square of the electron density. Thus, the von Hamos spectrometers on Alcator C-Mod provide time resolved spectra with good statistics in spite of their relatively low throughput. Von Hamos type spectrometers are generally more compact than Johann spectrometers of comparable spectral resolution, so that it is easier to install several von Hamos spectrometers on a tokamak to obtain spatially-resolved measurements. An array of five von Hamos spectrometers with different sightlines is used on Alcator C-Mod for measurements of the profiles of the ion temperature and toroidal plasma rotation velocity[219]. The origin of plasma rotation in Alcator C-Mod plasmas, which arises without external momentum input, and which seems to play an important role for the formation of transport barriers and the transition to regimes of enhanced confinement, is presently a subject of intensive research[220- 224]. As an example, Fig. 31 shows the plasma stored energy, toroidal rotation velocity at four radii measured by x-ray crystal spectroscopy, and D_α emission in an Alcator C-Mod discharge[222]. The onset of toroidal rotation with no external momentum input following the transition into the EDA H-mode (indicated by the drop in the D_α emission) is clear.

New diagnostic applications and innovative instrumental designs were developed for lower-hybrid current drive experiments at the Frascati Tokamak (FT)[225]. Following a proposal by Gabriel and Phillips[226], the intensity ratios of the *1s*^{2}-*1s2p* resonance line and associated dielectronic *n=2* and *n=3* satellites of Fe^{24+} were used for the first time to measure the non-Maxwellian electron energy distributions produced in FT experiments[227]. A prototype of the first spatially-resolving Johann crystal spectrometer was built for FT by inserting a moveable horizontal slit between the crystal and a two-dimensional detector, so that a 2:1 image of the plasma was projected onto the detector[228]. A useful tutorial on x-ray spectroscopy and the experiments at FT is given by Bartiromo[229].

The Tokamak Fusion Test Reactor (TFTR) and Joint European Torus (JET) required diagnostics that could operate in the environment of intense neutron and gamma radiation resulting from D-T operation. The TFTR x-ray crystal spectrometer instrumentation consisted of a massively-shielded Johann configuration spectrometer in the TFTR Test Cell with a central line of sight in the horizontal mid-plane[230] and an array of up to five Johann x-ray crystal spectrometers with near-vertical sightlines for profile-measurements of the ion temperature.[231, 232] The latter instruments were located in the TFTR basement, where the background of neutron and gamma radiation in the basement was smaller by three orders of magnitude than in the TFTR Test Cell. Additional shielding was provided by lead and borated polyethylene shielding surrounding the detectors. The dimensions of these spectrometers were large as the radii of curvature of the cylindrically bent crystals varied between 10 and 12 m.

A Johann spectrometer of even larger dimensions, using a quartz crystal with a radius of curvature of 25 m and a Bragg angle of 50.75°, was built for JET[233]. The layout of this instrument allowed the crystal and detector to be positioned outside a 3 m thick concrete wall separating the torus hall from the diagnostic hall. The sightline of this spectrometer passed through the horizontal mid-plane of JET at an angle of 35° with a major radius of the torus at the magnetic axis, so that a large fraction (57%) of the central toroidal plasma rotation velocity could be observed as a Doppler shift. Because of its large dimensions, the dispersion and resolving power ($\lambda/\Delta\lambda = 20000$) of the instrument were very high, so that only a small spectral range, including the resonance line of helium-like nickel at 0.159 nm and nearby dielectronic satellites, could be observed.

Experience demonstrated that the JET spectrometer could indeed be used during D-T experiments while the shielding of the spectrometers on TFTR was only adequate for D-D operation. Nevertheless, x-ray spectroscopy on TFTR was very useful[234] because D-D experiments were the most common mode of operation on TFTR and each DT experiment was prepared by a series of DD experiments to optimize the experimental parameters.

The x-ray measurements of the ion temperature and toroidal plasma rotation velocity on JET and TFTR were based on Doppler measurements of the $1s^2 - 1s2p$ resonance line of the helium-like charge state of indigenous metal impurities, such as titanium, iron, and nickel. The spectrometer on JET recorded, almost exclusively, spectra of Ni^{26+} (refs. 236 and 237), whereas the spectrometers on TFTR recorded spectra of Ti^{20+} (ref. 238), Fe^{24+} (ref. 239), and Ni^{26+} (refs. 240-242).

For ion temperatures greater than 20 keV, measurement of the ion temperature on TFTR was complicated due to the fact that the spectral features were smeared out as a result of the large Doppler broadening. For instance, the satellite spectrum of the $1s^2 - 1s2p$ resonance line of Fe^{24+}, which showed 10 well resolved features during Ohmic heating, appeared to consist of only four wide overlapping features during the intense neutral beam heating phase[239]. This would appear to make an ion temperature measurement impossible. However, the ion temperature could be obtained from a least-squares fit comparison of the measured spectrum with a synthetic spectrum constructed from detailed theoretical predictions[203], treating the ion and electron temperatures, the position and intensity of the $1s^2$-$1s2p$ resonance line, and the relative abundance of the lithium-like and helium-like charge states, Fe^{23+} and Fe^{24+}, as variable parameters. The fact that the least squares fit value for T_e, obtained by comparing the predicted intensity ratios for the dielectronic satellites and the resonance line *w* with the experimental data, was in excellent agreement with the central T_e from Thomson scattering measurements provided convincing evidence that the synthetic spectrum included all the essential features[239]. It also indicated that the Fe^{24+} satellite spectra were predominantly emitted from the hot core of the plasma and that a least-squares fit value for the ion temperature represented the central ion temperature. Corroborating evidence for this conclusion was obtained from the observation that the ion-temperature value from the crystal spectrometer also agreed with central value of the ion temperature profile measured by charge exchange recombination spectroscopy[234].

In recent years, x-ray spectroscopy has been further developed on other MFE devices, such as LHD[244-247], TEXTOR[248-251], and NSTX[252-255]. The LHD spectrometer[244] employs a quadrangular crystal holder with four cylindrically bent quartz crystals, allowing the instrument to be tuned for the observation of the He-like ion spectra of argon, titanium, chromium, and iron. A diagram of the spectrometer is shown in Fig. 32. Instead of a multi-wire proportional counter, a CCD detector is used to achieve higher count rates and because it is relatively insensitive to magnetic fields. Because of the small pixel dimensions of typically 22.5 μm × 22.5 μm, the spatial resolution of a CCD detector is better by about an order of magnitude than that of a multi-wire proportional counter, so that a spectrometer with a CCD detector can be much more compact than one with a multiwire proportional counter and achieve comparable spectral resolution[260]. However, the dimensions of the spectrometer on LHD are large. Since the distance between the plasma and the diagnostic port is about 5 m, a large focal length corresponding to a radius of curvature of the crystals of about 3 m is required to reduce the field of view to an appropriate size. As a result of these constraints and the CCD size of 17.3 mm x 25.9 mm, only a small spectral range can be detected. The spectrometer has been successfully used for measurements of the central ion temperature and central plasma rotation in LHD experiments with electron-cyclotron, ion-cyclotron and neutral-beam heating[245-247].

The x-ray crystal spectrometers on TEXTOR and NSTX are high-resolution Johann spectrometers of similar design. They were designed for measurements of the dielectronic satellite spectra of Ar^{16+}. The crystals are cylindrically or spherically bent with a radius of curvature of 3.8 m. TEXTOR has two such instruments with dispersion planes parallel and perpendicular to the horizontal mid-plane of the tokamak, providing the capability for x-ray polarization measurements and the study of non-Maxwellian electron energy distributions.

The TEXTOR spectrometers have produced measurements of the time behavior of the ion and electron temperatures, toroidal plasma rotation, and ionization equilibrium during sawtooth oscillations by recording spectra with a time resolution of 1 ms, as shown in Fig. 33.[248] Accurate measurements of the argon ion charge state distribution as a function of density from TEXTOR discharges with and without neutral beam injection documented large deviations from coronal equilibrium due to charge exchange recombination during neutral-beam injection[249]. New experimental evidence was found for theoretically-predicted cascades between doubly excited levels, which mainly affect the intensity of inner-shell excited satellites for which the contributions from dielectronic recombination are weak.[250]

The spectrometer on NSTX was installed at the end of a long pump duct such that the dispersion plane coincides with the horizontal mid-plane of NSTX and the distance between the crystal and the plasma is 7.5 m. Since the spectrometer sightlines intersect the path of the neutral beam, it is also possible to study effects of the charge-exchange recombination of argon ions with energetic hydrogen atoms. The central electron temperatures of ohmic NSTX discharges are typically in the range 0.5-1.0 keV. The dielectronic satellites are therefore prominent features in the spectra, offering an opportunity to study these features under conditions where Doppler broadening is relatively small.

C. Atomic Physics Studies Using X-Ray Spectroscopy

Since tokamak discharges are well diagnosed and reproducible, they are also useful for experimental tests of atomic theory predictions and as bench-mark experiments for astrophysical observations. The extensive work done in this area is beyond the scope of this article; references 207, 210-212, 232, 235-240, 242, 248-250, and 254-281 cover various aspects of this work.

D. New instrumental developments

A new type of x-ray imaging crystal spectrometer which can provide spatially and temporarily resolved spectra of MFE plasmas is presently being developed.[282-285] The instrument consists of a spherically bent crystal and a two-dimensional detector, which are arranged in a Johann configuration. The imaging properties of this configuration have been discussed by Bitter *et al.*[252] and Bertschinger *et al.*[283].

Fig. 34 shows a spatially resolved spectrum of helium-like argon, Ar^{16+}, recorded with an x-ray imaging crystal spectrometer on NSTX.[252] The spectrometer employs a spherically bent quartz crystal with a radius of curvature of 3.888 m. The distances between crystal and detector and crystal and plasma are 3.14 m and 7.50 m, respectively, so that a demagnified image of a large plasma cross-section that extends from -0.40 m below to +0.40 m above the horizontal mid-plane of NSTX was projected onto a 0.10 m (wide) x 0.30 m (high) multi-wire proportional counter. The spatial resolution in the plasma was about 0.015 m. The lines are elliptically curved since the Bragg reflected x-rays lie on a cone which intersects the detector plane. The single-photon count rate count rate upper limit of 400 kHz of the two-dimensional multi-wire proportional counters used limited the time resolution to 100 ms or longer. The data shown in Fig. 34 were therefore recorded from several NSTX discharges to improve the statistics. So far, the best spatially resolved spectra of Ar^{16+} have been obtained with an x-ray imaging spectrometer of similar dimensions on TEXTOR, where it is possible to record spectra with good statistics during the 4 s flattop period of a single discharge.[284] The spatially resolved argon spectra obtained from TEXTOR have been used to derive radial profiles of the electron temperature and ion charge state distribution.

Efforts are now underway to equip these imaging spectrometers with high count rate detectors. A compact imaging x-ray crystal spectrometer which employs CCD detectors and a set of several spherically bent crystals will be installed on TEXTOR to record time-resolved radial profiles of the ion charge-state distribution for transport studies.[283] New two-dimensional segmented multi-wire proportional counters with up to eight segments and count rates of 400 kHz per segment together with fast readout electronics are presently being developed for use on NSTX and KSTAR.[285] A promising new high count rate detector for this application is the semiconductor pixel array (PILATUS II detector). [286] The size of a PILATUS II detector module is 80 mm x 34 mm and the size of a pixel is 0.172 mm x 0.172 mm. Each pixel has its own readout electronics, so that single photon counting at a rate of 1 Mhz per pixel is possible. A recent test of a PILATUS II detector module on one of the X-ray crystal spectrometers on Alcator C-Mod successfully recorded spectra of Ar^{16+} at 3.1 keV. It is planned to equip a new X-ray imaging crystal spectrometer on Alcator C-Mod with several PILATUS II detector modules. Due to the high radiation intensity on Alcator C-Mod, it should be possible to obtain spatially resolved Ar^{16+} spectra with good statistics and 10 ms time resolution. These data will provide measurements of the ion-temperature and toroidal plasma rotation velocity profiles.

F. Issues for Burning Plasmas

The imaging x-ray crystal spectrometer may be useful for ion-temperature measurements on ITER. This instrumental concept has been adopted for a design of the ITER X-ray crystal spectrometers.[288] ITER diagnostics must operate in an environment of intense neutron and gamma radiation. A crystal spectrometer has the attractive feature that the radiation is reflected by the crystal onto the detector at the Bragg angle, so that the detector is not in line with radiation streaming through the aperture in the first wall. It is not yet clear whether solid-state detectors can be used in the ITER environment. A viable alternative may be gas filled multi-wire proportional counters and/or GEM detectors[165], which are not damaged by neutrons. It is also not yet clear whether crystals can withstand the high neutron fluxes without damage. Experiments are now underway to measure the impact of high neutron fluxes on the rocking curve of spherically bent crystals. In preparation for ITER, it will be necessary to continue the early experiments with krypton on TFTR[243] on present-day tokamaks to understand the X-ray line radiation of krypton and the impact of krypton on the plasma performance under various experimental conditions. The TFTR experiments[243] showed that the ion charge-state distribution of krypton and, in particular, the concentration of helium-like Kr^{34+}, depend strongly on the profiles of the electron temperature and electron density.

V. Edge and Divertor Visible Spectroscopy Measurements

A. Overview

Spectroscopic observations of impurities in the edge and divertor regions of the plasma typically focus on understanding processes which can limit the performance of existing experiments and may limit the performance of future tokamaks, such as ITER, and other MFE experiments. This section describes diagnostics which measure and characterize 1) intrinsic impurities produced by erosion of plasma-facing components; 2) extrinsic (injected) impurities used to simulate helium ash or to reduce heat fluxes; and 3) utility impurities, which are introduced to provide optimum pre-conditioning of plasma-facing surfaces. A number of visible and UV spectroscopic diagnostic systems are typically used to identify and quantify impurity emissions in the wavelength region between 200 nm–1000, and filtered camera systems are used to measure one- and two-dimensional distributions of the particle influxes in the divertor and edge plasma regions. Commonly observed impurities are lithium, beryllium, boron, carbon, oxygen, copper, molybdenum, and tungsten which originate from the divertor target plates and from the first wall surfaces in the main chamber. Neon and other impurity gases injected into the plasma for radiation cooling in the divertor are also studied.

The choice of optimum plasma-facing materials will be especially important in the near future, as decisions must be made soon for the early operation of ITER. Many experiments have been carried out on this topic, and much interpretative modeling has been devoted to the understanding of the properties of carbon components and to the optimization of the plasma-facing surfaces. Interpretation is needed to infer erosion rates and the efficiency of core plasma contamination by intrinsic impurities. Additional concerns are the rate at which co-deposited intrinsic impurities contribute to deuterium retention (and possible T retention in D-T operation) and the effects of ELMs and localized hot spots on wall and limiter surfaces. An important element of this work is the resolution of global impurity production into its component processes, such as direct particle-induced physical sputtering (both by plasma and by impurity ions), chemical erosion processes producing molecular hydrocarbon products, and radiation-enhanced sublimation (RES), in which the sublimation rate is increased by neutral atom fluxes.

Experiments with the extrinsic impurity He are performed to simulate the recycling properties of helium ash. Experiments with higher-Z noble gases are conducted to enhance core and divertor radiation as a means of reducing the heat flux onto limiter and wall surfaces. Some concerns are similar to those mentioned above, namely the efficiency with which externally injected impurities penetrate the scrape-off layer (SOL) to contaminate the core plasma, and the dynamics of transport in the SOL and divertor plasma. There is also an important need to establish the localization (compression) of impurities near the divertor and their relative enrichment compared with bulk ion concentrations.

Finally, one of the striking aspects of tokamak confinement physics is the degree to which changes in surface conditioning directly improve energy confinement. A few examples are: carbonization leading to H-mode confinement, boronization leading to the VH-mode in DIII-D, boronization of the molybdenum first wall in C-Mod leading to decreased radiation losses and improved confinement, and the application of lithium wall coatings to produce the Enhanced Reverse Shear regime in TFTR. Thus, spectroscopy of utility gases that are introduced to study wall conditioning is an important topic in preparation for ITER operation.

The subject of modeling and interpretation of visible and UV emission from the edge and divertor regions of MFE plasmas is an extensive one that can not be covered in this paper. A good introduction to current work in this area is given in references 289-294.

B. Visible, UV, and near-IR grating spectroscopy

Due to the harsh environment (x-rays, neutrons, γ-rays, and high magnetic field) in the vicinity of an MFE experiment, many visible diagnostics use optical fibers to bring the light from light collecting optics located near the vacuum vessel to remotely-located spectrometers and filtered detectors. High-purity fused silica optical fibers up to 1.0 mm in diameter are typically used. These can be several meters to ~100 meters in length. The region of the spectrum that can be observed is determined by the transmission properties of the fiber. Fig. 35 shows a transmission curve for a silica-clad silica fiber. The useful spectral transmission range for plasma diagnostics is approximately 220 nm to 2000 nm; over most of this range, the fiber has a low attenuation of < 30 dB/km. The numerical aperture, NA, of a typical 1 mm diameter silica-clad silica fiber is ≈ 0.23, which corresponds to an f-number of *f*/2.2. Plastic-clad silica fibers are also widely used and can have a larger NA.

A fused silica window typically serves as the vacuum interface for visble and UV diagnostics mounted outside the vacuum vessel. Telescopes focus the light onto the ends of optical fibers which transport the plasma light to the spectromter or filter detector. The Czerny-Turner spectrometer configuration[295] is widely used for these measurements because it is able to scan over a wide spectral range with low or high dispersion, as needed for a particular experiment. A plane grating, located between collimating and focusing mirrors, is rotated to vary the observed wavelength region. Most commercial Czerny–Turner spectrometers achieve f-numbers in the range $f/4$-$f/11$. An example of an early use of fiber optics coupled to a 1.0 meter grating Czerny-Turner spectrometer is the system used for impurity studies on JET.[296] Detection of the plasma light at the exit aperture of the spectrometer was accomplished by an optical multichannel analyzer (OMA). Seraydarian *et al.*[297, 298] also used a Czerny-Turner spectrometer with intensified linear photodiode array detectors, as shown in Fig. 36, to obtain high resolution spectra on DIII-D. Burrell *et al.*[299] have recently equipped faster (*f*/4.7) spectrometers on DIII-D with charge-coupled device (CCD) cameras to increase the photon detection efficiency, and thus improve the time resolution of the system. Fig. 37 shows a spectrum obtained from a JET helium discharge collected with a Czerny-Turner spectrometer equipped with a CCD camera detector.[300] It contains many low ionization-state lines of the wall materials carbon and beryllium. Prominent lines in the spectrum are D_β, and lines emitted by He, He^+, Be, Be^+, C^+, C^{2+}, C^{4+}, and C^{5+}. Visible bremsstrahlung is also present.

Recent advances in commercialization of volume phase holographic (VPH) gratings have enabled new compact visible spectrometers that offer several advantages over the Czerny–Turner configuration, including high throughput (*f*/1.8), stigmatic imaging and high grating efficiency.[300,301] Transmission grating spectrometers using the VPH technology are commercially available.[302, 303] In these spectrometers, a transmission grating is located at the intersection of the optical axes of two commercial camera lenses oriented perpendicular to each other. The use of commercial camera lenses ensures high resolution, flat field imaging. A CCD detector is placed in the image plane of the spectrometer. Each grating is designed to cover a specific wavelength range. Optical fibers may be placed in the image plane of the input collimating lens since the f-number of the fiber closely matches that of the spectrometer. This eliminates the need for inefficient étendue-matching optics. Thus, the fibers can be mounted directly to the entrance slit of the spectrometer. In a typical Czerny–Turner configuration, the image of a $f/2$ fiber would need to be magnified 2–5 times to match the $f/4$ - $f/9$ spectrometer, resulting in light loss. With stigmatic near-axis imaging, fibers can be closely stacked along the length of the entrance slit without causing cross talk in the detector plane. This allows spectra from many spatial locations to be observed on a single 2-dimensional detector. The typical grating efficiency for VPH gratings is 80% for unpolarized light.[304] As a result of the Bragg condition for the gratings typically used, only first order light is diffracted. The transmission grating spectrometer has the advantages over the Czerny–Turner spectrometer of higher throughput and good imaging properties, but it has the disadvantage that a given grating covers only a fixed wavelength range. However, this is not a problem for many plasma diagnostic applications, which require routine measurement of a few specific lines. The short focal length of the camera lenses (50–85 mm) produces strong spectral line curvature in the detector plane. The spectral line curvature can easily be overcome with curved slits.[301, 304] The details of the grating equations and slit curvature of this spectrometer can be found in Bell *et al.*[301]. The arrangement of a VPH grating spectrometer with a CCD detector used on JET is shown in Fig. 38.[305]

A diagnostic based on a VPH grating spectrometer has been used to measure the poloidal and toroidal flow velocities as well as temperatures in the edge of NSTX discharges[306]. Plasma rotation is both theoretically and experimentally linked to improved stability and confinement. Measurement of flow velocities is therefore important for understanding tokamak confinement and transport.[307-309] Since graphite tiles are used in high heat flux areas of most present-day tokamaks, line emission from edge carbon ions can be extremely bright, and is therefore well-suited to diagnostic measurements. In the plasma edge, low charge-state ions are formed by successive electron impact ionizations of inflowing neutral impurity atoms. Electron impact ionization is therefore the primary excitation mechanism for these ions. As a consequence of the steep electron temperature gradient at the plasma edge, narrow shells of C^{2+} emission are formed in this region. The intersection of a diagnostic sightline with the edge C^{2+} emission shell provides spatial localization of the measurement.

For the NSTX edge rotation diagnostic, light is collected from six sightlines, as shown in Fig. 39. The plasma is focused onto optical fibers by a telescope viewing through a fused silica vacuum window mounted on the top of the machine. The details of the optical head and the geometry of the sightlines are given by Biewer, *et al.*[306] and Bell *et al.*[304] The lens assembly in the optical head images the carbon emission onto the six fibers which transmit the plasma light from the tokamak to the remotely-located spectrometers. All of the lens elements are fused silica to avoid loss of transmission due to neutron exposure. Shutters are mounted on the vacuum side of the vacuum window to protect against contamination during vacuum vessel bakeout and He glow-discharge cleaning. Fig. 40 is a sample spectrum from the NSTX edge rotation diagnostic showing the C^{2+}, C^{3+}, and He^{+} lines. The spectrum from each sightline is a line-averaged measure of the intrinsic emission of a given species in the edge of the plasma. Local measurements of the ion spectral line emissivity, velocity, and temperature are obtained by inverting the data.[310, 311] Similar measurements of plasma rotation in the edge have also been performed on the COMPASS-C tokamak by Bamford *et al.*[312]

Absolute calibration of visible spectrometer systems is typically performed before and just after each plasma campaign using an absolutely-calibrated integrating sphere light source. During vacuum openings, the integrating sphere is placed inside the tokamak vacuum vessel and the response of each channel is recorded to provide an absolute calibration which incorporates all geometric factors.

On the Alcator C-Mod tokamak, poloidal and toroidal rotation measurements have been obtained using a high throughput (*f*/3.0) visible (350 –700 nm) spectrometer similar to the VPH transmission grating spectrometer.[313] The spectrometer has a temporal response of 1 ms and a rotation velocity sensitivity of $\sim 10^3$ m/s. The fast time resolution and high spectral resolution are possible due to a 0.15 m diameter transmission grating that provides a resolving power of $\lambda/\Delta\lambda \sim$ 15,500 at 576.9 nm. The detector is a 1-dimensional linear NMOS photodiode array with 512 pixels that are 50 μm x 2.5mm. The wavelength coverage is ~15.0 nm.

On LHD, Yoshinuma *et al.*[314] have built a compact, high-throughput spectrometer which has a scanable grating. The spectrometer consists of *f*/2.8 camera lenses with 400 mm focal length and a 2160 g/mm grating. The dispersion of the spectrometer is 0.73 nm/mm at 524.9 nm, which yields an instrumental line width of 0.08 nm for a slit width of 100 μm. The 652 x 496 pixel CCD detector has a pixel size of 12 μm, which yields a wavelength range of 5.7 nm. This spectrometer has been used for measurements of the ion temperature, toroidal rotation, and radial electric field on LHD during Ne gas puffing experiments.

A great deal of research has been carried out using visble spectroscopy to characterize the behavior of potential ITER first wall materials, such as carbon and tungsten. References 315-320 describe some of this work.

C. MOSS spectroscopy

An interesting alternative to conventional grating spectrometers has been developed on the H-1 heliac by Howard *et al.*[321, 322] The electro-optically modulated solid-state (MOSS) spectrometer is a Fourier transform interferometer modulated around a fixed delay. Because there is no entrance slit, the entrance aperature can be large, resulting in high throughput and good time resolution. Such an instrument equipped with a CCD detector has been used to make fast 2-D measurements of the Doppler broadening and shift of impurity lines on H-1, from which tomographic reconstructions of T_i and plasma flow velocities were made.

D. Impurity line measurements via discrete filtered detectors and filtered cameras

1. Discrete filtered detectors

Absolutely-calibrated measurements of the D_α line intensity are widely used on MFE experiments both as a monitor of fuel particle confinement and as a diagnostic of MHD instabilities. D_α light is emitted primarily from the plasma edge and divertor regions, and observations at multiple locations can be used to quantify plasma edge conditions and recycling sources and to calibrate plasma-edge modeling codes. The large number of discrete spatial channels required dictates the design of a compact detection system called the filterscope array, which can detect visible lines of plasma impurities as well as the D_α line.[323] This design utilizes photomultiplier tubes with built-in high voltage power supplies and signal amplifiers. The phototubes and associated electronics are built into compact modules, with each module capable of handling many photomultiplier tubes. Light from the plasma is imaged onto optical fibers and transmitted to the filterscope array, which is remotely located in a low radiation area. Fiber optic splitters are used to divide the light into 3-5 paths, each of which is coupled to an optical bandpass filter and a photomultiplier tube. This allows signals from the same plasma sightline to be simultaneously recorded at several wavelengths. The time evolution of the intensities of D_α, D_β, D_γ, C^{2+}, Li, O^+, B^+, and H^+ lines are recorded for every discharge. Signals are digitized at rates up to 100 kHz, allowing the study of edge localized modes (ELMs) and scrapeoff layer (SOL) turbulence. D_α data from a tangential array of eight detectors on the midplane of DIII-D have been inverted, yielding neutral atom densities[324-325] and ionization rate profiles in the plasma edge and SOL, as well as snapshots of edge turbulence[326] with high time resolution. Most major tokamaks are equipped with filterscopes or functionally equivalent systems.

Visible plasma light is collected and focused onto the optical fibers by a lens located outside a window on the vacuum vessel. This sightlines for the DIII-D upper and lower divertor filterscopes are shown in Fig. 41. Light from each fiber is split into 5 channels by a fiber-optic splitter, as shown in Fig. 42. After being split, the light is imaged onto a one-inch-diameter optical band-pass filter. The filters are mounted in holders which are attached to the photomultiplier tubes. The bandpass of the D_α and D_β filters is 1 nm and that of the C^{2+} and He^+ filters is typically 2 nm. The filtered light is detected by photomultiplier tubes and amplified for output to the data acquisition system. The signal gain is controlled via the photomultiplier high voltage, which is remotely controlled. Typical data are shown in Fig. 43.[327]

Measurements with filterscopes or photodiodes with spectral bandpass filters have contributed significantly to the understanding of ELMS. A recent review article by Hill[328] on ELMs describes many of these measurements. On JET, divertor impurity sources and bremsstrahlung emission[329] at 523.5 nm are monitored via interference filter-photomultiplier tube combinations to evaluate the impurity content (Z_{eff}) of the plasma and to determine if additional wall conditioning is required. Monitoring of D_α and He^+ emission during Helium Glow Discharge conditioning is a useful indicator of wall-conditioning that plays a role in obtaining high performance discharges on NSTX.[330]

2. One- and Two-dimensional imaging using filtered cameras

Typical of the visible light imaging systems on tokamaks is the tangential camera used on DIII-D[331] for two-dimensional imaging studies of C^{2+} (465 nm) and D_α (656.3 nm) line emission in the lower divertor region during ELMs. The system views the divertor tangentially from an outer port at approximately the height of the X point. At the tangency plane, the entire divertor from the inner wall to outboard of the DIII-D bias ring is viewed with spatial resolution of 0.5 cm. A charge injection device (CID) camera equipped with an intensifier provides sufficient signal at time resolution of 1-100 μs. The intensifier acts as a fast shutter, photon current converter, and amplifier. A multi-alkali photocathode with broad spectral response (400 and 800 nm) is used. Remotely selectable filters are inserted into the optical path to isolate emission from a single spectral line (C^{2+} or D_α were used during the ELM measurements).[332] Tomographic reconstruction techniques with the assumption of toroidal symmetry were used to obtain two-dimensional (2-D) polodal profiles of the line emission during ELMs. The spatial resolution of the raw data is approximately 5 mm. Binning the raw data into a manageable 640 x 240 element array resulted in overall spatial resolution of 20 mm/pixel in the reconstructed 2-D emission. Fig. 44 shows two examples of the raw 3-D image data of C^{2+} emission (a, c) in ELMy H-mode discharges and their 2-D reconstructions on a poloidal plane (b, d). The C^{2+} emission profiles are significantly different and can be interpreted as an attached (see Fig. 44b) and detached divertor (see Fig. 44d) plasma.

A spectral imaging diagnostic on the MAST spherical torus views the full plasma cross section with up to 256 x 512 chords and at frame rates up to 130 Hz.[333] The narrow bandwidth capability and the wide field of view available is important for monitoring line emission arising due to high energy neutral beam injection. These include D_α emission from the beam fast neutrals and the background neutrals, as well as charge-exchange excited Rydberg transitions in the fuel and impurity ions. High–speed imaging measurements of C^+ have also been performed on Heliotron-J for plasma wall interaction studies[334] and on NSTX by Soukhanovskii *et al.*[335] On the Alcator C-Mod tokamak,[336, 337] a high speed (250 kHz), 300 frame CCD camera has been used to image plasma turbulence. D_2 gas puffs localize the emission in a plane viewed by the camera system, allowing the dynamics of the turbulence in the vicinity of the separatrix to be studied.

One-dimensional imaging of deuterium and impurity line emission in the divertor and scrapeoff regions of MFE plasmas has been performed using linear CCD camerass and photodiode arrays. Such measurements have the advantage over 2-D imaging of providing high spatial resolution (the detectors typically have 512-2048 pixels) and sub-millisecond time resolution. For example, two 2048 pixel linear CCD cameras are used on NSTX to image D_α, C^{2+}, and He^+ line emission from the lower divertor region and the horizontal midplane on NSTX with ~1 mm spatial resolution and 208 μs time resolution.[335]

E. H/D/T relative concentration measurements via grating spectrometers and Fabry-Perot interferometers

1. Line Shape Analysis

Understanding the behavior of deuterium atoms in divertor regions is necessary to the control of fuelling and pumping in fusion plasmas. Recently, knowledge of atomic and molecular processes in divertor regions has become more important, as a gas target regime is considered to be a possible way to control the heat load on the divertor tiles in a tokamak reactor.[338, 339] The shape of the deuterium line emission from the divertor region contains information on the velocity distribution of the deuterium atoms and their recycling processes. The velocity distribution of the atoms determines their penetration depth into the plasma. Understanding of the emission processes of the deuterium lines is necessary to utilize measurements for diagnosis of divertor plasmas.

In the TFR tokamak, the ratio of hydrogen atom flux to deuterium atom flux was obtained from measurements of hydrogen and deuterium lines at high spectral resolution using a Fabry–Perot interferometer.[340] In TEXTOR, the profiles of the H and D lines emitted in front of limiters have been observed with high-resolution spectrometers and analyzed using Monte Carlo calculations.[341-343] The tritium line has been observed in studies of recycling and isotope exchange in the TFTR D-T-experiments.[344] On JT-60U, Kubo *et al.*[345] have investigated the spectral profiles of the D_α line emitted from the divertor region via a high-resolution spectrometer. This spectrometer[346] uses a Littrow lens with a 1.2 m focal length and 100 mm diameter. An echelle grating ruled at 79 g/mm is used to obtain high spectral resolution by working at high spectral order. The dispersed light is detected by an image intensified CCD camera. The D_α profile was explained as being composed of narrow and broad components; the narrow component is attributed to dissociative excitation and electron collisional excitation of the atoms produced by dissociation, and the broad component is attributed to electron collisional excitation of the atoms produced by reflection and charge exchange.

In a similar experiment on the Tore Supra tokamak, the shape of the D_α Balmer line was analyzed to produce information on the velocity distribution of atoms in ergodic divertor plasmas.[347, 348] The line profiles are analyzed by a model that includes the Zeeman splitting and Doppler broadening. This analysis also shows that two deuterium populations (cold and warm) are present. The cold population has an apparent temperature of 1.4 – 2.5 eV, whereas the warm component has a temperature of 22 eV.

2. Recombination

Enhanced three-body recombination and Stark broadening of the Balmer series lines of hydrogen emitted from the divertor region has been observed near the density limit in several tokamaks, such as Alcator C-Mod[349], ASDEX-U[350], and DIII-D.[351] If strongly recombining regions exist, it is important for understanding the physics of divertor plasmas that they be identified. The spectra due to electron collisional excitation, collisional-radiative (three-body) recombination, and molecular-assisted recombination are all expected to exhibit distinctive signatures, which permit the dominant process producing hydrogen emission to be identified. On JET, spatially resolved measurements of the deuterium Balmer series emission in the outer leg of the divertor have been made using a high resolution Czerny-Turner spectrometer which directly viewed the divertor in the 200nm – 400 nm region.[352] Measurements on JET have been made in a variety of high density, detaching plasmas for various divertor geometries of increasing closure. Fig. 45 shows a representative spectrum near the Balmer series limit prior to detachment (56.85 s) and during detachment (60.75 s). During detachment the transitions n = 5-2 to 13-2 are observed as unblended lines and higher transitions are observed to the series limit. Those emitted from high-n states are substantially broadened due to the Stark effect and there is a marked change in the continuum level between 370 – 395 nm.[352, 353] Stark broadening is analyzed to obtain radial distributions of the electron density across the JET outer divertor target plate. The maximum density exceeds 5 x 10^{20} m^{-3} and is correlated with the strike point prior to detachment.

3. High resolution spectroscopy of D_α and T_α using Fabry-Perot interferometers

Control of the D-T isotopic ratio and limiting helium ash content are the key to creating and optimizing the fuel burn in a fusion reactor, such as ITER. Preferential isotope enrichment is also an important indicator of particle confinement processes. In addition, knowledge of the H-D ratio is important for optimization of ion cyclotron radio frequency (ICRF) heating on present experiments, and measurement of the H-D-T relative concentrations will be needed for ICRF heating in ITER. Measurements of the relative and absolute concentrations of hydrogen, deuterium, and tritium have been performed in JET and TFTR D-T experiments. On TFTR, Skinner, *et al.*[344, 354] developed a diagnostic system to measure the D-T concentration which utilizes a Fabry-Perot interferometer to scan the visible Balmer-α line emission from deuterium and tritium, which are excited in the plasma scrape-off layer. The TFTR Fabry-Perot interferometer system is shown in Fig. 46. Light from TFTR was collected by a telescope and transmitted via a fiber to a Fabry-Perot interferometer. The telescope views a region on the TFTR inboard limiter at the midplane. The Zeeman effect splits the H_α, D_α, and T_α lines into an unshifted π component, polarized parallel to the field direction and two σ components polarized perpendicular to the field. A polarizing filter was placed in front of the telescope lens and oriented to transmit only the unshifted π component. The light was recollimated and transmitted through a pre-filter to select a 0.7 nm band centered at the D_α wavelength. It was then observed with a scanning Fabry-Perot interferometer with a wavelength resolution of 0.023 nm. Fig. 47 shows a TFTR spectrum before T was introduced and simulations are shown for the addition of 6% and 24% T. On TFTR the T concentration rose to 11% after 8 tritium-only neutral beam discharges. Analysis of the Doppler broadened line profiles revealed overall agreement with the dissociation, charge exchange, sputtering, and reflection velocities predicted by the neutral

Monte-Carlo code DEGAS with some deficiency in the treatment of dissociation products in the 10- 100 eV range. The T_α line was measurable on TFTR at concentrations, $T_\alpha /(H_\alpha+D_\alpha+T_\alpha)$, down to about 2%.

A variation on this technique was used on JET to measure the T concentration in the subdivertor utilizing a modified Penning gauge.[355] The Penning discharge provided a source of electrons to excite the neutral hydrogen, deuterium, and tritium in the pumping duct. Visible light was collected in an optical fiber bundle and detected in a remotely-located, high resolution Czerny-Turner spectrometer equipped with a fast CCD camera. The intensity of the line emission (H_α, D_α, and T_α) is directly proportional to the partial pressure of the emitting species in the divertor. The line intensity from each isotope is calibrated as a function of pressure. The ratio of the line intensities thus provides a direct measurement of the D-T isotopic ratio. The lower limit for the determination of the D-T isotopic ratio is about 0.5%. This system is applicable for the pressure range from 10^{-5} mbar to a few times 10^{-2} mbar. On TFTR, the D_α and T_α lines blended together and become unresolved due to Doppler broadening of the D_α and T_α lines at the scrapeoff temperature of 20-30 eV. This limited the determination of the tritium concentration in TFTR. On the other hand, the modified Penning gauge produces a very cold plasma discharge (about 5 eV), yielding narrow, well-resolved spectral lines for both D_α and T_α. This permitted measurement of lower tritium concentrations on JET than was possible on TFTR.

F. Projections to ITER diagnostics

1. Overview

The difficulties of implementing optical diagnostics in the environment of a burning plasma experiment such as ITER are discussed in detail in another article in this issue. Thus, we give only a brief overview of the main issues and possible solutions here. The difficulties for optical diagnostic components on ITER arise primarily from two sources. First, the long pulse length of the machine (1000 s) will result in high thermal loads on optical components near the plasma, and large erosion or deposition of plasma-facing optical components, depending on location. Second, the nuclear environment in the vicinity of the plasma gives rise to a range of radiation-induced effects such as radio-luminescence/radiation-darkening of transmission optics and transmutation/distortion of sensors. Heat loads from the long pulse length at the first wall of ITER are expected to be 0.5 MW/m^2 and neutron fluxes will be 3×10^{18} n/m^2s, preventing the use of refractive optical components close to the plasma. Optical diagnostics will make use of mirrors and shielding labyrinths to bring the light to locations where windows, lenses, and fiber optics can be used. Fiber optics are particularly vulnerable to radiation darkening and luminescence, due to the large optical path length through the fiber material. Mirrors facing the plasma will be subjected to fluxes of escaping ions, charge-exchange, and sputtered neutral atoms. Depending on their location, mirrors will therefore become either coated with layers of carbon or beryllium or their surface layers will be eroded. Single crystal metal mirrors (e. g., tungsten or molybdenum) show good survivability in erosion conditions and the surface retains its smoothness and hence good reflectivity. Such mirrors appear suitable for first mirrors on ITER. Protection against contamination by the use of shutters and/or in-situ cleaning techniques will still be required where mirrors are subject to deposition rather than erosion. In addition, *in* *situ* mirror monitoring and calibration techniques will be needed to compensate for changes in mirror properties due to erosion and deposition.

2. Fibers

Fibers made from high purity fused silica offer good tolerance to radiation darkening, and operation at elevated temperature or doping with hydrogen further improves radiation tolerance by annealing color center formation in the glass. Fig. 48 shows the luminescence and loss of transmission of fibers due to neutron irradiation during deuterium-tritium operation on TFTR.[356] The luminescence and total neutron production rate are shown in Fig. 48(a). The observed luminescence in a fiber is linearly proportional to neutron rate up to 2.2×10^{18} s^{-1}, which corresponds to a near-vessel neutron flux of 4.4×10^{16} $n\text{-}m^{-2}\text{-}s^{-1}$ and a radiation dose rate of 11 Gy/s. Fig. 48(b) shows the loss in transmission compared with the total neutron production during the same shot; the transmission loss accumulates during the shot. The change in transmission during a shot presents a serious problem for data analysis, as it decreases the apparent amplitude of continuum measurements such as visible bremsstrahlung, and it distorts the measured spectral line shape if the transmission changes as the detector pixels are being read out. Similar results for attenuation of signals due to neutrons have been reported on JET.[296]

Radiation induced loss of transmission (or browning) of the fibers can be reduced by thermal annealing.[356] This is extensively used on JET for optical fibers during D-T operation.[357] The first 25 m of the quartz fiber, which are within the JET biological radiation shield, are protected by an aluminum jacket and enclosed in a metal insulated tube, which is heated to 250° C to prevent transmission loss by annealing out the color centers as they form. On JET, the fiber transmission and possible luminescence of the fibers has been monitored from shot to shot and no significant effect was observed. However, even with thermal annealing, the use of optical fibers on ITER will be restricted to relatively low-radiation areas away from the first wall.

3. Mirrors and lenses

The first mirror for ITER diagnostics should be metallic to withstand the thermal loads.[358] In the region of 200-500 nm, the reflectivity of Mo is better than that of Cu and W and the sputtering yield for deuterium is relatively low.[359, 360] Thus, Mo appears to be a good choice for a first mirror in the ITER divertor cassette. Neutral particle bombardment of the first mirror can also degrade the performance. Baffle plates can be installed in front of the mirror to reduce the number of particles bombarding the mirror but this decreases the solid angle seen by the mirror.

The potential use of carbon in the ITER divertor will present a problem that is common in present experiments, namely the need to estimate light transmission efficiency through deposited layers on windows. The layers have been observed to grow in time during an experimental campaign on Tore Supra.[361] Modeling and measurements indicate that carbon deposited on mid-plane viewing windows is probably generated by transient events such as ELMs, disruptions or plasma start-up / shut-down, rather than by steady deposition from the well-confined plasma.[362]

4. Neutron and γ-ray irradiation effects on viewing windows

The viewing windows located at the ITER first wall will be protected against overheating by water-cooled stainless-steel tubes. The neutron flux and γ-ray dose rates at the windows are expected to be 6×10^{11} m^{-2} s^{-1} and 3 Gy/h. The degradation of the transmission (λ >350 nm) of KU fused silica is less than 5% (8 mm thickness) at a neutron fluence of 10^{21} m^{-2} and a γ-ray dose of 10^7 Gy.[358] Thus, the windows are expected to survive lifetime ITER operation (50,000 shots × 1000 s) for $\lambda > 350$ nm. For the 200 - 350 nm wavelength region, the windows will survive the γ-ray irradiation. More detailed analysis is necessary to determine the effect of neutron irradiation.

VI. Synchrotron Radiation Measurements of Runaway Electrons

Relativistic electrons in tokamak discharges are collisionless and can therefore be confined long enough to be accelerated to energies up to tens of MeV. These high-energy "runaway" electrons are a concern for burning plasma experiments such as ITER because they can be generated and then expelled from the plasma during a disruption, possibly causing severe, localized damage to plasma-facing components.[364,365] Thus, development of a runaway electron diagnostic is important. Runaway electrons are seen in present-day tokamaks during low density ($n_e < 10^{19}$ m^{-3}) operation and during disruptions. The spectrum of the synchrotron radiation emitted by runaway electrons as they orbit the torus in the presence of the toroidal magnetic field provides a means of measuring the runaway energy, pitch angle, runaway current, and beam radius.

The use of synchrotron radiation to diagnose runaway electrons has been developed on TEXTOR and TEXTOR-94 by Finken[366] and Jaspers.[367] Analytic expressions for the runaway synchrotron radiation spectrum emitted by runaway electrons in a tokamak plasma are given by Pankratov.[368] The formalism of Schwinger[369] for radiation from electrons in a circular orbit is used, with an approximate instantaneous orbital radius. Fig. 49 shows the synchrotron radiation spectrum for a single electron calculated for TEXTOR-94 and for ITER for various values of the electron energy, w, and pitch angle, θ (defined as the ratio of the components of the electron velocity perpendicular and parallel to the magnetic field).[367] The radiation is emitted in the infrared region and peaks between 5 μm and 15 μm, depending on electron energy and pitch angle. It can therefore be detected by the standard infrared cameras used for measuring the temperature of surfaces inside the vacuum vessel. Because the electrons are relativistic, the radiation is emitted in a narrow cone in the forward direction of the electron motion. The camera must therefore have a tangential view into the direction of electron motion. Fig. 50 shows three images taken using a tangentially-viewing infrared camera during a low-density discharge in TEXTOR-94. The camera sensitivity and long wavelength cutoff of the viewing optics allowed measurements in the 3-8 μm range. The first image (A) was taken before the runaway electron population developed and therefore shows the background emission due to heating of plasma-facing surfaces. The second image (B) shows the early development of the synchrotron radiation and the third image (C) shows the fully developed synchrotron radiation. The runaway energy, pitch angle, runaway current, and beam radius were deduced from these images.[367]

For ITER, it appears that the optimum spectral region for observation of runaway electrons with energies up to 50 MeV is 1-5 μm.[367] The choice of spectral region is influenced by the need to distinguish the synchrotron radiation from the background thermal and bremsstrahlung radiation. Because the spectrum at wavelengths shorter than the peak wavelength is very steep, as shown in Fig. 49, measurements in two spectral regions below the peak wavelength would allow the maximum electron energy to be accurately determined.

VII. Conclusion and Outlook

Measurements using passive spectroscopic diagnostic techniques have played an important role in advancing understanding of the physics of MFE plasmas from the early days of fusion research to the present. Many of the techniques described here have become standard and are routinely used on a variety of MFE devices. Development of new passive spectroscopy diagnostics for present-day experiments continues, e. g. x-ray crystal spectrometers with 2-D detectors and optical soft x-ray arrays. However, the major new challenge for these diagnostics is their implementation on burning plasma devices, such as ITER. The problems due to the burning plasma environment have been discussed. Solutions to these problems are not always apparent and significant research and development is needed to find acceptable solutions.

Acknowledgments

The authors would like to thank the referees for providing many helpful suggestions which improved this paper. This work was supported by the US Department of Energy under Contract No. DE-AC02-76CH03073 with the Princeton Plasma Physics Laboratory and Contract No. DE-AC05-00OR22725 with the Oak Ridge National Laboratory.

References

1. H. R. GRIEM, *Principles of Plasma Spectroscopy*, Cambridge University Press, UK (1997).
2. A, THORNE, U. LITZÉN, and S. JOHANSSON, *Spectrophysics*, Springer-Verlag, Berlin (1999).
3. R. C. ISLER, "Impurities in Tokamaks", *Nucl. Fusion*, **24**, 1599 (1984).
4. C. DE MICHELIS and M. MATTIOLI, "Soft X-Ray Diagnostics of Laboratory Plasmas", *Nucl. Fusion*, **21**, 677 (1981).
5. C. DE MICHELIS and M. MATTIOLI, "Spectroscopy and Impurity Behavior in Fusion Plasmas", *Rep. Prog. Phys.*, **47**, 1233 (1984).
6. R. W. P. MCWHIRTER and H. P. SUMMERS, "Atomic Radiation from Low Density Plasma", *Applied Atomic Collision Physics,* vol. 2, Plasmas, Academic Press, New York (1984).
7. N. J. PEACOCK, "Diagnostics Based on Emission Spectra", *Applied Atomic Collision Physics,* vol. 2, Plasmas, Academic Press, New York (1984).
8. N. J. PEACOCK, "Fusion Spectroscopy", *Astrophysics and Space Science*, **237**, 341 (1996).
9. T. LOVEGROVE *et al.*, *in Proceedings of the 22nd European Conference on Controlled Fusion and Plasma Physics, Bournemouth, 1995, Europhysics Conference Abstracts* Vol. 19C (The European Physical Society, Geneva, 1995) p. III-301.
10. J. L. TERRY *et al.*, "Volume Recombination and Opacity in Alcator C-Mod Plasmas", *Phys. Plasmas*, **5**, 1759 (1998).
11. M. L. ADAMS *et al.*, "Application of Magnetically Broadened Hydrogenic Line Profiles to Computational Modeling of a Plasma Experiment", *J. Quant Spect. Rad. Transfer*, **71**, 117 (2001).
12. LISGO *et al.*, "OSM-EIRENE Moeling of Neutral Pressures in the Alcator C-Mod Divertor", *J. Nucl. Mater.*, **337-339**, 139 (2005).
13. B. LIPSCHULZ *et al.*, "Ultrahigh Densities and Volume Recombination inside the Separatrix of the Alcator C-Mod Tokamak", *Phys. Rev. Lett.*, **81**, 1007 (1998).
14. H. P. SUMMERS, "Atomic Data and Analysis Structure – User Manual', JET Joint Undertaking Report JET-IR(94)06 (1987).
15. H. P. SUMMERS *et al.,* "Atomic Data for Modelling Fusion and Astrophysical Plasmas", *Plasma Phys. Control. Fusion*, **44**, B323 (2002).
16. M. O'MULLANE, University of Strathclyde, Personal Communication (January 2005).
17. L. LAURO-TARONI, *et al.*, "Impurity Transport of High Performance Discharges in JET" *in Proc. 21st EPS Conference on Controlled Fusion and Plasma Physics, Montpellier*, vol. 1, p. 102 (1994).
18. J. E. RICE *et al.,* "X-Ray and VUV Observations of Mo^{23+}-Mo^{33+} Brightness Profiles from Alcator C-Mod Plasmas", *J. Phys. B*, **29**, 2191 (1996).
19. J. READER *et al.,* "Wavelengths and Transition Probabilities for Atoms and Atomic Ions, Part I. Wavelengths. Part II. Transition Probabilities", *Nat. Stand. Ref. Ser., Natl. Bur. Stand.* **68** (1980). These tables also appear in the *CRC Handbook of Chemistry and Physics* and on-line at http://physics.nist.gov/PhysRefData.

20. R. L. KELLY, “Atomic and Ionic Spectrum Lines Below 2000 Angstroms: Hydrogen through Krypton”, J. Phys. Chem. Ref. Data, **16** Suppl. 1 (1987). These tables also appear on-line at http://physics.nist.gov/PhysRefData.
21. http://www.pa.uky.edu/~peter/atomic/
22. http://cfa-www.harvard.edu/amdata/ampdata/ampdb.shtml
23. http://cfa-www.harvard.edu/amdata/ampdata/amdata.shtml
24. http://www.pmp.uni-hannover.de/cgi-bin/ssi/test/kurucz/sekur.html
25. W. J. KARZAS and R. LATTER, “Electron Radiative Transitions in a Coulomb Field”, *Astrophysical Journal Suppl. Ser.* **6**, 167 (1961).
26. S. VON GOELER *et al.,* Thermal X-Ray Spectra and Impurities in the ST Tokamak”, *Nucl. Fusion*, **15**, 301 (1975).
27. A. WELLER, Max Planck Institut für Plasmaphysik, Personal Communication (January 2005).
28. A. WELLER *et al.*, “Modelling of Soft X-Ray Emission from JET Plasmas”, JET Joint Undertaking Report JET-IR(87) (1987).
29. J. A. R. SAMSON, *Techniques of Vacuum Ultraviolet Spectroscopy,* John Wiley and Sons, Inc., New York (1967).
30. J. A. R. SAMSON and D. L. EDERER, *Vacuum Ultraviolet Spectroscopy I,* Academic Press, San Diego (1998).
31. R. J. FONCK, A. T. RAMSEY, and R. V. YELLE, “Multichannel Grazing-Incidence Spectrometer for Impurity Diagnosis”, *Appl. Opt.,* **21**, 2115 (1982).
32. T. KITA, T. HARADA, and H. KURODA, “Mechanically-Ruled Abberation-Corrected Concave Gratings for a Flat-Field Grazing Incidence Spectrograph”, *Appl. Opt.,* **22**, 512 (1983).
33. W. BIEL *et al.*, “Design of a High-Efficiency Extreme Ultraviolet Overview Spectrometer System for Plasma Impurity Studies on the Stellarator Experiment Wendelstein 7-X”, *Rev. Sci. Instrum.*, **75**, 3268 (2004).
34. C. DAVIS, *Davis, Lasers and Electro-Optics*, Cambridge University Press, Cambridge, UK (1996).
35. M. BASS, *Handbook of Optics*, *Vol. 1*, Optical Society of America (1995).
36. R. E. BELL, M. FINKENTHAL, and H. W. MOOS, “Time-Resolving Extreme Ultraviolet Spectrograph for Fusion Diagnostics”, *Rev. Sci. Instrum.,* **52**, 1806 (1981).
37. W. HODGE, B. C. STRATTON, and H. W. MOOS, “Grazing Incidence Time-Resolving Spectrograph for Magnetic Fusion Plasma Diagnostics”, *Rev. Sci. Instrum.*, **55**, 16 (1984).
38. J. L. SCHWOB, A. W. WOUTERS, and S. SUCKEWER, “High-Resolution Duo-Multichannel Spectrometer for Tokamak Plasma Diagnostics”, *Rev. Sci. Instrum.*, **58**, 1601 (1987).
39. P. BEIERSDORFER *et al.*, “Grazing-Incidence Spectrometer for Soft X-Ray and Extreme ultraviolet Spectroscopy on the national Spherical Torus Experiment” *Rev. Sci. Instrum.,* **77**, 10F306 (2006).
40. K. KONDO *et al.*, “Visible and VUV Spectroscopic Diagnostics on Heliotron E”, *Rev. Sci. Instrum.*, **59**, 1533 (1988).
41. H. KUBO *et al.,* “Multichordal Spectroscopy on JT-60”, *Rev. Sci. Instrum.*, **59**, 1515 (1988).

42. H. NAGATA *et al.,* "Module-Type Flat-field Grazing-incidence Spectrographs for Large Tokamak (JT-60) Plasma Diagnosis", *Nucl. Instrum. And Methods in Phys. Res.,* **A294**, 292 (1990).
43. N. YAMAGUCHI *et al.,* "Space-Resolving Flat-Field Vacuum Ultraviolet Spectrograph For Plasma Diagnostics", *Rev. Sci. Instrum.*, **65**, 3408 (1994).
44. A. R. FIELD *et al.*, "A Spatially Scanning Vacuum Ultraviolet and Visible Range Spectrometer for Spectroscopy of Tokamak Plasmas in ASDEX-Upgrade", *Rev. Sci. Instrum.*, **66**, 5433 (1995).
45. F. G. MEJIER, "A High Resolution Vacuum Ultraviolet Spectrometer for Plasma Spectroscopy", *Meas. Sci. Technol.*, **10**, 367 (1999).
46. M. YOSHIKAWA *et al.*, "Space-Resolving VUV and Soft X-Ray Spectroscopy in the Tandem Mirror GAMMA 10 Plasma", *Surface Review and Letters*, **9,** 555 (2002).
47. V. PIFFL *et al.*, "VUV Imaging Seya-Namioka Spectrometer", *Czech J. Phys. Suppl. D*, **52**, D70 (2002).
48. S. MORITA and M. GOTO, "Space-Resolved VUV Spectroscopy Using the 3 m Normal Incidence Spectrometer with Back-Illuminated CCD detector in the LHD", *Rev. Sci. Instrum.*, **74**, 2036 (2003).
49. B. C. STRATTON *et al.,* "SPRED Spectrograph Upgrade: High-Resolution Grating and Improved Absolute Calibrations", *Rev. Sci. Instrum.*, **57**, 2043 (1986).
50. A. NUDELFUDEN, R. SOLANKI, and H. W. MOOS, "Spatial Imaging in the Soft X-Ray Region (20-304 Å) Utilizing the Astigmatism of the Grazing Incidence Concave Grating", *Appl. Opt.,* **24**, 789 (1985).
51. D. CONTENT, D. WROBLEWSKI, M. PERRY, and H. W. MOOS, "Space- and Time-Resolving Spectrograph for High-Temperature Plasma Diagnostics", *Rev. Sci. Instrum.*, **57**, 2041 (1986).
52. K. J. MCCARTHY *et al.,* "A Toroidal Focusing Mirror Based Vacuum Ultraviolet Diagnostic for TJ-II", *Rev. Sci. Instrum.*, **70**, 312 (1999).
53. E. HINNOV and F. W. HOFFMANN, "Measurement of Absolute Radiation Intensities in the Vacuum Ultraviolet Region", *J. Opt. Soc. Am.*, **53**, 1259 (1963).
54. E. B. SALOMAN, "Absolute Radiometric Calibration of Detectors between 200-600 Å", *Appl. Opt.,* **14**, 1391 (1975).
55. B. C. STRATTON, R. J. FONCK, and A. T. RAMSEY, "Synchrotron Radiation Calibration of the SPRED VUV Spectrograph at the NBS SURF II Electron Storage Ring", SPIE Proceedings, vol. 689, pp. 77-81, "X-Ray Calibration: Techniques, Sources, and Detectors", P. D. Rockett and P. Lee, eds., (San Diego, 1986) (SPIE, 1986).
56. Y. OKAMOTO *et al.*, "Absolute Calibration of Space- and Time-Resolving Flat-Field Vacuum Ultraviolet Spectrograph Under Both P and S Polarized Light Conditions for Plasma Diagnostics", *Rev. Sci. Instrum.*, **72**, 4366 (2001).
57. M. MAY *et al.,* "Photometric Calibration of an EUV Flat Field Spectrometer at the Advanced Light Source", *Rev. Sci. Instrum.*, **74**, 2011 (2003).
58. M. YOSHIKAWA *et al.,* "Absolute Calibration of Vacuum Ultraviolet Spectrograph System for Plasma Diagnostics", *Rev. Sci. Instrum.*, **75**, 4088 (2004).
59. J. M. BRIDGES and W. R. OTT, "Vacuum Ultraviolet Radiometry. 3: The Argon Mini-arc as a New Secondary Standard of Spectral Radiance", *Appl. Opt.,* **16**, 367 (1977).
60. K. DANZMANN *et al.*, "High Current Hollow Cathode as a Radiometric Transfer Standard Source for the Extreme Vacuum Ultraviolet", *Appl. Opt.,* **27**, 4947(1988).

61. V. A. SOUKHANOVSKII *et al.,* “Compact Collimated Vacuum Ultraviolet Diagnostics for Localized Impurity Measurements in Fusion Boundary Plasmas”, *Rev. Sci. Instrum.*, **72**, 3270 (2001).
62. B. BLAGOJEVIC *et al.,* “Imaging Transmission Grating Spectrometer for Magnetic Fusion Experiments”, *Rev. Sci. Instrum.*, **74**, 1988 (2003).
63. V. A. SOUKHANOVSKII *et al.,* “Development of Phosphor Scintillator-Based Detectors for Soft X-Ray and Vacuum Ultraviolet Spectroscopy of Magnetically Confined Fusion Plasmas”, *Rev. Sci. Instrum.*, **74**, 4331 (2003).
64. S. HOKIN, R. FONCK, and P. MARTIN, “A Simple Multifoil Spectrometer for Routine Carbon and Oxygen Measurements”, *Rev. Sci. Instrum.*, **63**, 5038 (1992).
65. D. STUTMAN *et al.*, “Line Emission Tomography for CDX-U Using Filtered Diodes”, *Rev. Sci. Instrum.*, **68**, 1059 (1997).
66. C. SUZUKI, B. J. PETERSON, and K. IDA, “Measurement of Impurity Emission Profiles in CHS Plasma Using AXUV Photodiode Arrays and VUV Bandpass Filters”, *Rev. Sci. Instrum.*, **75**, 4142 (2004).
67. R. KORDE, J. S. CABLE, and L. R. CANFIELD, “One Gigarad Passivating Nitrided Oxides for 100% Internal Quantum Efficiency Silicon Photodiodes”, *IEEE Trans. Nucl. Sci.,* **40**, 1655 (1993).
68. V. A. SOUKHANOVSKII *et al.,* “Multilayer Mirror and Foil Filter AXUV Diode Arrays on CDX-U Spherical Torus”, *Rev. Sci. Instrum.*, **72**, 737 (2001).
69. D. S. GRAY *et al.,* “Time Resolved Radiated Power During Tokamak Disruptions and Spectral Averaging of AXUV Photodiode Response on DIII-D”, *Rev. Sci. Instrum.*, **75**, 376 (2004).
70. J. H. UNDERWOOD and T. W. BARBEE, “Layered Synthetic Microstructures as Bragg Diffractors for X Rays and Extreme Ultraviolet: Theory and Predicted Performance”, *Appl. Opt.*, **20**, 3027 (1981).
71. A. P. ZWICKER *et al.,* “Peak Reflectivity Measurements of W/C, Mo/Si, and Mo/B_4C Multilayer Mirrors in the 8-190 Å Range Using both K_α Line and Synchrotron Radiation”, *Appl. Opt.*, **29**, 3694 (1990).
72. M. J. MAY *et al.,* “Measurements of Molybdenum Radiation in the Alcator C-Mod Tokamak Using a Multilayer Mirror Soft X-Ray Polychromator”, *Rev. Sci. Instrum.*, **66**, 561 (1995).
73. D. STUTMAN *et al.,* “Multilayer Mirror Based Line Emission Tomography for Spherical Tokamaks”, *Rev. Sci. Instrum.*, **68**, 1055 (1997).
74. D. STUTMAN *et al.,* “High Throughput Ultrasoft X-Ray Polychromator for Embedded Impurity Pellet Injection Studies”, *Rev. Sci. Instrum.*, **76**, 013508 (2005).
75. D. STUTMAN *et al.,* “Ultrasoft X-Ray Telescopes for Fluctuation Imaging in Fusion Plasmas”, *Rev. Sci. Instrum.*, **72**, 732 (2001).
76. K. KADOTA, M. OTSUKA, and J. FUJITA, “Space and Time-Resolved Study of Impurities by Visible Spectroscopy in the High-Density Regime of JIPP T-II Tokamak Plasma”, *Nucl. Fusion*, **20**, 209 (1980).
77. A. T. RAMSEY and S. L. TURNER, “HAIFA: A Modular, Fiber-Optic Coupled, Spectroscopic Diagnostic for Plasmas”, *Rev. Sci. Instrum.*, **58**, 1211 (1987).
78. H. NOZATO *et al.,* “Measurement of Bremsstrahlung Profile with a High-Spatial Resolution on LHD”, *J. Plasma Fusion Res. SERIES*, **5**, 442 (2002).

79. H. NOZATO *et al.,* "A Study of Charge Dependence of Particle Transport Using Impurity Pellet Injection and High-Spatial Resolution Bremsstrahlung Measurement on the Large Helical Device", *Phys. Plasmas.*, **11**, 1920 (2004).
80. E. S. MARMAR *et al*., "High Resolution Visible Continuum Imaging Diagnostic on the Alcator C-Mod tokamak", *Rev. Sci. Instrum.*, **72**, 940 (2001).
81. P. G. CAROLAN *et al.,* "High Definition Imaging in the Mega Amp Spherical Torus from Soft X-Rays to Infrared (invited)", *Rev. Sci. Instrum.*, **75**, 4069 (2004).
82. H. MEISTER *et al.,* "Z_{eff} from Spectroscopic Bremsstrahlung Measurements at ASDEX Upgrade and JET", *Rev. Sci. Instrum.*, **75**, 4097 (2004).
83. H. RÖHR *et al.,* "Measurement of Zeff Profiles from Bremsstrahlung Emission in the Near Infrared", *Rev. Sci. Instrum.*, **59**, 1875 (1988).
84. K.-H. STEUER *et al.,* "Bremsstrahlung Measurements in the Near Infrared on ASDEX", *Rev. Sci. Instrum.*, **61**, 3084 (1990).
85. F. ORSITTO *et al.,* "Z_{eff} Profiles from Bremsstrahlung Emission in the Near Infrared Spectral Region", *Rev. Sci. Instrum.*, **70**, 925 (1999).
86. J. K. ANDERSON *et al.,* "Direct Removal of Edge-Localized Pollutant Emission in a Near-Infrared Bremsstrahlung Measurement", *Rev. Sci. Instrum.*, **74**, 2107 (2003).
87. V. VOITSENYA *et al.,* "Diagnostic Mirrors for Burning Plasma Experiments (invited)", *Rev. Sci. Instrum.*, **72**, 475 (2001).
88. N. J. PEACOCK *et al.,* "Spectroscopy for Impurity Control in ITER", *Diagnostics for Experimental Thermonuclear Fusion Reactors*, Plenum Press, New York, 1996.
89. N. C. HAWKES *et al.,* "XUV and VUV Spectroscopy of ITER", *Diagnostics for Experimental Thermonuclear Fusion Reactors 2*, Plenum Press, New York, 1998.
90. K. W. HILL *et al.,* "Analysis of Nuclear-Radiation-Induced Noise in Spectroscopic and X-Ray Diagnostics during High-Power Deuterium-Tritium Experiments on the Tokamak Fusion Test Reactor", *Rev. Sci. Instrum.*, **66**, 913 (1995).
91. R. BARNSLEY *et al.,* "JET Beamline with Integrated X-Ray, VUV, and Visible Spectrometers for Burning Plasma Experiments", *Rev. Sci. Instrum.*, **74**, 1969 (2003).
92. I. H. COFFEY *et al.,* "First Operation of ITER-Prototype VUV Spectroscopy on JET", *Rev. Sci. Instrum.*, **75**, 3737 (2004).
93. K. EBISAWA *et al.,* "Vacuum Ultraviolet Impurity Monitor for the International Thermonuclear Experimental Reactor", *Rev. Sci. Instrum.*, **70**, 328 (1999).
94. D. R PARSIGNAULT *et al.,* "A Shielded, Multichannel, Extreme Ultraviolet Spectrograph for Fusion Plasma Diagnostics", *Rev. Sci. Instrum.*, **64**, 1014 (1993).
95. L. RODRÍGUEZ-BARQUERO *et al.,* "Preparation and Characterization of Pixelated Phosphor Screens for High-Resolution Imaging in the Vacuum Ultraviolet and X-Ray Ranges", *Rev. Sci. Instrum.*, **75**, 3998 (2004).
96. D. STUTMAN *et al.,* "Spectroscopic Imaging Diagnostics for Burning Plasma Experiments", *Rev. Sci. Instrum.*, **76**, 023505-1 (2005).
97. J. D. JOANOPOULOS, P. R. VILLENEUVE, and S. FAN, "Photonic Crystals: Putting a New Twist on Light", *Nature*, **386**, 143 (1997).
98. M. IBANESCU *et al.,* "An All-Dielectric Coaxial Waveguide", *Science*, **289**, 415 (2000).
99. S. A. FLODSTROM and R. Z. BACHRACH, "Simple Far UV Transmission Grating Monochromator for Use with Resonance Radiation Lamps", *Rev. Sci. Instrum.*, **47**, 1464 (1976).

100. P. J. CALDWELL, E. T. ARAKAWA, and T. A. CALLCOTT, "Extreme Ultraviolet Transmission Grating Spectrometer", *Appl. Opt.,* **20**, 3047 (1981).
101. L. KIPP *et al.,* "Sharper Images by Focusing Soft X-Rays with Photon Sieves", *Nature*, **414**, 184 (2001).
102. J. M. BENDICKSON *et al.,* "Metallic Surface-Relief On-Axis and Off-Axis Focusing Diffractive Cylindrical Mirrors", *J. Opt. Soc. Am. A*, **16**, 113 (1999).
103. S. P. REGAN *et al.,* "An Evaluation of Multilayer Mirrors for the Soft X-Ray and Extreme Ultraviolet Wavelength Range that were Irradiated with Neutrons", *Rev. Sci. Instrum.*, **68**, 757 (1997).
104. F. C. JAHODA *et al.*, "Continuum Radiation in the X-Ray and Visible Regions from a Magnetically Compressed Plasma (Scylla)," *Phys. Rev.* **119**, 843, (1960).
105. S. VON GOELER, W. STODIEK, and N. SAUTHOFF, "Studies of Internal Disruptions and m = 1 Oscillations in Tokamak Discharges with Soft X-Ray Techniques," *Phys. Rev. Lett.* **33**, 1201 (1974).
106. EQUIPE TFR, "Electron Temperature and Z_{eff} Measurements in the Hot Plasma of TFR by Soft X-Ray Analysis", *Nucl. Fusion* **17**, 213 (1977).
107. S. VON GOELER, "Soft X-Ray Measurements", *Diagnostics for Fusion Experiments*, E. Sindoni and C. Wharton, eds., Pergamon, New York (1979).
108. M. BITTER *et al.*, "Doppler-Broadening Measurements of X-Ray Lines for Determination of the Ion Temperature in Tokamak Plasmas", *Phys. Rev. Lett.* **42**, 304 (1979).
109. K. W. HILL *et al.*, "Tokamak Fusion Test Reactor X-Ray Imaging Diagnostic", *Rev. Sci. Instrum.* **56**, 830 (1985).
110. K. MCGUIRE *et al.*, "Diagnostic Applications of the TFTR XIS System", *Rev. Sci. Instrum.* **57**, 2136 (1986).
111. S. VON GOELER *et al.*, "Tangential Imaging for Fluctuation Studies", *Rev. Sci. Instrum.* **61**, 3055 (1990).
112. R. D. GILL *et al.*, "Soft X-Ray Measurements of the Impurity Density in DITE", *Nucl. Fusion* **19**, 1003 (1979).
113. K. BRAU *et al.*, "Observations of Giant Recombination Edges on the Princeton Large Torus Tokamak Induced by Particle Transport", *Phys. Rev.* **A22**, 2769, (1980).
114. E. H. SILVER *et al.*, "Soft X-Ray Measurements from the PDX Tokamak", *Rev. Sci. Instrum.* **53**, 1198 (1982).
115. S. VON GOELER, *et al.*, "X-Ray Diagnsotics for TFTR", *in Proceedings of the Course on Diagnostics for Fusion Reactor Conditions*, Varenna, Italy, September 1982, Vol. I, p 69.
116. J. E. RICE *et al.*, "Continuum X-Ray Emission from the Alcator A Tokamak", *Phys. Rev.* **A25**, 1645, (1982).
117. K. W. HILL *et al.*, "Tokamak Fusion Test Reactor Prototype X-Ray Pulse-Height Analyzer Diagnostic", *Rev. Sci. Instrum.* **56**, 840 (1985).
118. S. SESNIC *et al.*, "Measurement of the Wall Radiation in the Soft X-Ray Region in PDX", *Rev. Sci. Instrum.* **56**, 1160 (1985).
119. K. W. HILL *et al.*, "Studies of Impurity Behavior in TFTR", *Nucl. Fusion* **26**, 1131 (1986).
120. D. PASINI *et al.*, "JET X-Ray Pulse-Height Analysis System", *Rev. Sci. Instrum.* **59**, 693 (1988).
121. T. CHO *et al.*, "X-Ray Studies of Various Shapes of Electron-Velocity Distribution Functions and of Electron Confinement Affected by Kilovolt-Range Electrostatic Potentials", *Phys. Rev.* **A45**, 2532, (1992).

122. S. MUTO *et al.*, “First Measurements of Hard X-Ray Spectrum Emitted from High-Energy Electrons in Electron-Cyclotron Heated Plasmas of LHD”, *Rev. Sci. Instrum.* **74**, 1993 (2003).
123. Y. SHI *et al.*, “Application of Avalanche Photodiode for Soft X-Ray Pulse-Height Analyses in the HT-7 Tokamak”, *Nucl. Instrum. Meth.* **A488**, 566 (2002).
124. R. O’CONNELL *et al.*, “Measurement of Fast Electron Distribution Using a Flexible, High Time-Resolution Hard X-Ray Spectrometer”, *Rev. Sci. Instrum.* **74**, 2001 (2003).
125. AMPTEK Corporation, http://www.amptek.com/
126. C. S. ROSSINGTON, J. T. WALTON, and J. M. JAKELVIC, “Si(Li) Detectors with Thin Dead Layers for Low Energy X-ray Detection”, *IEEE Trans. Nucl. Sci*. **38**, 239 (1991).
127. P. LECHNER *et al.*, “Novel High Resolution Silicon Drift Detectors”, *X-Ray Spectrometry* **33**, 256 (2004).
128. A. LONGONI *et al.*, “A Portable XRF Spectrometer for Non-Destructive Analyses in Archaeometry”, *Nucl. Instrum. Meth.* **A409**, 407 (1998).
129. Y. SHI *et al.*, “Soft X-Ray Pulse Height Analyzer in the HT-7 Tokamak”, *Rev. Sci. Instrum.* **75**, 4930 (2004).
130. Z. Y. CHEN *et al.*, “A Compact Soft X-Ray PHA in the HT-7 Tokamak”, *Nucl. Instrum. Meth.* **A527**, 604 (2004).
131. Y LIANG *et al.*, “Energy and Spatial Resolved Measurement of Soft X-Ray Emission with Photon Counting X-Ray Charge Coupled Device Camera in Compact Helical System”, *Rev. Sci. Instrum.* **71**, 3711 (2000).
132. Y LIANG *et al.*, “Photon Counting CCD Detector as a Tool of X-Ray Imaging”, *Rev. Sci. Instrum.* **72**, 717 (2001).
133. J. M. R. CARDOSO *et al.*, “A Portable XRF Spectrometer for Non-Destructive Analyses in Archaeometry”, *Nucl. Instrum. Meth.* **A422**, 400 (1999).
134. D. STUTMAN *et al.*, “Ultrasoft X-Ray Imaging System for the National Spherical Tokamak Experiment”, *Rev. Sci. Instrum.* **70**, 572 (1999).
135. P. FRANZ *et al.*, “Compact Soft X-Ray Multichord Camera: Design and Initial Operation”, *Rev. Sci. Instrum.* **74**, 2152 (2003).
136. E. T. POWELL, R. KAITA, and R. J. FONCK, “Technique for Relating Internal Plasma Shape to Plasma Current Profiles in Noncircular Tokamaks”, *Rev. Sci. Instrum.* **61**, 3301 (1990).
137. V. A. VERSHKOV and S. V. MIRNOV, “Role of Impurities in Current Tokamak Experiments”, *Nucl. Fusion* **14**, 383 (1974).
138. G. L. JAHNS *et al.*, “Dynamic Behavior of Intrinsic Impurities in Doublet III Discharges”, *Nucl. Fusion* **22**, 1049 (1978).
139. R. PETRASSO *et al.*, “Fully Ionized and Total Silicon Abundances in the Alcator-C Tokamak”, *Phys. Rev. Lett.* **49**, 1826 (1982).
140. F. H. SEGUIN *et al.*, “Effects of Internal Disruptions on Impurity Transport in Tokamaks”, *Phys. Rev. Lett.* **51**, 455 (1983).
141. R. D. PETRASSO *et al.*, “Using X-Ray Arrays to Measure Impurity Transport in the Alcator-C tokamak”, *Rev. Sci. Instrum.* **56**, 843 (1985).
142. A. COMPANT LA FONTAINE *et al.*, “Q = 1 Magnetohydrodynamic Activity in PLT Studied with Aluminum Impurity Injection as a Diagnostic Tool”, *Plasma Phys. Control. Fusion* **27**, 229 (1985).

143. K. W. WENZEL and R. D. PETRASSO, “X-ray Imaging Arrays for Impurity-Transport Studies on the Texas Experimental Tokamak”, *Rev. Sci. Instrum.* **61**, 693 (1990).
144. H. WEISEN *et al.*, “Measurement of Light Impurity Densities and Z_{eff} in JET using X-Ray Tomography”, *Rev. Sci. Instrum.* **62**, 1531 (1991).
145. L. MARRELLI *et al.*, “Development and Tests of a Simple Multifoil Spectrometer for Highly Time-Resolved Line Intensity Measurements in the RFX Experiment”, *Meas. Sci. Technol.* **6**, 1690 (1995).
146. D. STUTMAN *et al.*, “Integrated Impurity Diagnostic Package for Magnetic Fusion Experiments”, *Rev. Sci. Instrum.* **74**, 1982 (2003).
147. L. A. SHMAENOK *et al.*, “Novel Instrumentation for Spectrally Resolved Soft X-Ray Plasma Tomography: Development and Pilot Results on TEXTOR”, *Rev. Sci. Instrum.* **72**, 1411 (2001).
148. M. DE BOCK *et al.*, “Measuring One-Dimensional and Two-Dimensional Impurity Density Profiles on TEXTOR using Combined Charge-Exchange, Beam-Emission Spectroscopy and Ultrasoft X-Ray Tomography”, *Rev. Sci. Instrum.* **75**, 4155 (2004).
149. H. TAKENAGA *et al.*, “Relationship Between Particle and Heat Transport in JT-60U Plasmas with Internal Transport Barrier”, *Nucl. Fusion* **43**, 1235 (2003).
150. H. KUBO *et al.*, “Radiation Enhancement and Impurity Behavior in JT-60U Reversed Shear Discharges”, *J. Nucl. Mater.* **313-316**, 1197 (2003).
151. T. P. DONALDSON, “Theory of Foil-Absorption Techniques for Plasma X-Ray Continuum Measurements”, *Plasma Phys.* **20**, 1279 (1978).
152. J. KIRALY *et al.*, “Fast Multichannel Electron-Temperature Diagnostic for TFTR Using X-Ray Imaging”, *Rev. Sci. Instrum.* **56**, 827 (1985).
153. J. KIRALY *et al.*, “Multichord Time Resolved Electron Temperature Measurements by the X-Ray Absorber Foil Method on TFTR”, *Nucl. Fusion* **27**, 397 (1987).
154. R. T. SNIDER, “Active Silicon X-Ray Filter for Measuring Electron Temperature”, *Rev. Sci. Instrum.* **66**, 546 (1995).
155. P. MARTIN, A. MURARI, and L. MARRELLI, “Electron-Temperature Measurements with High Time Resolution in RFX”, *Plasma Phys. Control. Fusion* **38**, 1023 (1996).
156. R. K. PAUL *et al.*, “Electron-Temperature Estimation in the Saha Institute of Nuclear Physics Tokamak from the Soft X-Ray Imaging System”, *Rev. Sci. Instrum.* **69**, 1378 (1998).
157. A. MURARI *et al.*, “An Optimized Multifoil Soft X-Ray Spectrometer for the Determination of the Electron Temperature with High Time Resolution”, *Rev. Sci. Instrum.* **70**, 581 (1999).
158. A. WELLER, C. GORNER, and D. GONDA, “X-ray Diagnostics on WENDELSTEIN 7-AS”, *Rev. Sci. Instrum.* **70**, 484 (1999).
159. R. BARTIROMO *et al.*, “Electron-Temperature Diagnostics in the RFX Reversed Field Pinch Experiment”, *Plasma Phys. Control. Fusion* **42**, 881 (2000).
160. H. KOGUCHI *et al.*, “Spatially Resolved Bolometric Measurement and Electron-Temperature Measurement using Diode Arrays”, *Rev. Sci. Instrum.* **75**, 4007 (2004).
161. H. A. B. BODIN, “The Reversed Field Pinch”, *Nucl. Fusion* **30**, 1717 (1990).
162. J. S. SARFF *et al.*, “Tokamak-Like Confinement at a High Beta and Low Toroidal Field in the MST Reversed Field Pinch”, *Nucl. Fusion* **43**, 1684 (2003).
163. R. KAITA and S. SESNIC, “Mode Number Identification with a Soft X-Ray Array”, *Rev. Sci. Instrum.* **68**, 750 (1997).

164. B. C. STRATTON *et al.*, "Initial Operation of the National Spherical Torus Experimental Fast Tangential Soft X-Ray Camera", *Rev. Sci. Instrum.* **75**, 3959 (2004).
165. D. PACELLA, R. BELLAZZINI, A. BREZ, and M. FINKENTHAL, "Energy Resolved Two-Dimensional X-Ray Imaging for MFE Plasmas", *Rev. Sci. Instrum.* **75**, 3926 (2004).
166. L. DELGADO-APARICIO *et al.,* "Optical" Soft X-Ray Arrays for Fluctuation Diagnostics in Magnetic Fusion Energy Plasmas", *Rev. Sci. Instrum.*, **75**, 4020 (2004).
167. L. DELGADO-APARICIO, The Johns Hopkins University, Personal Communication (January 2007).
168. K. W. HILL *et al.*, "ITER X-Ray Diagnostic Studies," *Rev. Sci. Instrum.* **63**, 5032 (1992).
169. D. PARSIGNAULT and A. S. KRIEGER, "X-Ray Fiber Optics from 60 eV to 10 keV", in *X-Ray Detector Physics and Applications*, edited by R. Hoover (SPIE, Bellingham 1992), Proc. SPIE, San Diego, CA, 16-24 July, 1992, Vol. 1736.
170. D. H. BILDERBACK, "Review of Capillary X-Ray Optics from the 2nd International Capillary Optics Meeting," *X-Ray Spectrom.* **32**, 195 (2003).
171. BJEOUMIKHOV *et al.*, "New Generation of Polycapillary Lenses: Manufacture and Applications," *X-Ray Spectrom.* **32**, 172 (2003).
172. M. GOLDMAN *et al.*, "Gridded Ionization Chamber for Detection of X-Ray Wave Activity in Tokamak Plasmas," *Rev. Sci. Instrum.* **56**, 349 (1985).
173. K. YAMASHITA *et al.*, "Supermirror Hard-X-Ray Telescope," *Appl. Opt.* **37**, 8067 (1998).
174. R. M. AMBROSI *et al.*, "Point Spread Function and Centroiding Accuracy Measurements with the JET-X Mirror and MOS CCD Detector of the SWIFT Gamma-Ray-Burst Explorer's X-Ray Telescope," *Nucl. Instrum. Meth.* **A488**, 543 (2002).
175. D. N. BURROWS *et al.*, "The *SWIFT* X-Ray Telescope," *Space Sci. Rev.* **120**, 165 (2005).
176. V. K. SYSOEV, "Design of the SODART Multimirror X-Ray Telescope," *J. Opt. Technol.* **73**, 42 (2006).
177. K. D. JOENSEN *et al.*, "Design of Grazing-Incidence Multilayer Supermirrors for Hard-X-Ray Reflectors," *Appl Opt.* **34**, 7935 (1995).
178. P. HOGHOJ *et al.*, "Focusing of Hard X Rays with a W/Si Supermirror," *Nucl. Instrum. Meth.* **B132**, 528 (1997).
179. K. D. JOENSEN *et al.*, "Broad-Band Hard X-Ray Reflectors," *Nucl. Instrum. Meth.* **B132**, 221 (1997).
180. B. L. HENKE *et al.*, "X-Ray Interactions: Photoabsorption, Scattering, Transmission, and Reflection at E = 50-30,000 eV, Z = 1-92," *At. Dat. Nucl. Dat. Tab.* **54**, 181 (1993).
181. E. SILVER *et al.*, "An NTD Germanium-Based Microcalorimeter with 3.1 eV Energy resolution at 6 keV," *Nucl. Instrum. Meth.* **A545**, 683 (2005).
182. F. S. PORTER *et al.*, "High Resolution X-Ray Microcalorimeters," *Nucl. Instrum. Meth.* **A559**, 436 (2006).
183. C. HOLLERITH *et al.*, "Energy-Dispersive X-Ray Spectroscopy with Microcalorimeters," *Nucl. Instrum. Meth.* **A520**, 606 (2004).
184. R. FUJIMOTO *et al.*, "TES Microcalorimeter Development for Future Japanese X-Ray Astronomy Missions," *Nucl. Instrum. Meth.* **A520**, 431 (2004).
185. K. SHINOZAKI *et al.*, "Soft X-Ray Measurement of the Toroidal Pinch Experiment RX Reversed Field Pinch Plasma using Transition Edge Sensor Calorimeter," *Rev. Sci. Instrum.* **77**, 043104 (2006).
186. M. P. BRUIJN *et al.*, "Development of and Array of Transition-Edge Sensors for Application in X-Ray Astronomy," *Nucl. Instrum. Meth.* **A520**, 443 (2004).

187. S. FRIEDRICH *et al.*, “A Multichannel Superconducting Tunnel Junction Detector for High Resolution X-Ray Spectroscopy of Magnesium Diboride Films,” IEEE Trans. Appl. Superconductivity **13**, 1114 (2003).
188. M. A. LINDEMAN *et al.*, “Performance of Compact TES Arrays with Integrated, High Fill-Fraction X-Ray Absorbers,” *Nucl. Instrum. Meth.* **A520**, 411 (2004).
189. J. COTTAM *et al.*, “Characterization of the Astro-E2 X-Ray Spectrometer,” *Nucl. Instrum. Meth.* **A520**, 368 (2004).
190. C. K. STAHLE *et al.*, “Cosmic Ray Effects in Microcalorimeter Arrays,” *Nucl. Instrum. Meth.* **A520**, 472 (2004).
191. G. C. HILTON *et al.*, “X-Ray Microcalorimeter Arrays Fabricated by Surface Micromachining,” *Nucl. Instrum. Meth.* **A520**, 435 (2004).
192. C. A. KILBOURNE, “The Science and Technology of Microcalorimeter Arrays,” *Nucl. Instrum. Meth.* **A520**, 402 (2004).
193. Y. ISHISAKI *et al.*, “Performance Analyses of TES Microcalorimeters with Mushroom Shaped X-Ray Absorbers made of Sn or Bi,” *Nucl. Instrum. Meth.* **A520**, 452 (2004).
194. P. GORENSTEIN and S. MICKIEWICZ, “Reduction of Cosmic Background in an X-Ray Proportional Counter through Risetime Discrimination,” *Rev. Sci. Instrum.* **39**, 816 (1968).
195. S. VON GOELER *et al.*, “X-Ray Analysis of NonMaxwellian Distributions (Current Drive)”, *in proceedings on the Course on Diagnostics for Fusion Reactor Conditions, Varenna, Italy, 1982, edited by P. Stott et al.* (Commission of the European Communities, Brussels 1983) Vol. I, p. 87-107.
196. S. VON GOELER *et al.*, “X-Ray Spectroscopy on Tokamaks”, *in proceedings on the Course on Diagnostics for Fusion Reactor Conditions, Varenna, Italy, 1982, edited by P. Stott et al.* (Commission of the European Communities, Brussels 1983) Vol. I, p. 109-127.
197. S. VON GOELER *et al.*, “X-Ray Measurements on the ST Tokamak”, *in Proc. of European Conference on Controlled Fusion and Plasma Physics, Vol. II, p. 71 – 73, Lausanne, September 1-5, 1975.*
198. A. L. MERTS, R. D. COWAN, and N. H. MAGEE, JR., LASL report LA-6220-MS (1976).
199. K. W. HILL *et al.*, “Determination of Fe Charge-State Distributions in the Princeton Large Torus by Bragg Crystal Spectroscopy”, *Phys. Rev. A* **19**, 1770 (1979).
200. H. JOHANN, “Intense X-Ray Spectra Obtained with Concave Crystals”, *Z. Phys*. **69**, 185 (1931).
201. A. H. GABRIEL, “Dielectronic Satellite Spectra for Highly Charged Helium-Like Ion Lines”, *Mon. Not. R. Astr. Soc.*, **160**, 99 (1972).
202. C. P. BHALLA, A. H. GABRIEL, and L. P. PRESNYAKOV, “Dielectronic Satellite Spectra for Highly-Charged Helium-Like Ions – II Improved Calculations”, *Mon. Not. R. Astr. Soc.* **172**, 359 (1975)
203. L. A. VAINSHTEIN and U. I. SAFRANOVA, “Wavelengths and Transition Probabilities of Satellites to Resonance lines of H- and He-like ions”, *Atomic Data and Nuclear Data Tables* **21**, 49 (1978).
204. F. BELY-DUBAU, A. H. GABRIEL, and S. VOLANTÉ, “Dielectronic Satellite Spectra for Highly-Charged Helium-Like Ions - III. Calculations of *n=3* solar flare iron lines”, *Mon. Not. R. Astr. Soc.* **186**, 405 (1979)
205. F. BELY-DUBAU, A. H. GABRIEL, and S. VOLANTÉ, “Dielectronic Satellite Spectra for Highly-Charged Helium-Like Ions - V. Effect of total satellite contribution on the solar flare iron spectra”, *Mon. Not. R. Astr. Soc.* **189**, 801 (1979).

206. F. BELY-DUBAU, J. DUBAU, P. FAUCHER, and A. H. GABRIEL, “Dielectronic Satellite Spectra for Highly-Charged Helium-Like Ions - VI. Iron spectra with improved inner-shell and helium-like excitation rates”., *Mon. Not. R. Astr. Soc.* **198**, 239 (1982).
207. M. BITTER *et al.*, “Dielectronic Satellite Spectrum of Heliumlike Iron (Fe XXV)”, *Phys. Rev. Lett.*, **43**, 129 (1979).
208. P. PLATZ *et al.*, “High-Throughput, High-Resolution Soft X-Ray Crystal Spectrometer for Tokamak Plasma Studies”, *J. Phys. E: Sci. Instrum.* **14**, 448 (1981).
209. TFR GROUP, J. DUBAU, and M. LOULERGE, “High-Resolution Spectra from Inner-Shell Transitions in Highly-Ionised Chromium (Cr XIX-XXIII)”, *J. Phys. B: At. Mol. Phys.* **15**, 1007 (1982).
210. TFR GROUP, F. BOMBARDA, F. BELY-DUBAU, *et al.*, “Dielectronic Satellite Spectrum of Heliumlike Argon: A Contribution to the Physics of Highly-Charged Ions and Plasma Impurity Transport”, *Phys. Rev. A* **32**, 2374 (1985).
211. TFR GROUP, M. CORNILLE, J. DUBAU, and M. LOULERGE, “Charge-Dependent Wavelength Shifts and Line Intensities in the Dielectronic Satellite Spectrum of Helium-Like Ions”, *Phys. Rev. A* **32**, 3000 (1985).
212. P. PLATZ, M. CORNILLE, and J. DUBAU, “High-Precision Wavelength Measurements of X-Ray Lines Emitted from TS-Tokamak Plasmas”, *J. Phys. B: At. Mol. Opt. Phys.* **29**, 3787 (1996).
213. P. PLATZ *et al.*, “X-Ray Line Diagnostics on the Tore Supra Tokamak”, *Rev. Sci. Instrum.* **70**, 308 (1999).
214. A. ROMANNIKOV *et al.*, “Measurement of Central Toroidal Rotation in Ohmic Tore Supra Plasmas”, *Nucl. Fusion* **40**, 319 (2000)
215. P. PLATZ *et al.*, “Toroidal Velocity and Ripple Losses in Tore Supra with LH, ICRF, and Combined Additional Heating”, *in Proceedings of the 22nd European Conference on Controlled Fusion and Plasma Physics, Bournemouth, 1995, Europhysics Conference Abstracts* Vol. 19C (The European Physical Society, Geneva, 1995) p. III-337.
216. P. PLATZ *et al.*, “Determination of Absolute Metal Densities in Tore Supra”, *in Proceedings of the 22nd European Conference on Controlled Fusion and Plasma Physics, Bournemouth, 1995, Europhysics Conference Abstracts* Vol. 19C (The European Physical Society, Geneva, 1995) p. II-385.
217. L. VON HÁMOS, “X-Ray Spectroscopy with Curved Crystalline Reflectors”, *Ann. Phys.* **17**, 716 (1933).
218. J. RICE *et al.*, “Five Chord High Resolution X-Ray Spectrometer for Alcator C-Mod”, *Rev. Sci. Instrum.* **61**, 2753 (1990).
219. J. RICE *et al.*, “Observations of Alcator C-Mod Plasmas from a Five Chord High Energy Resolution X-Ray Spectrometer Array”, *Rev. Sci. Instrum.* **66**, 752 (1995).
220. J. RICE *et al.*, “The Dependence of Core Rotation on Magnetic Configuration and the Relation to the H-mode Power Threshold in Alcator C-Mod Plasmas with no Momentum Input”, *Nucl. Fusion* **45**, 251 (2005).
221. J. RICE *et al.*, “Toroidal Rotation and Momentum Transport in Alcator C-Mod Plasmas with no Momentum Input”, *Phys. Plasmas* **11**, 2427 (2004).
222. J. RICE *et al.*, “Observations of Anomalous Momentum Transport in Alcator C-Mod Plasmas with no Momentum Input”, *Nucl. Fusion* **44**, 379 (2004).
223. W. D. LEE *et al.*, “Observation of Anomalous Momentum Transport in Tokamak Plasmas with No Momentum Input”, *Phys. Rev. Lett.* **91**, 205003 (2003).

224. J. RICE *et al.*, “Double Transport Barrier Plasmas in Alcator C-Mod”, *Nucl. Fusion* **42**, 510 (2002).
225. R. BARTIROMO *et al.*, “Time Resolving Bent Crystal Spectrometer for Tokamak Plasma Diagnostics”, *Nucl. Instrum. & Meth. In Phys. Res*. **225**, 378 (1984).
226. A. H. GABRIEL and K. J. H. PHILLIPS, “Dielectronic Spectra for Highly Charged Helium-Like Ions – IV. Iron Satellite Lines as a Measure of Non-Thermal Electron Energy Distributions”, *Mon. Not. R. Astron. Soc.* **189**, 319 (1979).
227. R. BARTIROMO, F. BOMBARDA, and R. GIANNELLA, “Spectroscopic Study of Nonthermal Plasmas”, *Phys. Rev. A* **32**, 531 (1985).
228. R. BARTIROMO *et al.*, “Space Resolving Bent Crystal Spectrometer for FTU”, ISPP-9 International School of Plasma Physics ’Piero Caldirola’, Diagnostics for Contemporary Fusion Experiments, Proceedings of the Workshop, P. E. Stott, D. K. Akulina, G. Gorini, and E. Sindoni (Eds.) SIF Bologna 1991, p. 959-966.
229. R. BARTIROMO, “X-Ray Spectroscopy”, ISPP-9 International School of Plasma Physics ’Piero Caldirola’, Diagnostics for Contemporary Fusion Experiments, Proceedings of the Workshop, P. E. Stott, D. K. Akulina, G. Gorini, and E. Sindoni (Eds.) SIF Bologna 1991, p. 377-406.
230. K. W. HILL *et al.*, “Tokamak Fusion Test Reactor Horizontal High-Resolution Bragg X-Ray Spectrometer (Abstract)”, *Rev. Sci. Instrum.* 56,1165 (1985).
231. M. BITTER *et al.*, “Vertical High-Resolution Bragg X-Ray Spectrometer for the Tokamak Fusion Test Reactor”, *Rev. Sci. Instrum.* **57**, 2145 (1986).
232. M. BITTER *et al.*, “Measurements of Radial Profiles of the Ion Temperature and Plasma Rotation Velocity with the TFTR Vertical X-Ray Crystal Spectrometer”, *Rev. Sci. Instrum.* **59**, 2131 (1988).
233. R. BARTIROMO *et al.*, “JET High Resolution Bent Crystal Spectrometer” *Rev. Sci. Instrum.* **60**, 237 (1989).
234. M. BITTER *et al.*, “High Power Neutral Beam Heating Experiments on TFTR with Balanced and Unbalanced Momentum Input”, *Plasma Physics and Controlled Fusion* **29**, 1235 (1987).
235. F. BOMBARDA *et al.*, “Observations and Comparisons with Theory of the Heliumlike and Hydrogenlike Resonance Lines and Satellites of Nickel from the JET Tokamak”, *Phys. Rev. A* **37**, 504 (1987).
236. M. MATTIOLI *et al.*, Impurity Ion Temperature and Toroidal Rotation Velocity in JET from High-Resolution X-Ray and XUV Spectroscopy”, *Journal of Applied Physics* **64**, 3345 (1988).
237. K.-D. ZASTROW, E. KÄLLNE, and H.P. SUMMERS, “Measurement and Comparison with Theory of the Temperature Dependence of Satellite-to-Resonance Line Ratios of Heliumlike Nickel from the JET Tokamak”, *Phys. Rev A* **41**, 1427 (1990)).
238. M. BITTER *et al.*, “Satellite Spectra for Heliumlike Titanium. II” *Phys, Rev. A* **32**, 3011 (1985).
239. M. BITTER *et al.*, “X-Ray Diagnostics of Tokamak Plasmas”, *Physica Scripta* **T47**, 87 (1993).
240. H. HSUAN *et al.*, “Satellite Spectra of Heliumlike Nickel”, *Phys. Rev. A* **35**, 4280 (1987).
241. H. HSUAN *et al.*, “Measurements of the Ion Temperature and Plasma Rotation from K_{α} Emission with the TFTR Horizontal X-Ray Crystal Spectrometer”, *Rev. Sci. Instrum.* **59**, 2127 (1988).

242. M. BITTER *et al.*, Satellite Spectra of the K_{α} Resonance Line of Heliumlike Nickel, Ni XXVII, from Tokamak-Fusion-Test-Reactor Plasmas: Comparison Between Theory and Experiment", *Phys. Rev. A* **44**, 1796 (1991).
243. M. BITTER *et al.*, "Spectrum of Heliumlike Krypton from Tokamak Fusion Test Reactor Plasmas", *Phys. Rev. Lett.* **71**, 1007 (1993).
244. S. MORITA and M. GOTO, "X-Ray Crystal Spectrometer with a Charge-Coupled Device Detector for Ion Temperature Measurements in the Large Helical Device" *Rev. Sci. Instrum.***74**, 2375 (2003).
245. S. MORITA, M. GOTO, S. MUTO, H, NOZATO, and LHD EXPERIMENTAL GROUP, "Introduction of LHD Spectroscopy", *in Proc, 13th International Stellarator Workshop, Canberra, Australia (2002), PIIA/13*
246. S. MORITA *et al.*, Experimental Study on Ion Temperature Behaviors in ECH, ICRF and NBI H_2, He and Ne Discharges of the Large Helical Device", *Nucl. Fusion* **43**, 899 (2003).
247. S. MORITA and M. GOTO *et al.*, "Behavior of Ion Temperature in Electron and Ion Heating Regimes Observed with ECH, NBI and ICRF Discharges of LHD", *Nucl. Fusion* **42**, 1179 (2002).
248. G. BERTSCHINGER *et al.*, "X-Ray Spectroscopy at the TEXTOR-94 Tokamak", *Physica Scripta* **T83**, 132 (1999).
249. J. WEINHEIMER, *et al.*, "High-Resolution X-Ray Crystal Spectrometer/Polarimeter at Torus Experiment for Technology Oriented Research-94", *Rev. Sci. Instrum.* **72**, 2566 (2001).
250. O. MARCHUK *et al.*, "Cascades between Doubly Excited Levels in Helium-Like Argon", *J. Phys. B: At. Mol./ Opt. Phys.* **37**, 1951 (2004).
251. G. BERTSCHINGER *et al.*, "X-ray Spectroscopy at TEXTOR", *Fusion Science and Technology* **47**, 253 (2005).
252. M. BITTER *et al.*, "Imaging X-Ray Crystal Spectrometers for the National Spherical Torus Experiment", *Rev. Sci. Instrum.* **70**, 292 (1999).
253. M. BITTER *et al*, "Results from the National Spherical Torus Experiment X-Ray Crystal Spectrometer", *Rev. Sci. Instrum.* **74**, 1977 (2003).
254. M. BITTER *et al.*, "New Benchmarks from Tokamak Experiments for Theoretical Calculations of the Dielectronic Satellite Spectra of Heliumlike Ions", *Phys. Rev. Lett.* **91**, 265001-1 (2003).
255. P. BEIERSDORFER *et al.*, "Charge-Exchange-Produced *K*-Shell X-Ray Emission from Ar^{16+} in a Tokamak Plasma with Neutral Beam Injection", *Phys. Rev. A* **72**, 032725 (2005).
256. E. S. MARMAR *et al.*, "Precision Measurement of the 1s Lamb Shift in Hydrogenlike Argon", *Phys. Rev. A* **33**, 774 (1986).
257. E. KÄLLNE, *et al.*, "X-ray Satellites of High-*n* Rydberg Transitions in Ar^{16+}", *Phys, Rev. A* **38**, 2056 (1988).
258. J. E. RICE *et al.*, "Observation of Charge-Transfer Population of High-*n* Levels in Ar^{+16} from Neutral Hydrogen in the Ground and Excited States in a Tokamak Plasma", *Phys. Rev. Lett.* **56**, 50 (1986).
259. J. RICE *et al.*, "X-ray Observations of *2l-nl'* Transitions from Zr, Nb, Mo, and Pd in Near-Neonlike Charge States", *Phys. Rev, A* **53**, 3953 (1996).
260. R. BARNSLEY *et al.*, "Versatile High Resolution Crystal Spectrometer with X-Ray Charge Coupled Device Detector", *Rev. Sci. Instrum.* **74**, 2388 (2003).
261. T. E. CRAVENS, "X-Ray Emission from Comets", *Science* **296**, 1042 (2002).

262. M. BITTER *et al.*, “Unresolved Dielectronic Satellites of the Resonance Lines of Heliumlike Iron (Fe XXV)”, *Phys. Rev. Lett.* **47**, 921 (1981).
263. P. BEIERSDORFER *et al.*, “Measurements of the Contributions from High-*n* Dielectronic Satellites to the K_α Resonance Line in Heliumlike Fe^{24+}”, *Rev. Sci. Instrum.* **63**, 5029 (1992).
264. J. DUBAU and M. LOULERGE, “High Resolution Spectra from Inner-Shell Transitions in Highly Ionized Chromium (Cr XIX-XXIII)” *J. Phys. B: At. Mol. Phys.* **15**, 1007 (1982).
265. F. BELY-DUBAU *et al.*, Satellite Spectra for Heliumlike Titanium”, *Phys. Rev. A* **26**, 3459 (1982).
266. M. BITTER *et al.*, “Dielectronic Satellite Spectra of Hydrogenlike Titanium (Ti XXII)”, *Phys. Rev. A* **29**, 661.
267. V. DECAUX *et al.*, “Dielectronic Satellite Spectra of Hydrogenlike Iron from the Tokamak Fusion Test Reactor”, *Phys. Rev. A* **43**, 228 (1991).
268. K. WIDMANN *et al.*, “Measurements of the K_α Transition Energies of Heliumlike Krypton”, *Phys. Rev. A.* **53**, 2200 (1996).
269. M. R. TARBUTT *et al.*, “Wavelength Measurements of the Satellite Transitions to the *n*=2 Resonance Lines of Helium-Like Argon”, *J. Phys. B: At. Mol./Opt. Phys.* **34**, 3979 (2001).
270. C. BIEDERMANN, R. RADTKE, and K. B. FOURNIER, “Spectroscopy of Heliumlike Argon Resonance and Satellite Lines for Plasma Temperature Diagnostics”, *Phys. Rev. E* **66**, 066404-1 (2002).
271. F. BELY-DUBAU *et al.*, “Measurement of the FeXXV Dielectronic Recombination Rate Coefficient in the PLT Tokamak Plasma”, *Phys. Lett.* **93A**, 189 (1983).
272. TFR GROUP *et al.*, “Charge-Dependent Wavelength Shifts and Line Intensities in the Dielectronic Satellite Spectrum of Heliumlike ions”, Phys. Rev. A **32,** 3000 (1985).
273. P. BEIERSDORFER *et al.*, “High-Resolution *n=3* to *n=2* spectra of Neonlike Silver”, *Phys. Rev. A* **34**, 1297 (1986).
274. P. BEIERSDORFER *et al.*, “Experimental Study of the X-Ray Transitions in the Heliumlike Isoelectronic Sequence”, *Phys. Rev A* **40**, 150 (1989).
275. E. KÄLLNE *et al.*, “Precision Measurement of the H-Like X-Ray Spectrum of Cl and the 1*s* Lamb Shift”, *J. Phys. B: At. Mol. Phys.* **17**, L115-lL120 (1984).
276. L.A. VAINSHTEIN and U. I. SAFRONOVA, “Energy Levels of He- and Li-Like Ions (States 1snl, 1s2nl with n=2-5)”, *Physica Scripta* **31**, 519 (1985).
277. P. INDELICATO, “Multiconfiguration Dirac-Fock Calculations of Transition Energies in Two Electron Ions with $10 \leq Z \leq 92$”, *Nucl. Instrum. Methods* **B31**, 14 (1988).
278. P. BEIERSDORFER *et al.*, “X-ray Transitions in Highly Charged Neonlike Ions”, *Phys. Rev. A* **37**, 4153 (1988).
279. R. BARNSLEY *et al.*, “Bragg Rotor Spectrometer for Tokamak Diagnostics”, *Rev. Sci. Instrum.* **57**, 2159 (1986).
280. R. BARTIROMO *et al.*, “High Counting Rate Soft X-Ray Spectrometer for Tokamak Plasma Diagnostics”, *Nucl. Instrum. & Meth. Phys. Res.* **B95**, 537 (1995).
281. D. L. MCKENZIE *et al.*, “Solar Flare Spectra between 7.8 and 23.0 Angstroms”, *Ap. J.* 241, 409 (1980).
282. M. BITTER *et al.*, “Spatially Resolved Spectra from a New X-Ray Imaging Spectrometer for Measurements of Ion and Electron Temperature Profiles (Invited)”, *Rev. Sci. Instrum.* **75**, 3660 (2004).

283. G. BERTSCHINGER *et al.*, "Compact Imaging Bragg Spectrometer for Fusion Devices", *Rev. Sci. Instrum.* **75**, 3727 (2004).
284. G. BERTSCHINGER *et al.*, "Space Resolved Measurements of Plasma Parameters using X-ray Spectra of He-Like Argon" *in proceedings of the 33rd European Physical Society Conference on Plasma Physics, Roma, Italy, June 19-23, 2006*, vol. 30I, P-2.153.
285. S. G. LEE *et al.*, "Research and Development of X-ray Imaging Crystal Spectrometers for KSTAR", *Rev. Sci. Instrum.* **75**, 3693 (2004).
286. Ch. BROENNIMANN *et al.*, "The PILATUS 1M Detector", *J. Synchrotron Rad.*, **13**, 120 (2006).
287. M. BITTER, Ch. BROENNIMANN, E. F. EIKENBERRY, K. W. HILL, A. INCE-CUSHMAN, S. G. LEE, J. E. RICE, and S. SCOTT, in proceedings of 2006 Nuclear Science Symposium, Medical Imaging Conference and 15th International Room Temperature Semiconductor Workshop, October 29-November 4, 2006, San Diego, CA.
288. R. BARNSLEY *et al.*, "Design Study for International Thermonuclear Experimental Reactor High-Resolution X-Ray Spectroscopy Array", *Rev. Sci. Instrum.* **75**, 3743 (2004).
289. P. C. STANGEBY, *The Plasma Boundary of Magnetic Fusion Devices*, Institute of Physics Publishing, Philadelphpia (2000).
290. C. S. PITCHER and P. C. STANGEBY, "Experimental Divertor Physics", *Plasma Phys. Control. Fusion* **39**, 799 (1997).
291. ITER PHYSICS BASIS EDITORS, "Chapter 1: Overview and Summary", *Nucl. Fusion* **39**, 2137 (1999).
292. H. KUBO *et al.*, "Spectroscopic Study of Hydrogen Neutral Behavior in Attached and Detached Divertor Plasmas of JT-60U", *J. Nucl. Mater.* **337-339**, 161 (2005).
293. A. POSPIESZCZYK *et al.*, "Molecular Deuterium Sources in the outer Divertor of JET", *J. Nucl. Mater.* **337-339**, 500 (2005).
294. S. BREZINSEK *et al.*, "Identification of Molecular Carbon Sources in the JET Divertor by Means of Emission Spectroscopy", *J. Nucl. Mater.* **337-339**, 1058 (2005).
295. M. CZERNY and A. F. TURNER, "Astigmatism in Mirror Spectrometers", *Z. Phys.* **61**, 792 (1930).
296. P.D. MORGAN *et al.,* "Spectroscopic Measurements on the Joint European Torus using Optical Fibers to Relay Visible Radiation", *Rev. Sci. Instrum.* **56**, 862 (1985).
297. R.P. SERAYDARIAN *et al.,* "Multichordal Visible/Near-UV Spectroscopy on the DIII-D Tokamak", *Rev. Sci. Instrum.* **59**, 1530 (1988).
298. R.P. SERAYDARIAN *et al.,* "Multichordal Charge Exchange Recombination Spectroscopy on the Doublet III Tokamak", *Rev. Sci. Instrum.* **57**, 155 (1986).
299. K.H. BURRELL *et al.,* "Improved Charge-Coupled Device Detectors for High-Speed, Charge Exchange Spectroscopy Studies on the DIII-D Tokamak", *Rev. Sci. Instrum.* **75**, 3455 (2004).
300. M. STAMP, UKAEA, Personal Communication (January 2006).
301. R.E. BELL, "Exploiting a Transmission Grating Spectrometer", *Rev. Sci. Instrum.* **75**, 4158 (2004).
302. H. OWEN *et al.,* "New Spectroscopic Instrument based on Volume Holographic optical Elements" *in Proceedings of SPIE Conference, Pratical Holography*, vol. 2406, p. 260 (1995).
303. KAISER_OPTICAL_SYSTEMS, Ann Arbor, MI; HTTP://WWW.KOSI.COM/.

304. R.E. BELL *et al.,* "Tokamak Fusion Test Reactor Poloidal Rotation Diagnostic (Invited)", *Rev. Scien. Instrum.* **70**, 821 (1999).
305. D.L. HILLIS *et al.,* "A High Throughput Spectrometer System for Helium Ash Detection on JET", *Rev. Sci. Instrum.* **75**, 3449 (2004).
306. T.M. BIEWER *et al.,* "Edge Rotation and Temperature Diagnostic on the National Spherical Torus Experiment", *Rev. Sci. Instrum.* **75**, 650 (2004).
307. T.N. CARLSTROM *et al.*, "Evidence for the Role of Velocity Shear on the L-H Transition in DIII-D", *Plasma Phys. Controlled Fusion* **44**, A333 (2002).
308. A. GIBSON, "Deuterium-Tritium Plasmas in the Joint European Torus (JET)" Behavior and Implications", *Phys. Plasmas* **5**, 1839 (1998).
309. Y-K PENG and D. STRICKLER, “Features of Spherical Torus Plasmas”, *Nucl. Fusion* **26**, 1839 (1986).
310. T.M. BIEWER *et al.,* “Observations of Anisotropic Ion Temperature in the NSTX Edge during RF Heating” *in proc. of the 31th EPS Conference on Contr. Fusion and Plasma Physics, London, 2004*, Vol. 28G, p. P-2.198..
311. T.M. BIEWER *et al.,* "Edge Ion Heating by Launched High Harmonic Fast Waves in the National Spherical Torus Experiment", *Physics of Plasmas* **12**, 056108 (2005).
312. R.A. BAMFORD *et al.,* "Combination of Multichannel Detection and Fast Time Response in a Multichord Spectrometer", *Rev. Sci. Instrum.* **63**, 4963 (1992).
313. A. GRAF *et al.,* "High Resolution Transmission Grating spectrometer for Edge Toroidal Rotation Measurements of Tokamak Plasmas", *Rev. Sci. Instrum.* **75**, 4165 (2004).
314. M. YOSHINUMA *et al.*, "Observations of Edge Radial Electric Field Transition in LHD Plasmas", *Plasma Phys. Control Fusion* **46**, 1021 (2004).
315. R. ISLER *et al.,* "Carbon Sources in the DIII-D Tokamak", *J. Nucl. Mater.* **313-316**, 873 (2003).
316. R.C. ISLER *et al.,* “Characterization of Impurities in Tokamak Divertor Plasmas from Analysis of Spectral Profiles”, *in Spectral Line Shapes: 16th International Conference on Spectral Line Shapes (Volume 12) - CP645*. (American Institute of Physics, 2002), p.3.
317. R. C. ISLER *et al.,* "Spectroscopic Determinations of Carbon Fluxes, Sources, and Shielding in the DIII-D Divertors", *Phys. Plasmas* **8**, 4470 (2001).
318. A. HUBER *et al.,* "Comparison of Impurity Production, Recycling and Power Deposition on Carbon and Tungsten Limiters in TEXTOR-94", *J. Nucl. Mater.* **290-293**, 276 (2001).
319. R. NEU *et al.,* "Plasma Operation with Tungsten Tiles at the Central Column of ASDEX Upgrade", *J. Nucl. Mater.* **290-293**, 206 (2001).
320. B. LIPSCHULTZ *et al.*, “Operation of Alcator C-Mod with High-Z Plasma Facing Components and Implications”, *Phys. Plasmas*, **13**, 056117 (2006).
321. J. HOWARD *et al.,* "Optical Coherence Techniques for Plasma Spectroscopy (Invited)", *Rev. Sci. Instrum.* **72**, 888 (2001).
322. J. HOWARD, "High-Speed High Resolution Spectroscopy using Spatial-Multiplex Coherence Imaging Techniques (Invited)", *Rev. Sci. Instrum.* **77**, 10F111-1 (2006).
323. R.J. COLCHIN *et al.,* "The Filterscope", *Rev. Sci. Instrum.* **74**, 2068 (2003).
324. R.J. COLCHIN *et al.,* “Method of Neutral Density Determination Near the X-point in DIII-D”, *in proc. of the 25th EPS Conference on Contr. Fusion and Plasma Physics, Praha, 1998*, p. 818.
325. R.J. COLCHIN *et al.,* "Measurement of Neutral Densities near the X Point in the DIII-D Tokamak", 27th EPS Conference on cont. Fusion and Plasma Phys. **24B**, 760 (2000).

326. R.J. COLCHIN *et al.,* "Slow L-H Transition in DIII-D Plasmas", *Phys. Rev. Lett.* **88**, 255002-255001 (2002)
327. R. J. COLCHIN, Oak Ridge National Laboratory, Personal Communication (January 2006).
328. D.N. HILL, "A Review of ELMs in Divertor Tokamaks", *J. Nucl. Mater.* **241-243**, 182 (1997).
329. M. STAMP *et al.,* "Divertor Impurity Sources; Effects of Hot Surfaces and Thin Films on Impurity Production", *J. Nucl. Mater.* **337-339**, 1038 (2005).
330. H. KUGEL *et al.*, "Overview of Impurity Control and Wall Conditioning in NSTX", *J. Nucl. Mater.* **290-293**, 1185 (2001).
331. M.E. FENSTERMACHER *et al.,* "A Tangentially Viewing Visible TV System for the DIII-D Divertor", *Rev. Sci. Instrum.* **68**, 974 (1997).
332. M. GROTH *et al.,* "Diagnosis of Edge Localized Mode Evolution in DIII-D using Fast-Gated CID and Infrared Cameras", *Rev. Scien. Instrum.* **74**, 2064 (2003).
333. A. PATEL *et al.,* "Versatile Multiwavelength Imaging Diagnostic in the MAST Spherical Tokamak", *Rev. Sci. Instrum.* **75**, 4145 (2004).
334. N. NISHINO *et al.,* "High Speed 2-D Image Measurement for Plasma-Wall Interaction Studies", *J. Nucl. Mater.* **337-339**, 1073 (2005).
335. V. A. SOUKHANOVSKII *et al.,* "High-Resolution Spectroscopic Diagnostic for Divertor and Scrape-Off Layer Neutral and Impurity Emission Measurements in the National Spherical Torus Experiment", *Rev. Sci. Instrum.* **74**, 2094 (2003).
336. J. TERRY *et al.,* "Visible Imaging of Turbulence in the SOL of the Alcator C-Mod Tokamak", *J. Nucl. Mater.* **290-293**, 757 (2001)
337. J.L. TERRY *et al.,* "High Speed Movies of Turbulence in Alcator C-Mod", *Rev. Sci. Instrum.* **75**, 4196 (2004).
338. D.E. POST, "A Review of Recent Developments in Atomic Processes for Divertors and Edge Plasmas", *J. Nucl. Mater.* **220-222**, 143 (1995).
339. G. JANESCHITZ *et al.,* "The ITER Divertor Concept", *J. Nucl. Mater.* **220-222**, 73 (1995).
340. TFR GROUP, "Isotope Exchange Experiments on TFR", *J. Nucl. Mater.* **93-94**, 173 (1980).
341. U. SAMM, "Plasma Edge Research on TEXTOR", *Plasma Phys. Control Fusion* **29**, 1321 (1987).
342. U. SAMM *et al.,* "Plasma Edge Physics in the Textor tokamak with Poloidal and Toroidal Limiters", *J. Nucl. Mater.* **162-164**, 24 (1989).
343. D. REITER *et al.,* "Measurement and Monte Carlo Computations of H_α Profiles in Front of a TEXTOR Limiter", *J. Nucl. Mater.* **196-198**, 1059 (1992).
344. C.H. SKINNER *et al.,* "Spectroscopic Diagnostics of Tritium Recycling in TFTR", *Rev. Sci. Instrum.* **66**, 646 (1995).
345. H. KUBO *et al.,* "The Spectral Profile of the D_α Line Emitted from the Divertor Region of JT-60U", *Plasma Phys. Cont. Fusion* **40**, 1115 (1998).
346. H. KUBO *et al.,* "High Resolution Visible Spectrometer for Divertor Study in JT-60U", *Fusion Engineering and Design* **34-35**, 277 (1997).
347. A. ESCARGUEL *et al.,* "Spectral Profile Analysis of the D Alpha Line in the Divertor Region of Tore Supra", *J. Nucl. Mater.* **290-293**, 854 (2001).
348. A. ESCARGUEL *et al.,* "Atomic and Molecular Deuterium Edge Density Evaluation from Spectral Analysis of the D Alpha Line Shape", *Plasma Phys. Control. Fusion* **43**, 1733 (2001).

349. D. LUMMA *et al*., "Radiative and Three-Body Recombination in the Alcator C-Mod Divertor", *Phys. Plasmas* **4**, 2555 (1997).
350. B. NAPIONTEK *et al.,* "Line and Recombination Emission in the ASDEX Upgrade Divertor at High Density" *in the Proc. of the 24th EPS Conference on Control Fusion and Plasma Phys., Berchtesgaden, 1997.*
351. R. C. ISLER *et al.,* "Signatures of Deuterium Recombination in the DIII-D Divertor", *Phys. Plasmas* **4**, 2989 (1997).
352. A. G. MEIGS *et al.,* "Spectroscopic Electron Density Measurements and Evidence of Recombination in High Density JET Divertor Discharges", *in proc. of the 25th EPS Conference on Contr. Fusion and Plasma Physics, Praha, 1998*, p. 373.
353. A. G. MEIGS *et al.,* "Density and Temperature Measurements in Detached Recombining JET Divertors", *in proc. of the 27th EPS Conference on Contr. Fusion and Plasma Physics, Budapest, 2000*, vol. 24B, p. 1264.
354. C. H. SKINNER *et al.,* "Plasma Wall Interaction and Tritium Retention in TFTR", *J. Nucl. Mater.* **241-243**, 214 (1997).
355. D. L. HILLIS *et al.,* "Deuterium-Tritium Concentration Measurements in the Divertor of a Tokamak via a Modified Penning Gauge", *Fusion Engineering and Design* **34-35**, 347 (1997).
356. A. T. RAMSEY, "D-T Radiation Effects on TFTR Diagnostics (Invited)," *Rev. Sci. Instrum.* **66**, 871 (1995).
357. A. T. RAMSEY *et al.*, "Radiation Effects on Heated Optical Fibers" *Rev. Sci. Instrum.* **68**, 632 (1997).
358. D. V. ORLINSKI, *in Diagnostics for Experimental Thermonuclear Fusion Reactors*, edited by P.E. Stott, G. Gorini, and E. Sindoni (Plenum, New York, 1996), p. 51.
359. J. H. WEAVER and H. P. R. FREDERIKSE, *CRC Handbook of Chemistry and Physics* (Chemical Rubber Corp., Boca Raton, FL, 1994).
360. T. SUGIE *et al.*, "Divertor Impurity Monitor for the International Thermonuclear Experimental Reactor", *Rev. Sci. Instrum.* **70**, 351 (1999).
361. S .J. TOBIN, *Carbon Impurity Production and Transport from the Inertially Cooled Horizontal Limiter in the Tore Supra Tokamak*, PhD Thesis, Univ. of Michigan, 1996.
362. C. H. SKINNER *et al.*, "Time Resolved Deposition Measurements in NSTX", *J. Nucl. Mater.* **337-339**, 129 (2005).
363. S. YAMAMOTO *et al.*, "Irradiation Tests on ITER Diagnostic Components" *Diagnostics for Experimental Thermonuclear Fusion Reactors 2*, Plenum Press, New York, 1998.
364. M. N. ROSENBLUTH and S. V. PUTVINSKI, "Theory for Avalanche of Runaway Electrons in Tokamaks", *Nucl Fusion,* **37**, 1355 (1997).
365. S. V. PUTVINSKI, *et al.,* "Halo Current, Runaway Electrons, and Disruption Mitigation in ITER", *Plasma Phys. Control. Fusion,* **39**, B157 (1997).
366. K. H. FINKEN, *et al.,* "Observation of Infrared Synchrotron Radiation from Tokamak Runaway Electrons in TEXTOR", *Nucl. Fusion,* **30**, 859 (1990).
367. R. JASPERS, *et al.,* "A Synchrotron Radiation Diagnostic to Observe Relativistic Runaway Electrons in a Tokamak Plasma", *Rev. Sci. Instrum.*, **72**, 466 (2001). (See also references cited herein.)
368. I. M. PANKRATOV, "Analysis of the Synchrotron Radiation Spectra of Runaway Electrons", *Plasma Phys. Rep.*, **25**, 145 (1999).

369. J. SCHWINGER, “On the Classical Radiation of Accelerated Electrons”, *Phys. Rev.,* **75**, 1912 (1949).

Table I. Spectral Regions Relevant to Spectroscopy of Magnetically-confined Plasmas

Spectral Region	**Wavelength/Energy Region**
Near Infrared	700-1200 nm / 1-2 eV
Visible	400-700 nm / 2-3 eV
Ultraviolet (UV)	200-400 nm / 3-6 eV
Vacuum Ultraviolet (VUV)	30-200 nm / 6-40 eV
Extreme Ultraviolet (EUV)	10-30 nm / 40-120 eV
Soft X-Ray	0.1-10 nm / 120-12000 eV

Table II: Parameter/technique matrix for passive spectroscopy plasma diagnostics.

	Impurity species identification	Impurity densities	Z_{eff}	Electron temperature	Ion temperature	Flow velocity	Electron density	Impurity transport	Particle influxes	H/D/T ratio	MHD modes	Runaway electrons	Described in Section
VUV/EUV grating spectroscopy	✸	✸						✸					II.A
VUV/EUV filtered detectors (inc. multilayer mirrors)		✸						✸					II.B&C
Visible bremsstrahlung			✸				❖						II.D
Pulse height analysis	✪	✸	✪	✪									III.B
Filtered SXR diodes		✸						✸			✸		III.C
SXR crystal spectroscopy	❖	✸		❖	✸	✸		❖					IV.B
Edge/divertor visible/UV/near-IR spectroscopy	✪	✸		❖	✸	✸	❖	✸	✸	✸			V.B&C
Visible/UV filtered detectors & filtered cameras		✸		❖			❖	✸	✸				V.D
Fabry-Perot interferometry and visible spectroscopy										✸			V.E
IR synchrotron radiation imaging												✸	VI

✸ Primary (technique is well suited to measurement)
✪ Backup (technique provides useful data but has some limitations compared to primary)
❖ Supplementary (technique provides data that can be used to check or constrain other measurements but is not a reliable measurement itself)

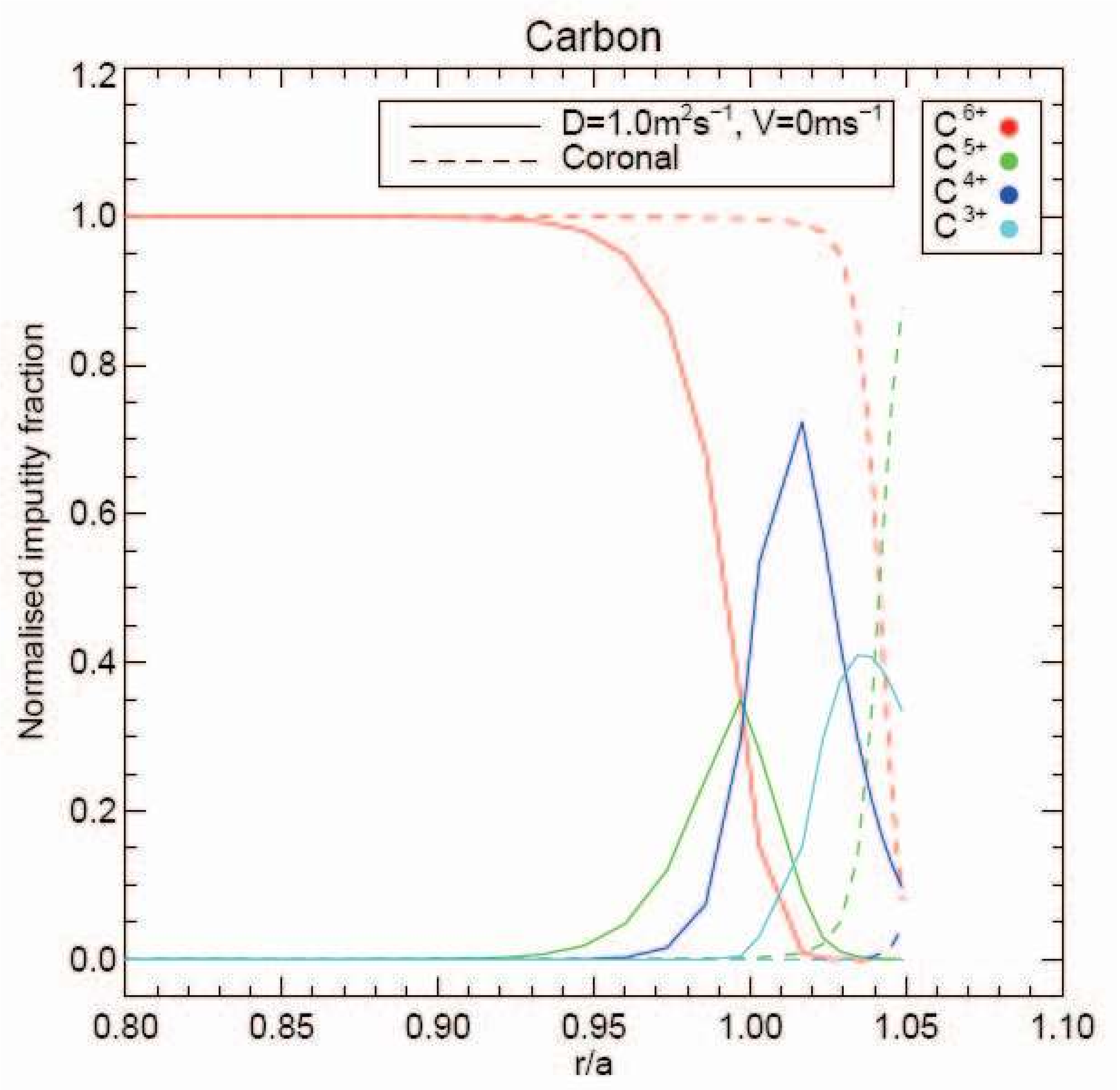

FIG. 1. Carbon ion distribution in JET plasma with T_e and n_e profiles shown in Fig. 4. (Figure courtesy of M. O'Mullane.[16])

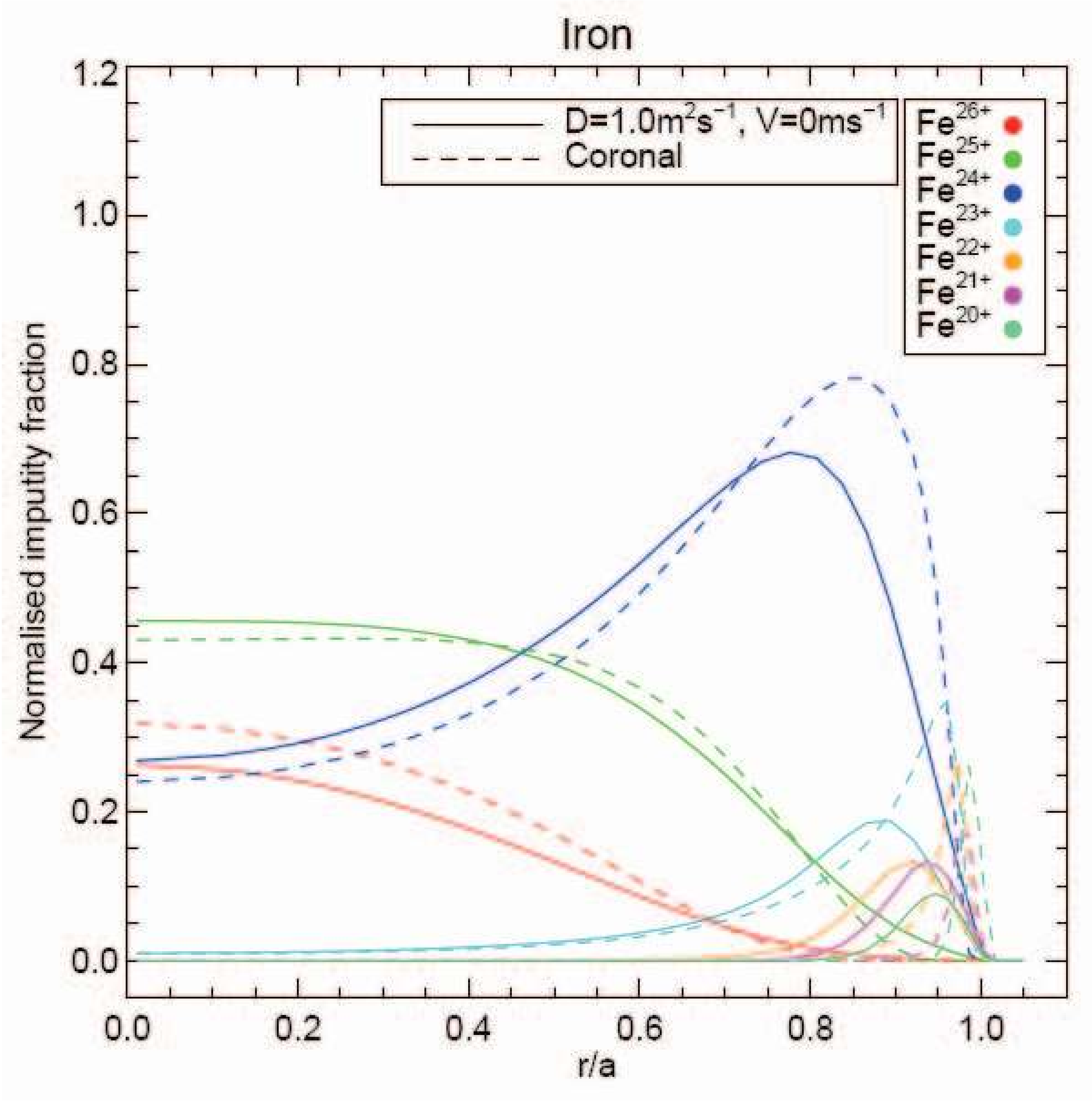

FIG. 2. Iron ion distribution in JET plasma with T_e and n_e profiles shown in Fig. 4. (Figure courtesy of M. O'Mullane.[16])

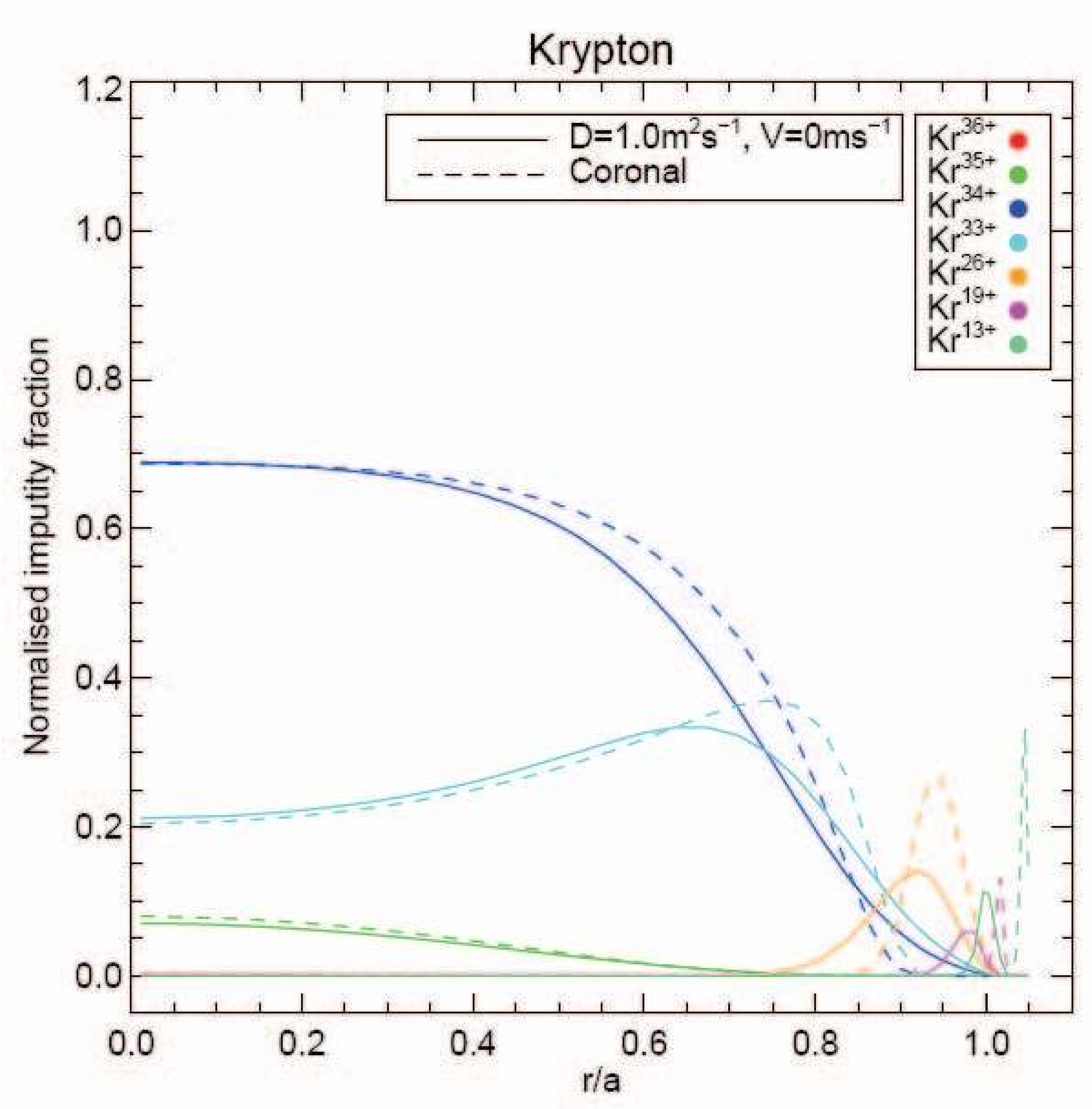

FIG. 3. Krypton ion distribution in JET plasma with T_e and n_e profiles shown in Fig. 4. (Figure courtesy of M. O'Mullane.[16])

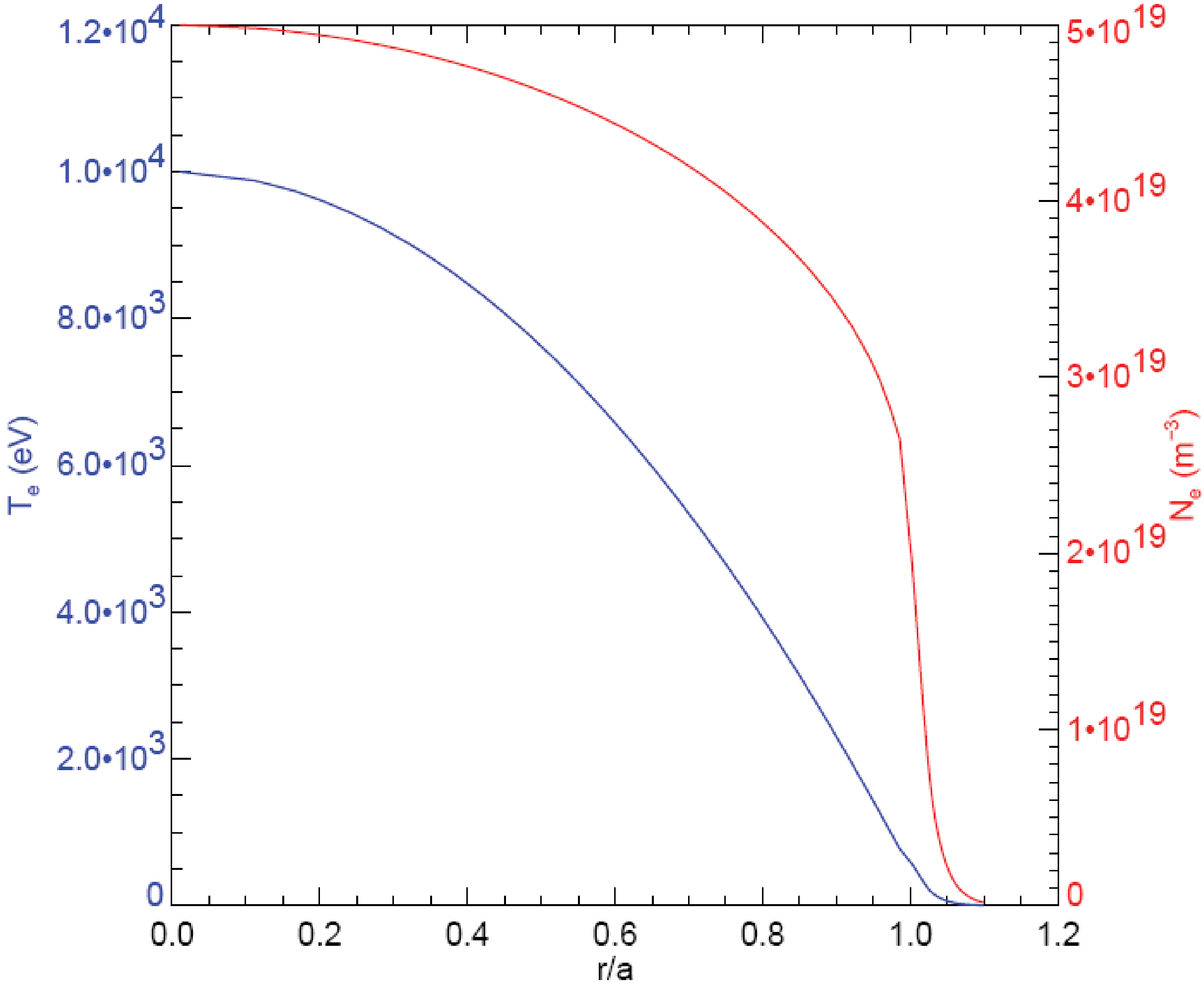

FIG. 4. T_e and n_e profiles assumed in calculations shown in Figs. 1-3. (Figure courtesy of M. O'Mullane.[16])

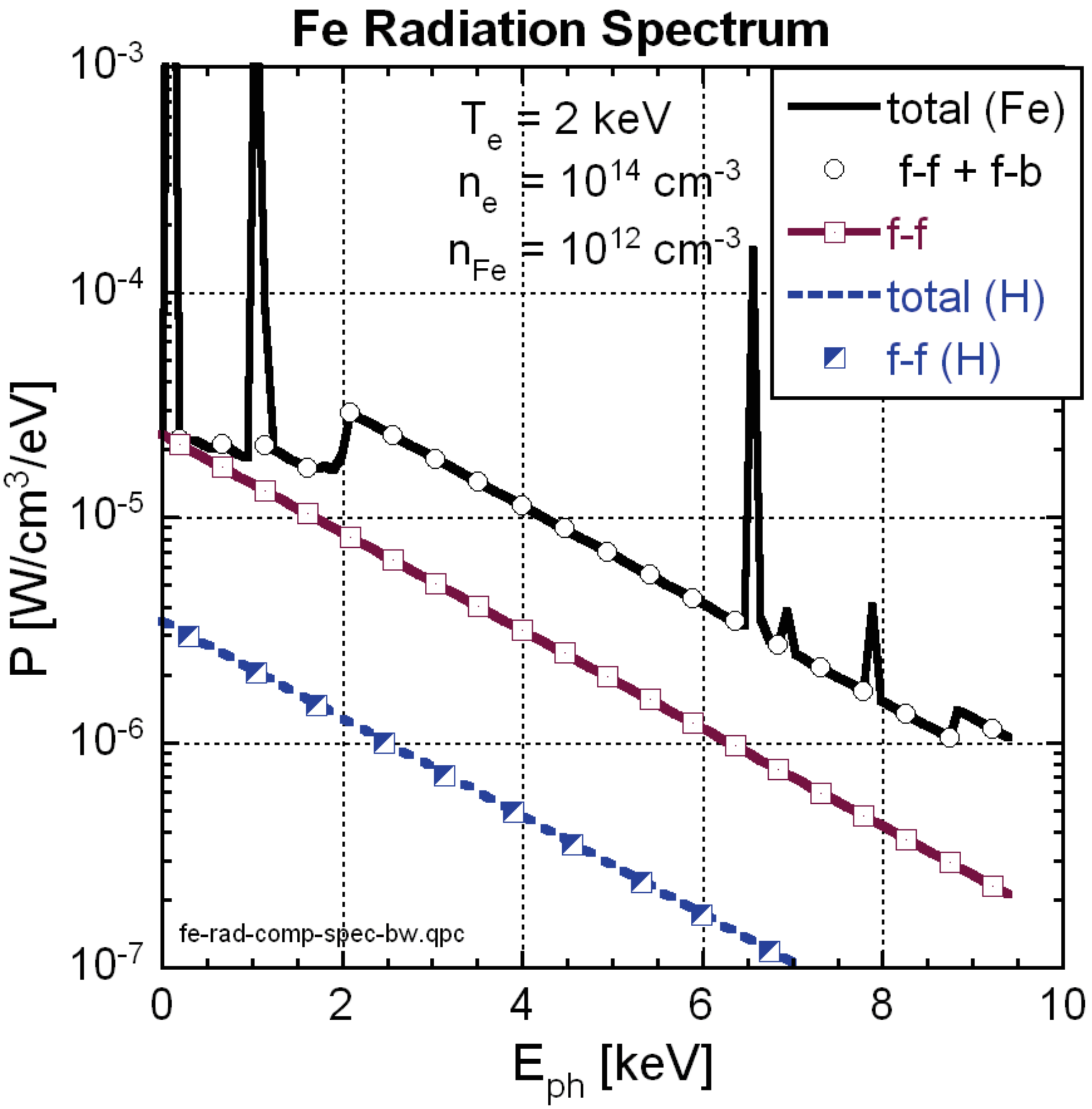

FIG. 5. Calculated soft x-ray spectrum of iron showing the contributions of line, bremsstrahlung, and radiative recombination radiation.[27] The hydrogen continuum is shown for comparison. (Figure courtesy of A. Weller. [27])

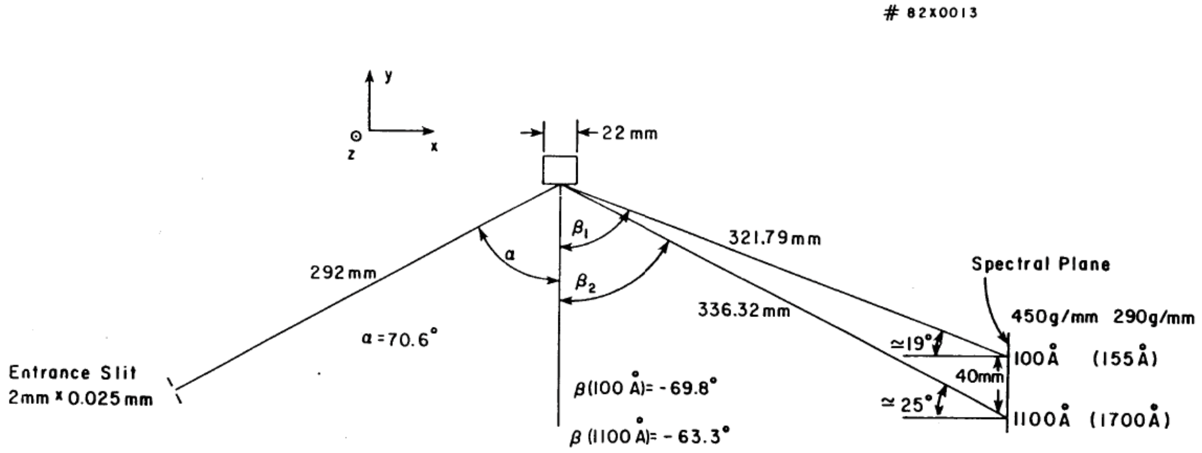

FIG. 6. Optical schematic of the SPRED spectrometer. (From Fonck *et al.*[31] Reused with permission of the Optical Society of America.)

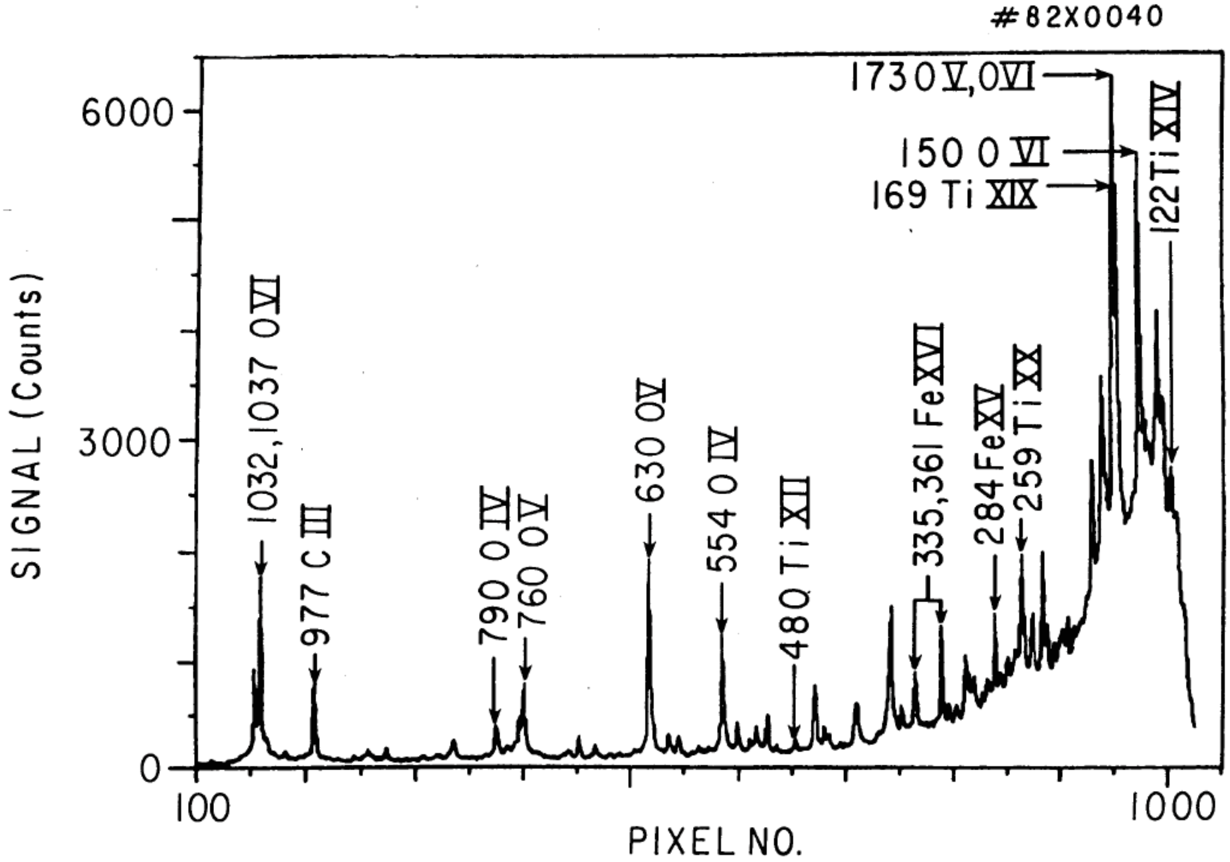

FIG. 7. SPRED spectrum of the 10-110 nm region from the PDX tokamak. (From Fonck *et al.*[31] Reused with permission of the Optical Society of America.)

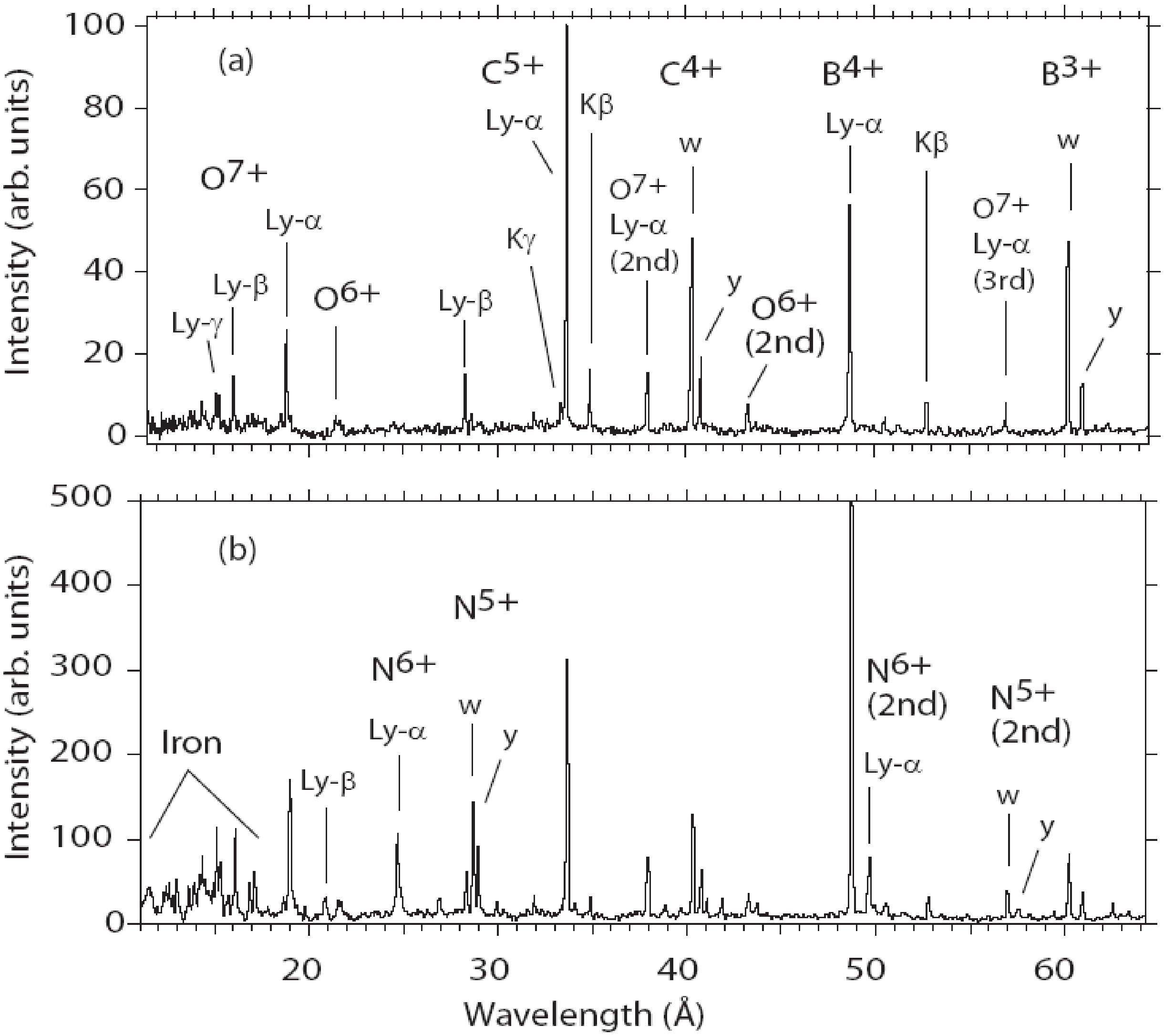

FIG. 8. Spectrum of the 1-6 nm region on NSTX obtained using a high-resolution, flat-field spectrometer. (From Beiersdorfer *et al.*[39] Reused with permission from P. Beiersdorfer, Review of Scientific Instruments, **77**, 10F306 (2006). Copyright 2006, American Institute of Physics.)

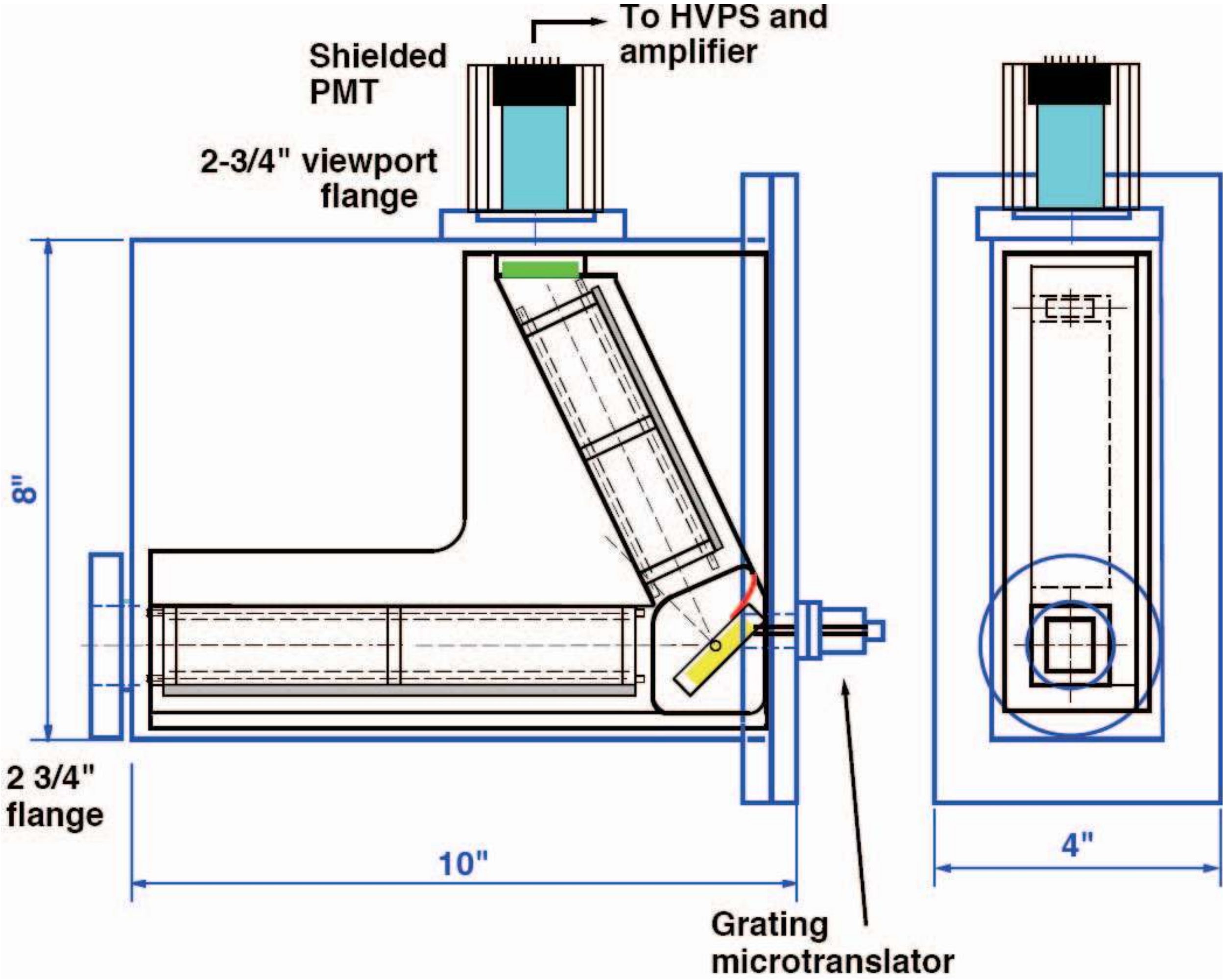

FIG. 9. Layout of plane grating polychromator. (From Soukhanovskii *et al.*[61] Reused with permission from V. A. Soukhanovskii, Review of Scientific Instruments, **72**, 3270 (2001). Copyright 2001, American Institute of Physics.)

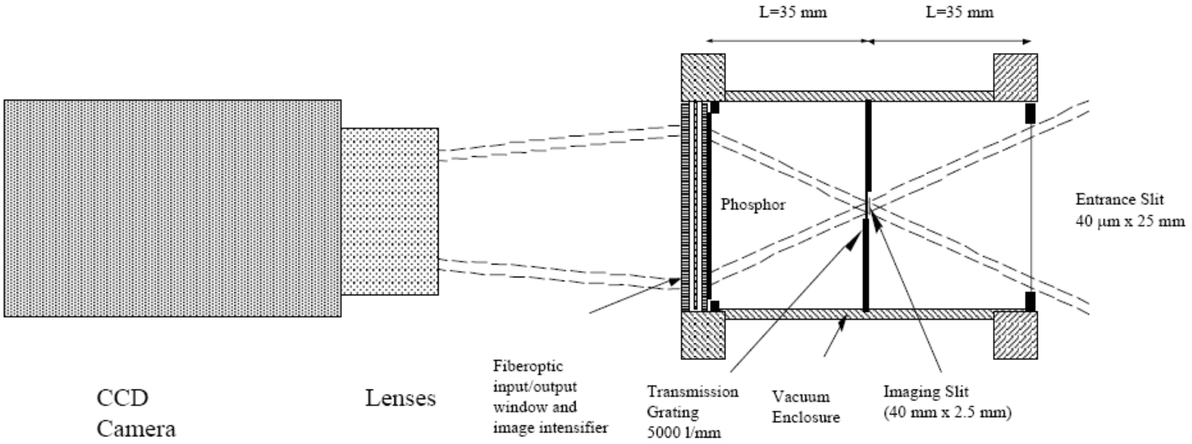

FIG. 10. Layout of EUV transmission grating spectrometer. (From Blagojevic *et al.*[62] Reused with permission from B. Blagojevic, Review of Scientific Instruments, **74**, 1988 (2003). Copyright 2003, American Institute of Physics.)

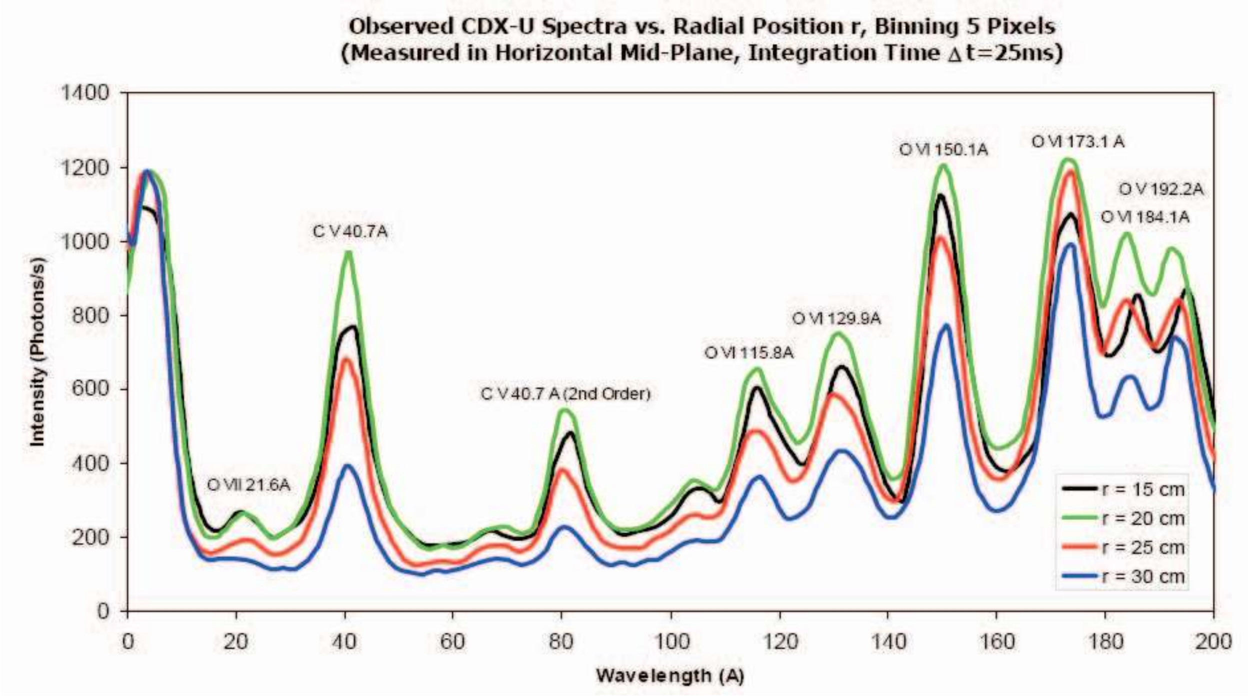

FIG. 11. Spatially-resolved spectrum of 2-20 nm region from CDX-U obtained using transmission grating spectrometer. (From Blagojevic *et al.*[62] Reused with permission from B. Blagojevic, Review of Scientific Instruments, **74**, 1988 (2003). Copyright 2003, American Institute of Physics.)

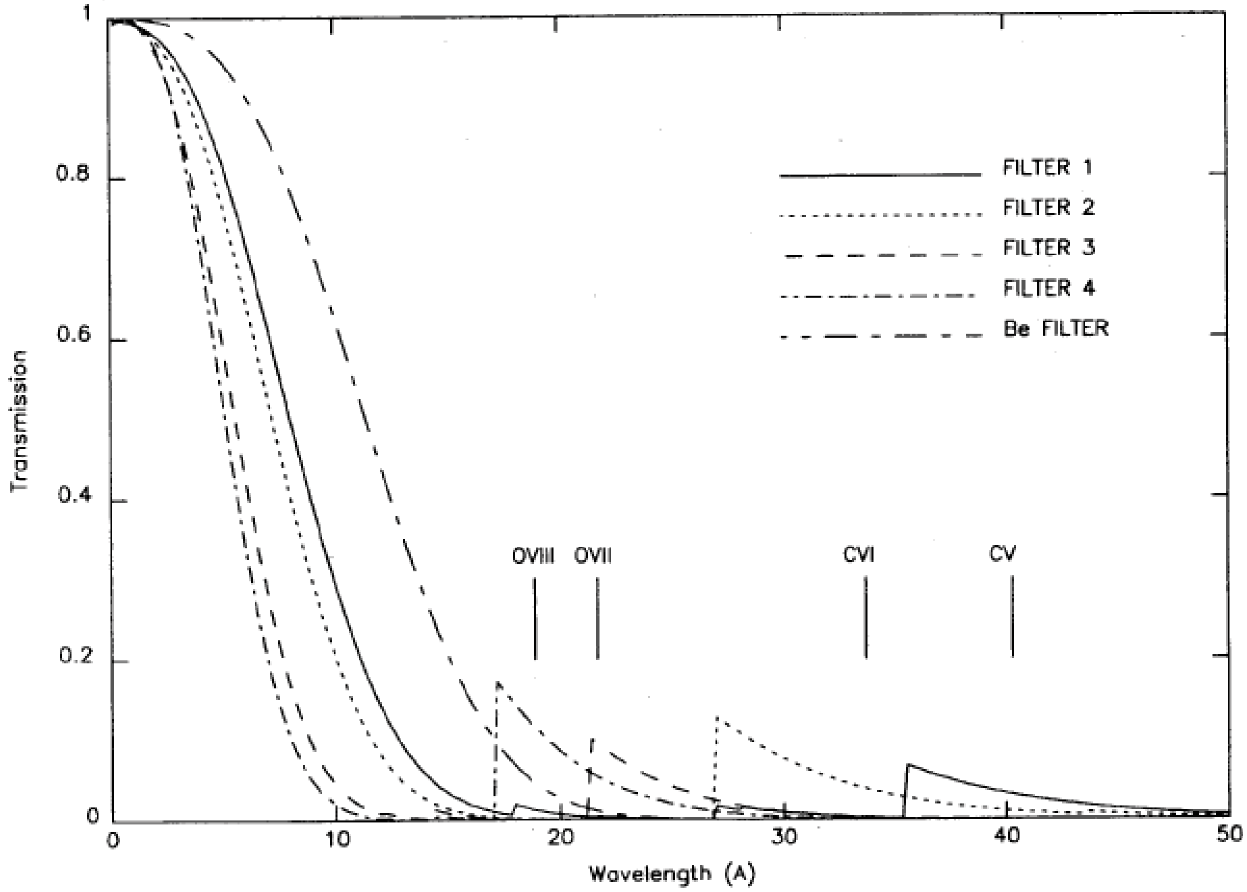

FIG. 12. Transmission curves for four filters used for filtered surface barrier diode measurements on MST. (From S. Hokin *et al.*[64] Reused with permission from S. Hokin, Review of Scientific Instruments, **63**, 5038 (1992). Copyright 1992, American Institute of Physics.)

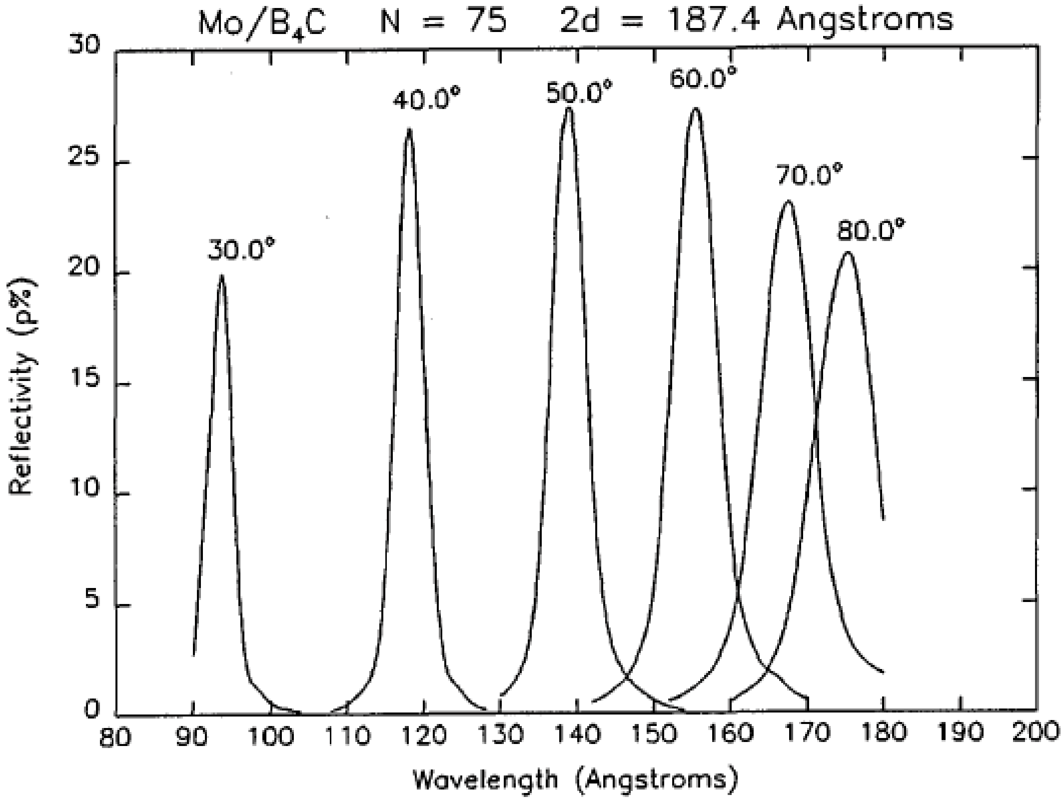

FIG. 13. Measured reflectivity and line shapes in the 9-18 nm region for a planar Mo/B_4C multilayer mirror with 75 layers and 2d=18.74 nm at various Bragg angles. (From A. P. Zwicker *et al.*[71] Reused with permission of the Optical Society of America.)

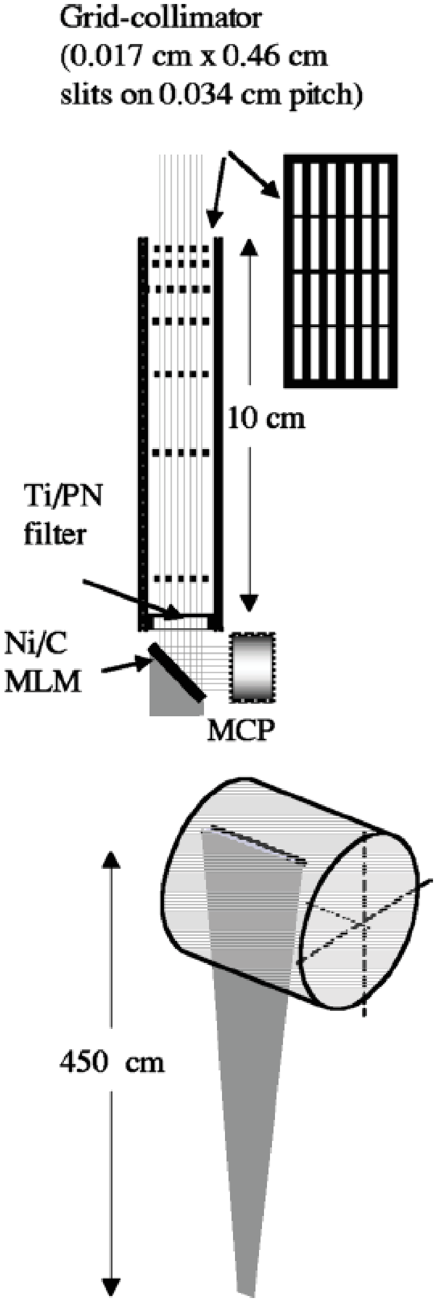

FIG. 14. Layout of multilayer mirror monochromator. (From D. Stutman *et al.*[74] Reused with permission from D. Stutman, Review of Scientific Instruments, **76**, 013508 (2005). Copyright 2005, American Institute of Physics.)

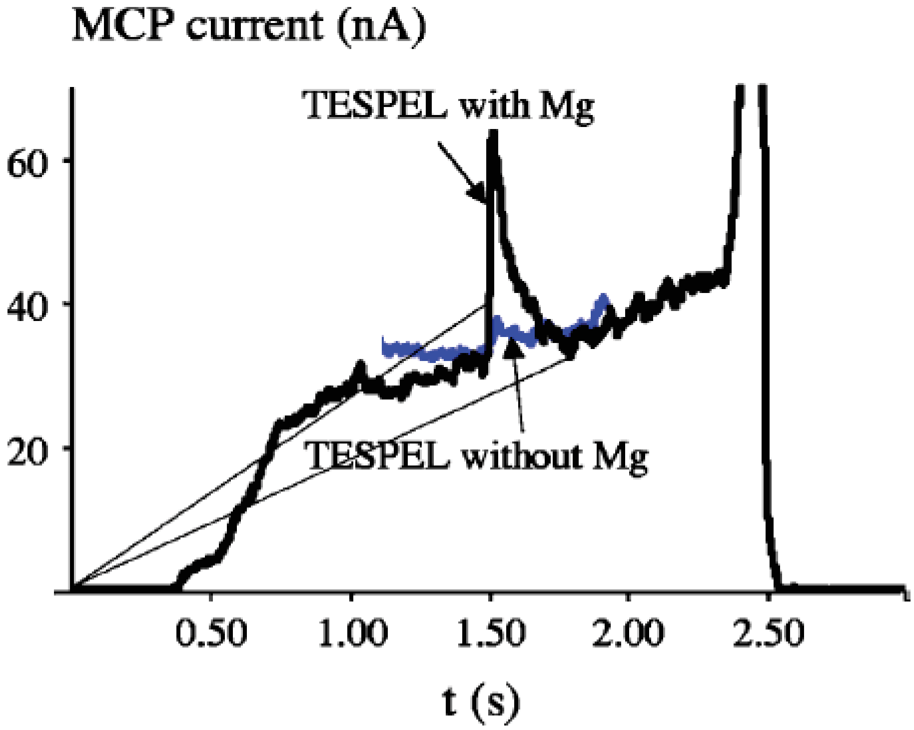

FIG. 15. Time evolution of Mg H_α 4.55 nm line from an impurity tracer pellet (TESPEL) containing Mg injected into LHD. The time evolution for a pellet without Mg is also shown. (From D. Stutman *et al.*[74] Reused with permission from D. Stutman, Review of Scientific Instruments, **76**, 013508 (2005). Copyright 2005, American Institute of Physics.)

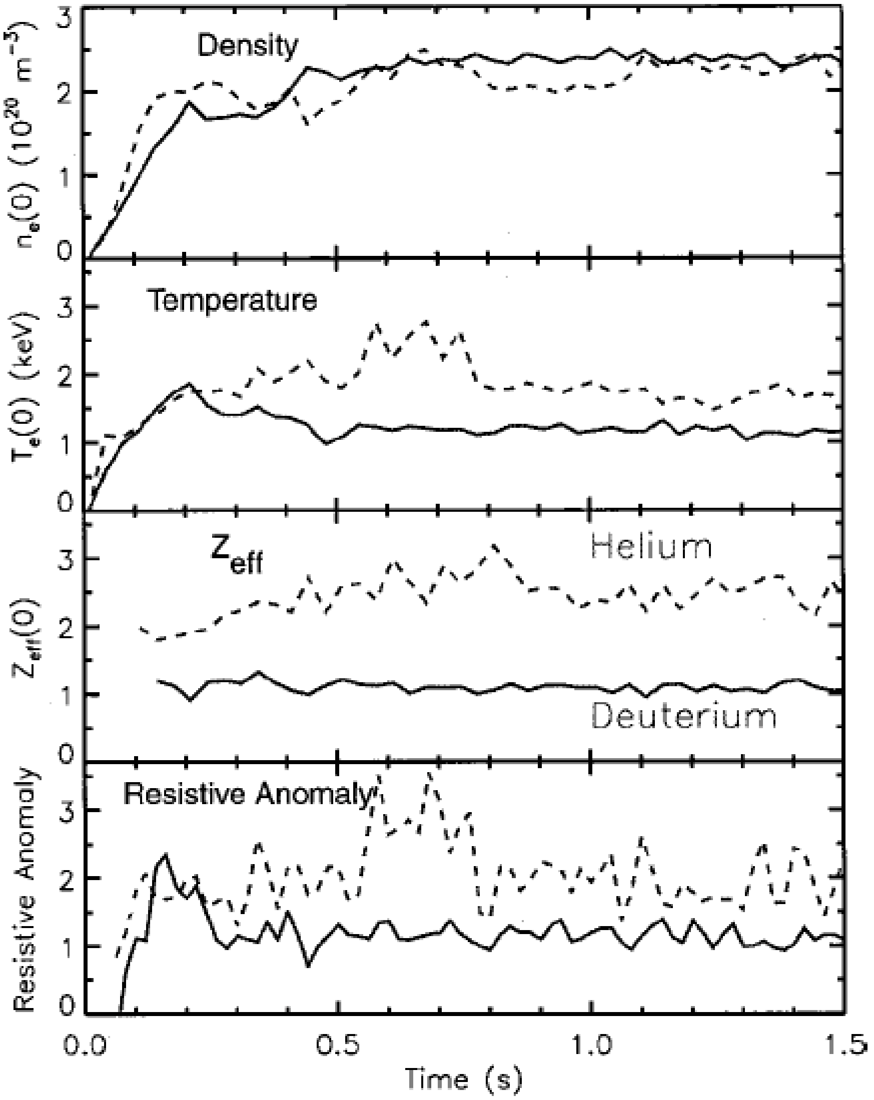

FIG. 16. Time evolution of $n_e(0)$, $T_e(0)$, and $Z_{eff}(0)$, in deuterium and helium Alcator C-Mod discharges. (From E. Marmar *et al.*[80] Reused with permission from E. Marmar, Review of Scientific Instruments, **72**, 940 (2001). Copyright 2001, American Institute of Physics.)

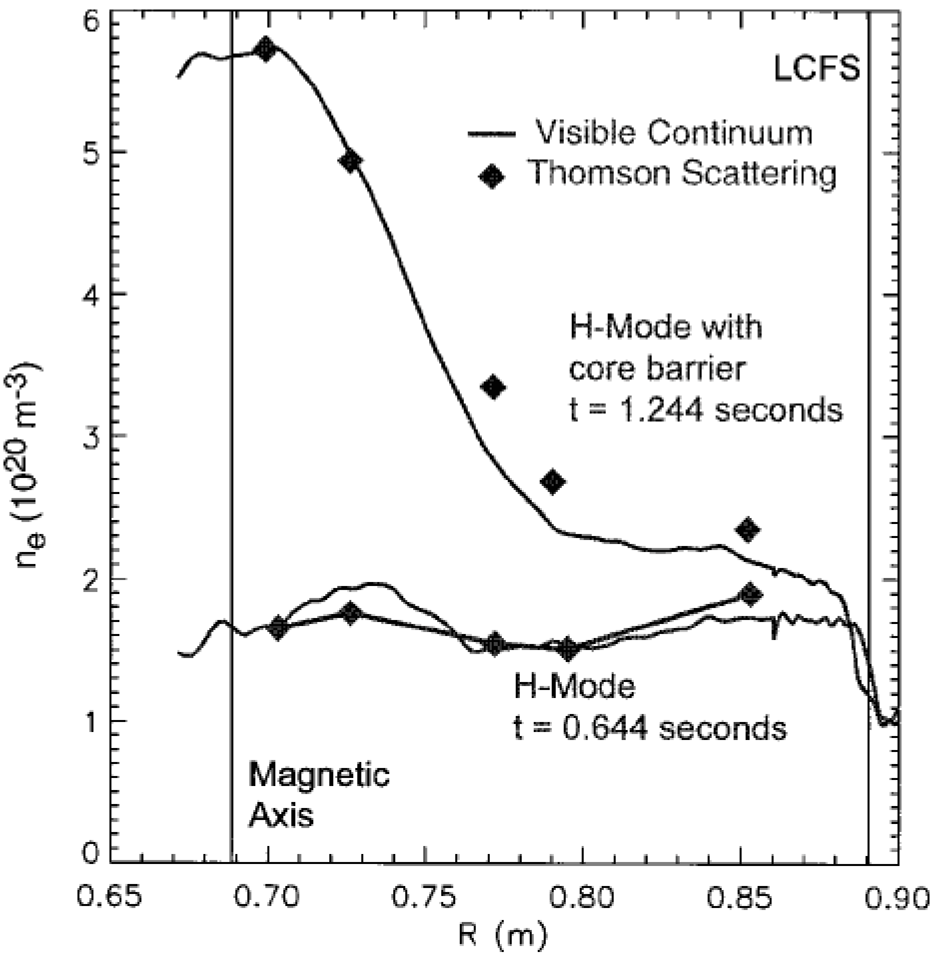

FIG. 17. n_e profiles deduced from visible bremsstrahlung measurements (lines) at two times in an Alcator C-Mod discharge. Thomson scattering measurements (points) are shown for comparison. (From E. Marmar *et al.*[80] Reused with permission from E. Marmar, Review of Scientific Instruments, **72**, 940 (2001). Copyright 2001, American Institute of Physics.)

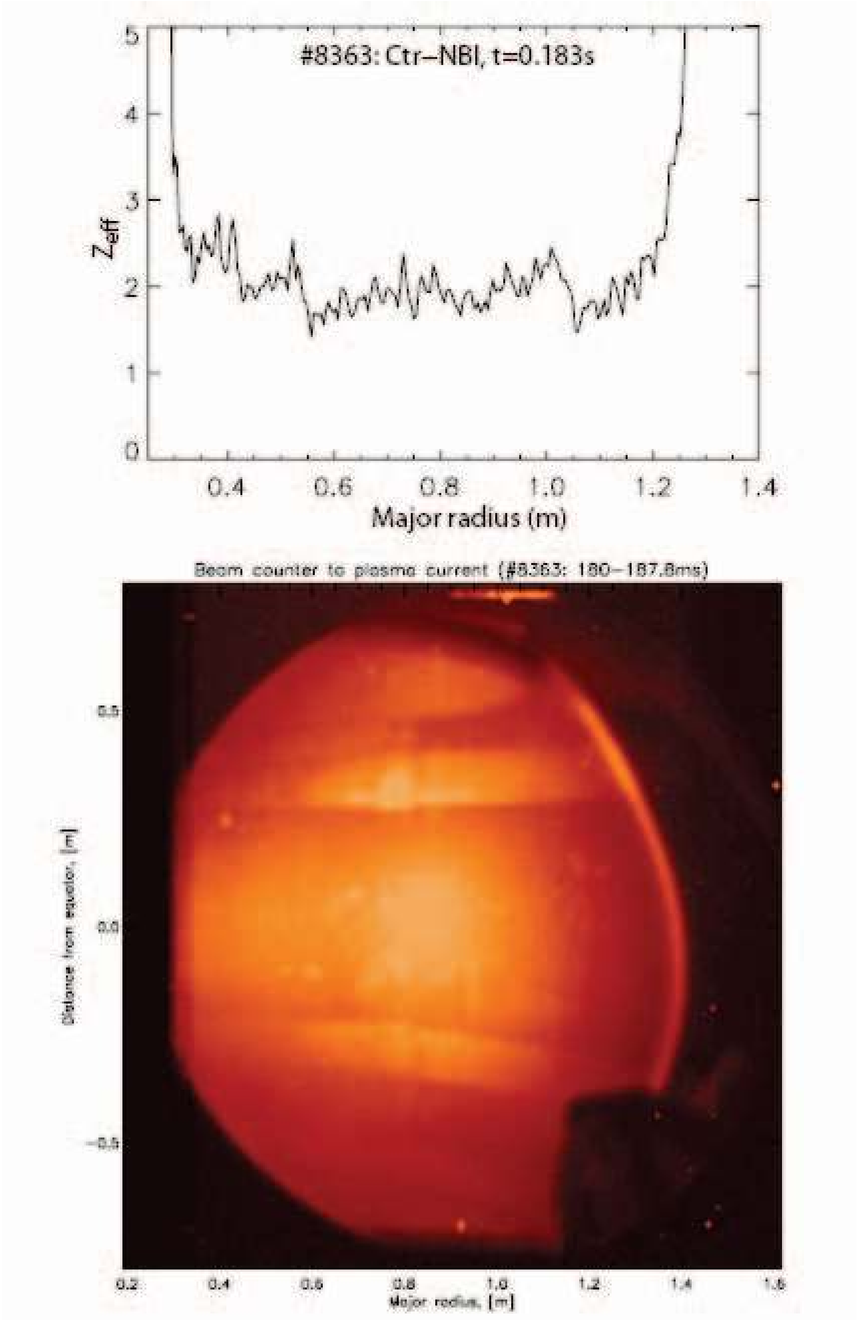

FIG. 18. Image of MAST plasma in visible bremsstrahlung radiation (bottom); Z_{eff} profile in midplane obtained from Abel inversion of midplane radiance profile and Thomson scattering measurements of n_e and T_e (top). (From P. Carolan *et al.*[81] Reused with permission from P. Carolan, Review of Scientific Instruments, **75**, 4069 (2004). Copyright 2004, American Institute of Physics.)

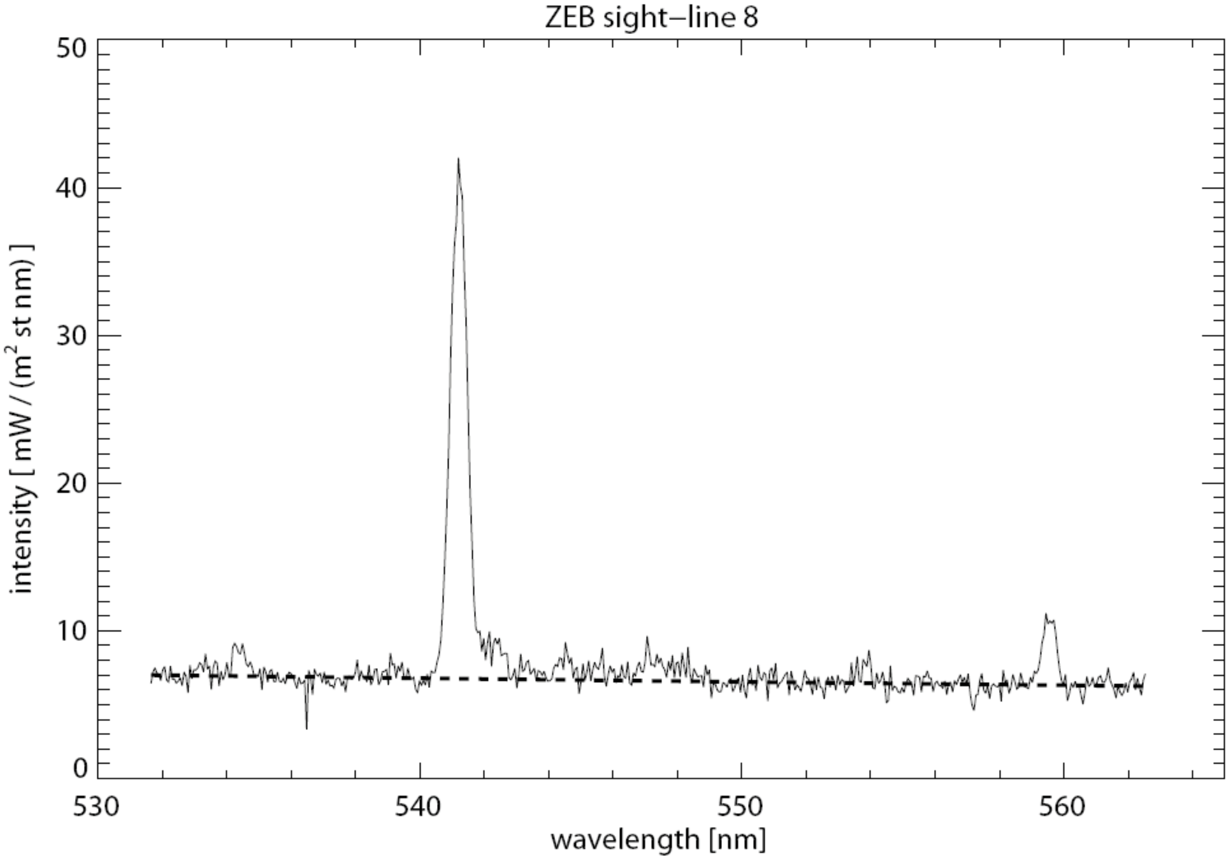

FIG. 19. Spectrum from edge of ASDEX Upgrade plasma showing lines and bremsstrahlung background. The fit to the bremsstrahlung signal assuming a λ^{-2} dependence is shown (dashed line). (From H. Meister *et al.*[82] Reused with permission from H. Meister, Review of Scientific Instruments, **75**, 4097 (2004). Copyright 2004, American Institute of Physics.)

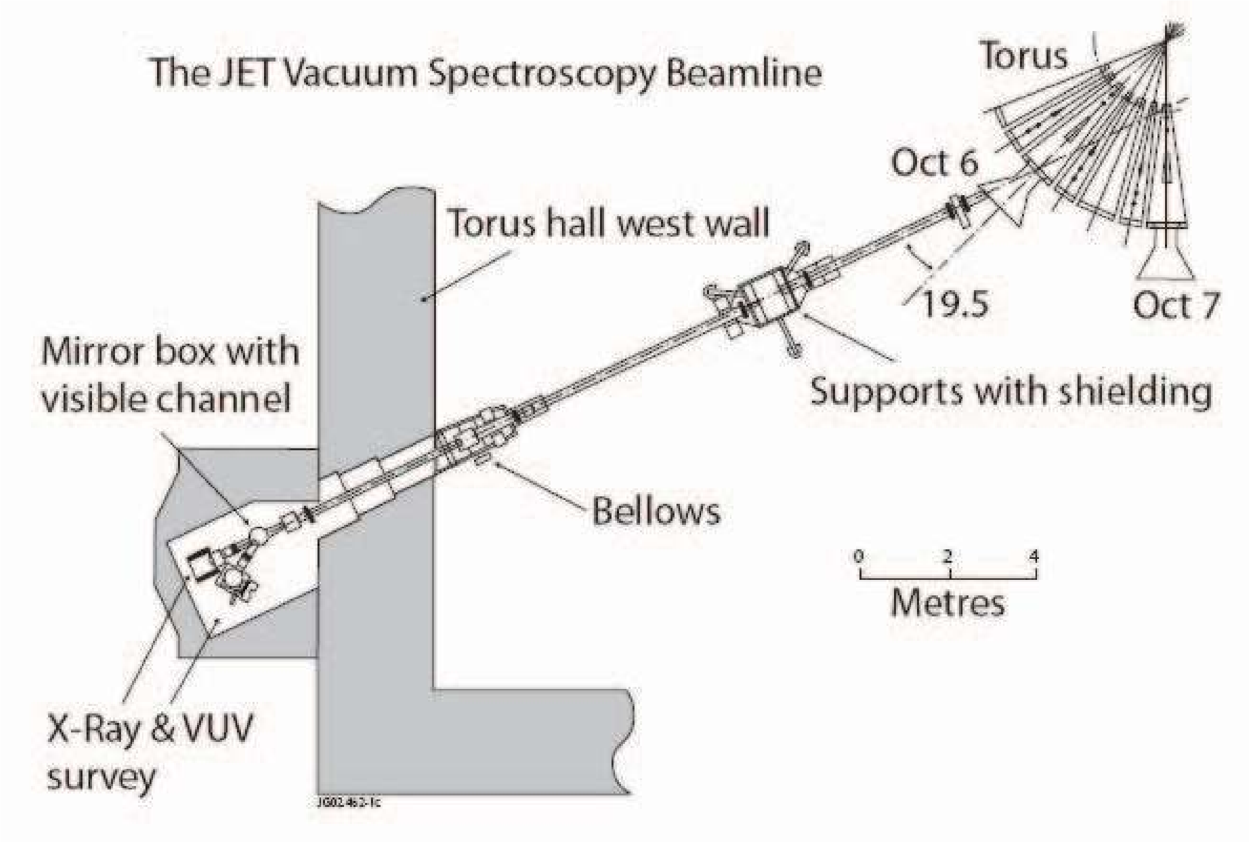

FIG. 20. Installation of SPRED and x-ray crystal survey spectrometers in a remote, shielded bunker on JET. The instruments view the plasma through a long beamline and a grazing incidence mirror is used to deflect the light into the SPRED spectrometer. (From R. Barnsley *et al.* [91] Reused with permission from R. Barnsley, Review of Scientific Instruments, **74**, 1969 (2003). Copyright 2003, American Institute of Physics and EFDA-JET.)

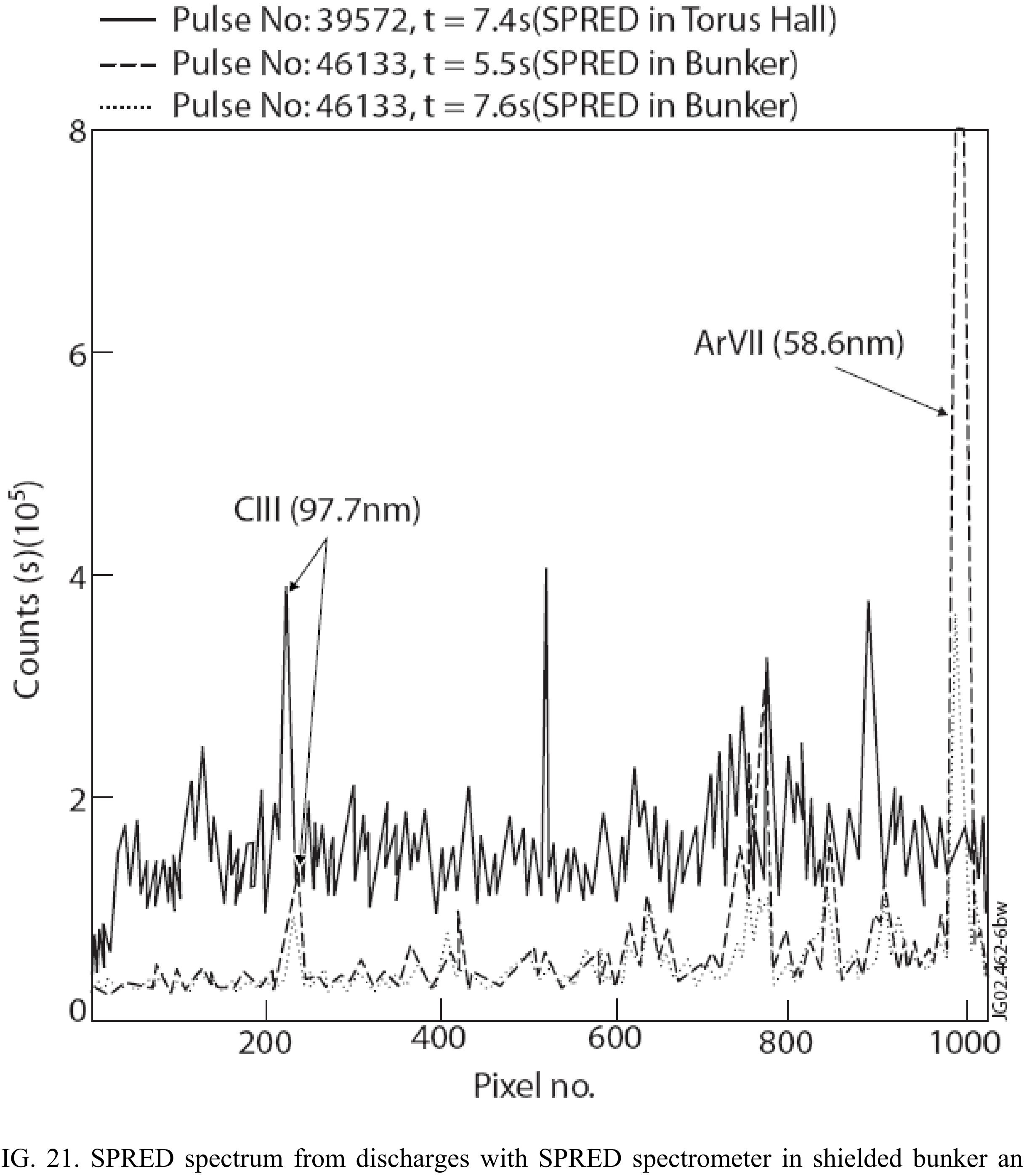

FIG. 21. SPRED spectrum from discharges with SPRED spectrometer in shielded bunker and near JET tokamak with no shielding. There is a strong reduction in neutron noise due to shielding. (From R. Barnsley *et al.* [91] Reused with permission from R. Barnsley, Review of Scientific Instruments, **74**, 1969 (2003). Copyright 2003, American Institute of Physics and EFDA-JET.)

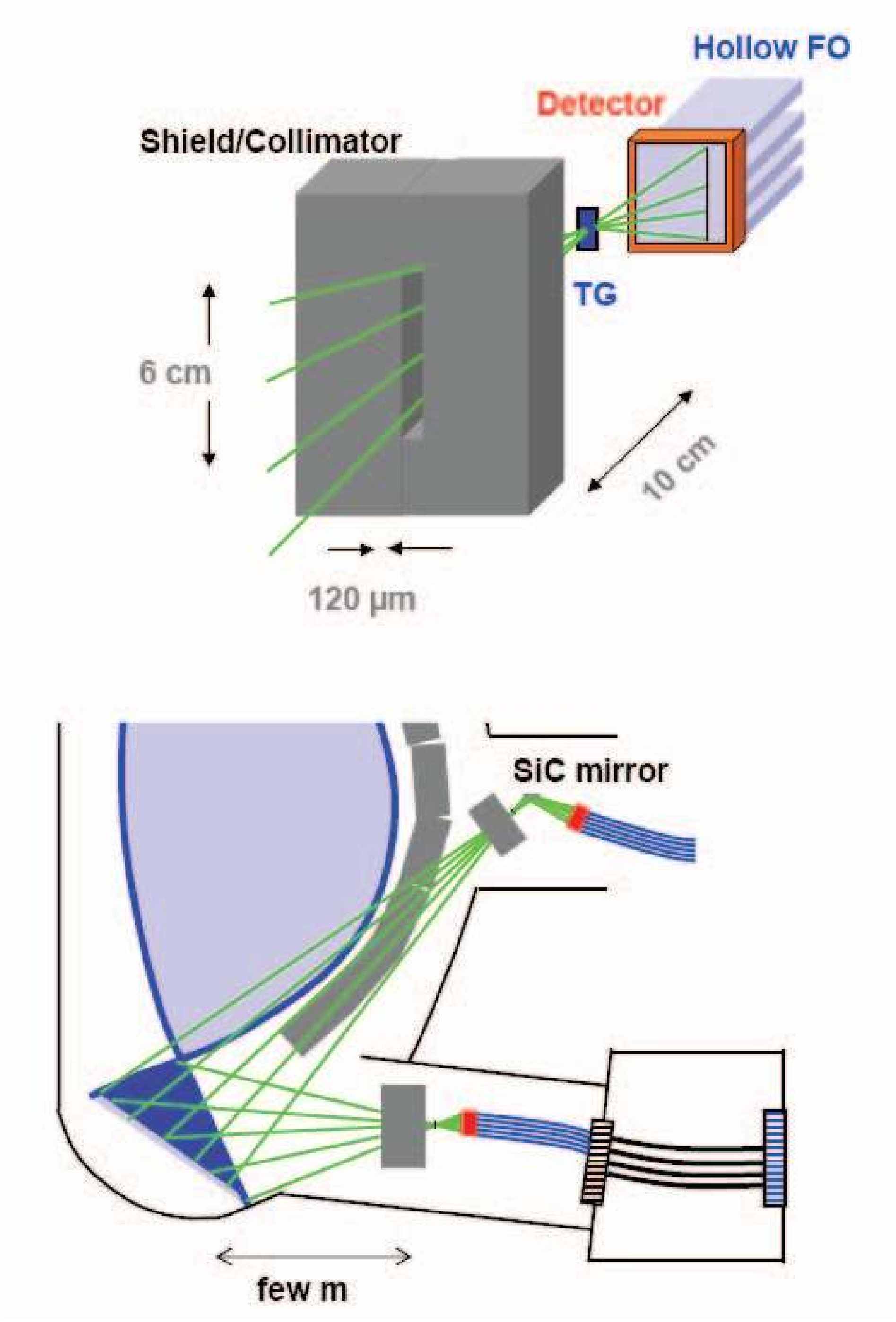

FIG. 22. Conceptual layout of a transmission grating spectrometer viewing the ITER divertor region. (From Stutman *et al.*[96] Reused with permission from D. Stutman, Review of Scientific Instruments, **76**, 023505-1 (2005). Copyright 2005, American Institute of Physics.)

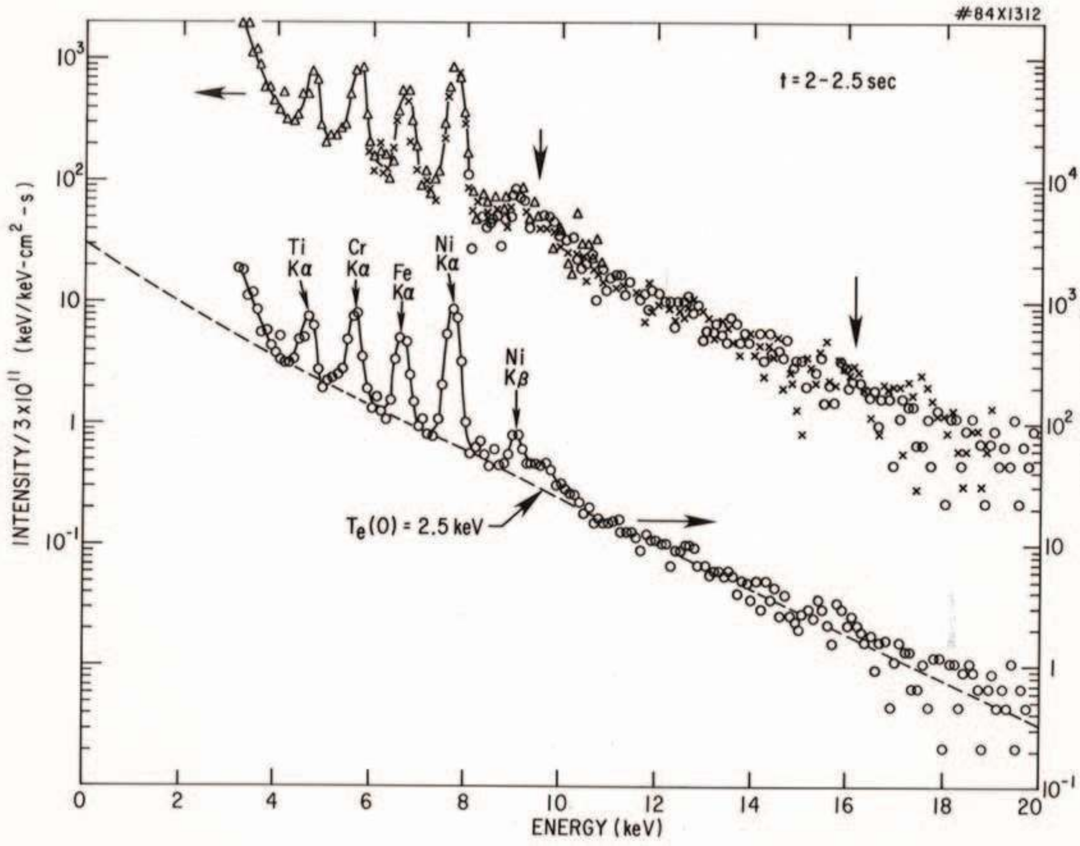

FIG. 23. Pulse height analyzer soft X-ray spectra from a TFTR discharge showing the continuum and $K_{\alpha,\beta}$ lines of metallic impurities. The symbols in the upper trace represent data taken with Be foils of different thicknesses. (From Hill *et al.*[117] Reused with permission from K. W. Hill, Review of Scientific Instruments, **56**, 840 (1985). Copyright 1985, American Institute of Physics.)

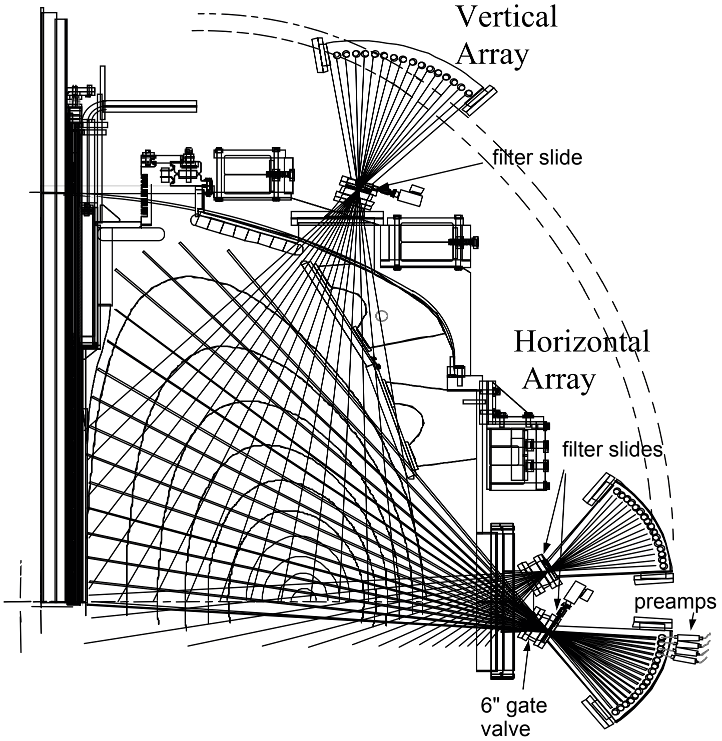

FIG. 24. Layout of two poloidally-viewing X-ray imaging arrays on NSTX. (From Stutman *et al.*[134] Reused with permission from D. Stutman, Review of Scientific Instruments, **70**, 572 (1999). Copyright 1999, American Institute of Physics.)

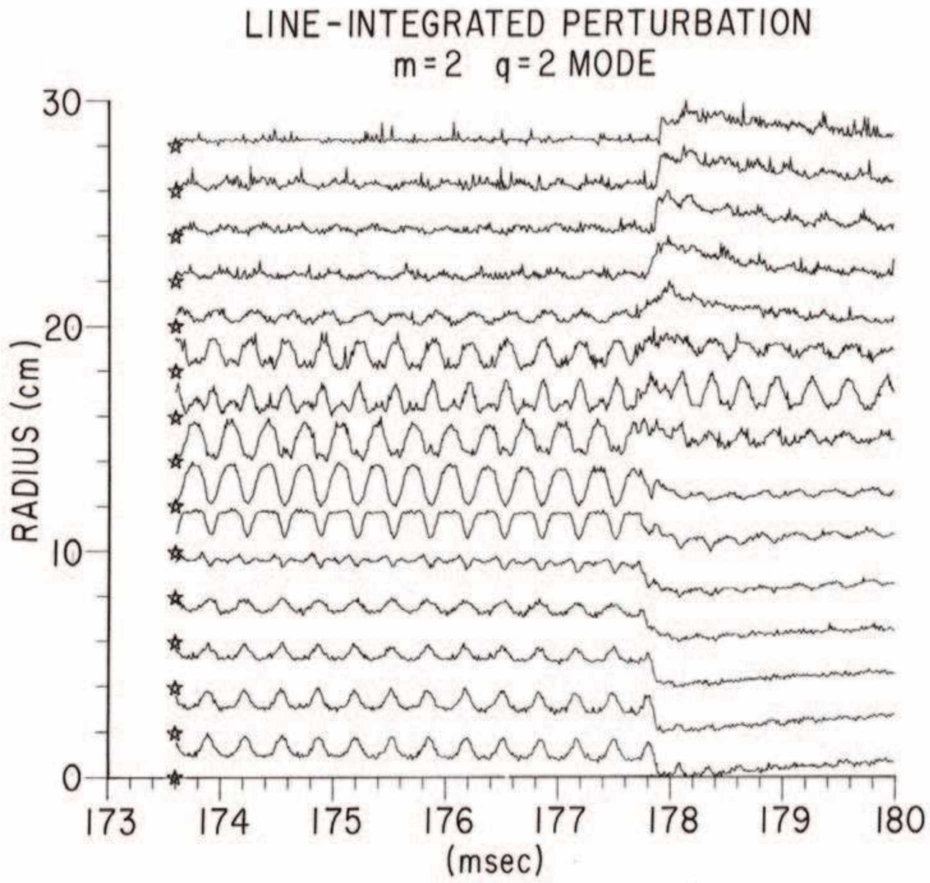

FIG. 25. X-Ray imaging array signals from different sightlines as a function of time showing an m=2 MHD mode.

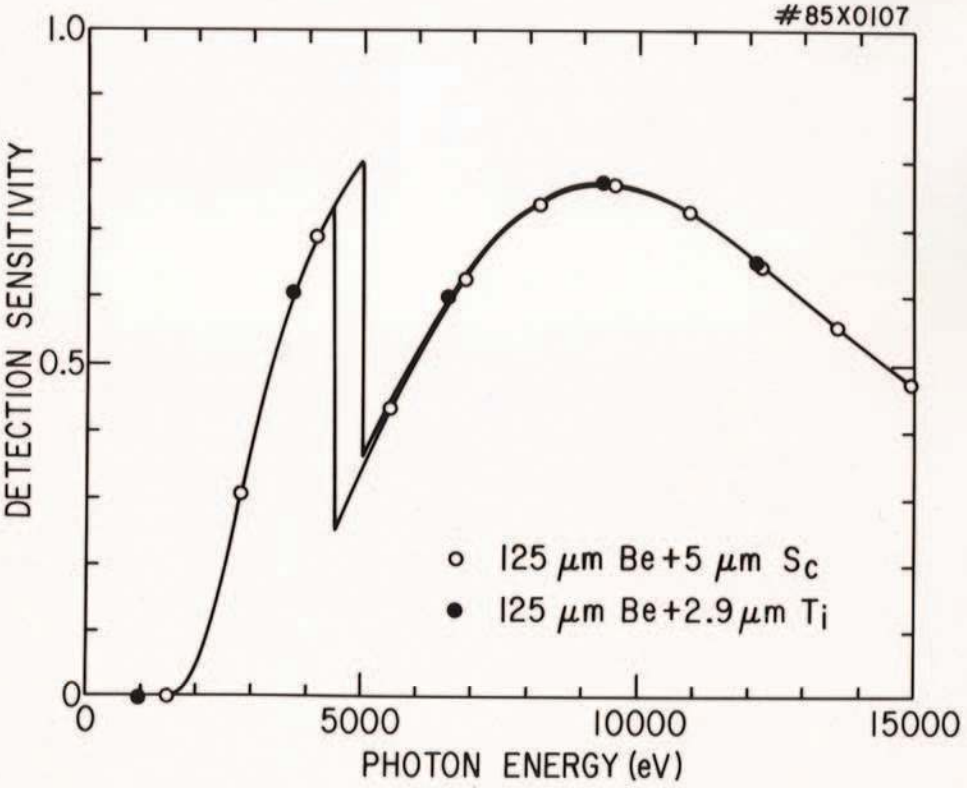

FIG. 26. Soft X-ray detector sensitivity for a SXR array filtered by two different types of foils. The difference of the signals from two detectors, each equipped with one of these foils, would measure radiation in the 4.5-5.0 keV energy range.

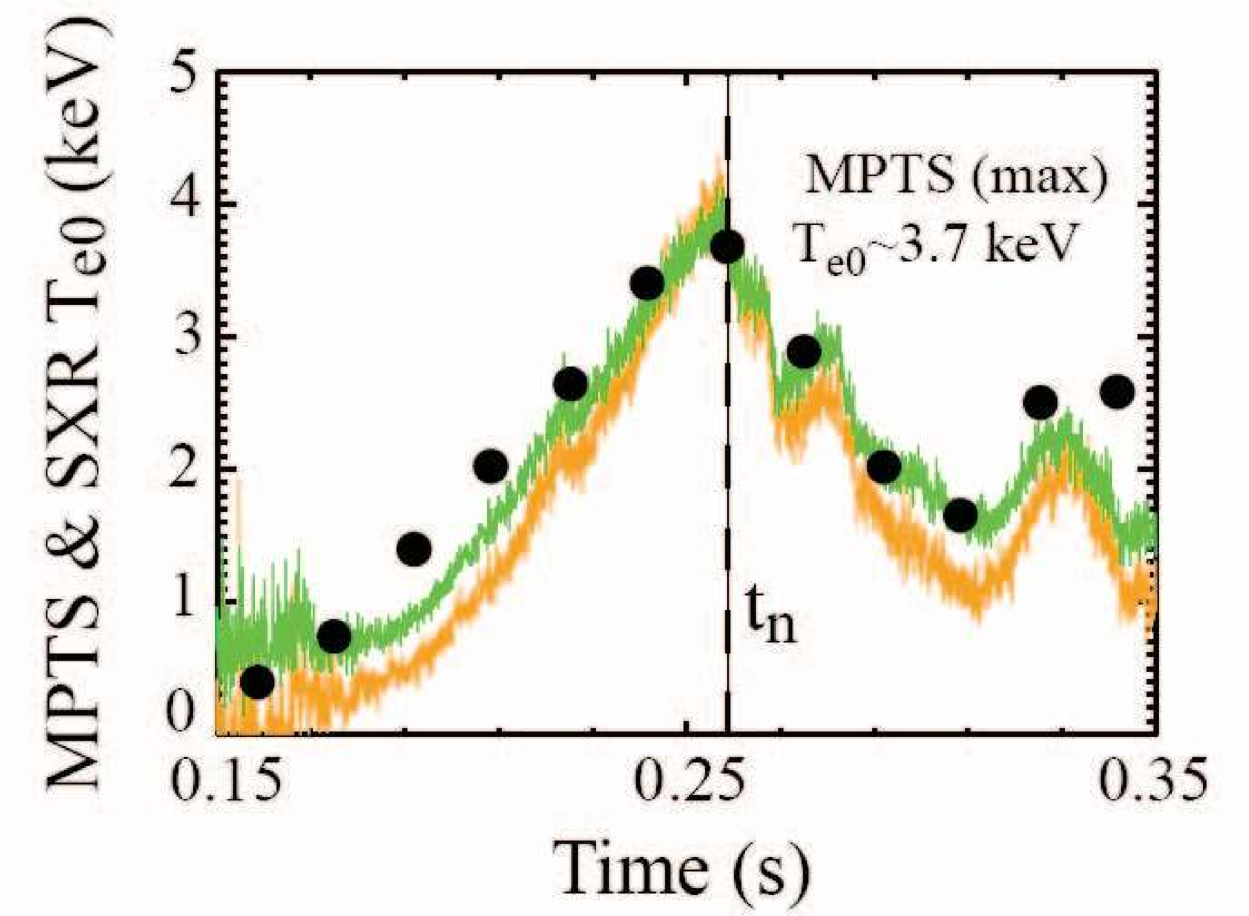

FIG. 27. Core T_e time evolution from an NSTX discharge measured by an optical soft X-ray array (solid line) and Thomson scattering (points).The green trace indicates the T_e deduced from the ratio of signals from detectors with 100 μm and 10 μm Be foils and the orange trace indicates the T_e deduced from the ratio of signals from detectors with 300 μm and 10 μm Be foils. (Figure courtesy of L. Delgado-Aparicio.[167])

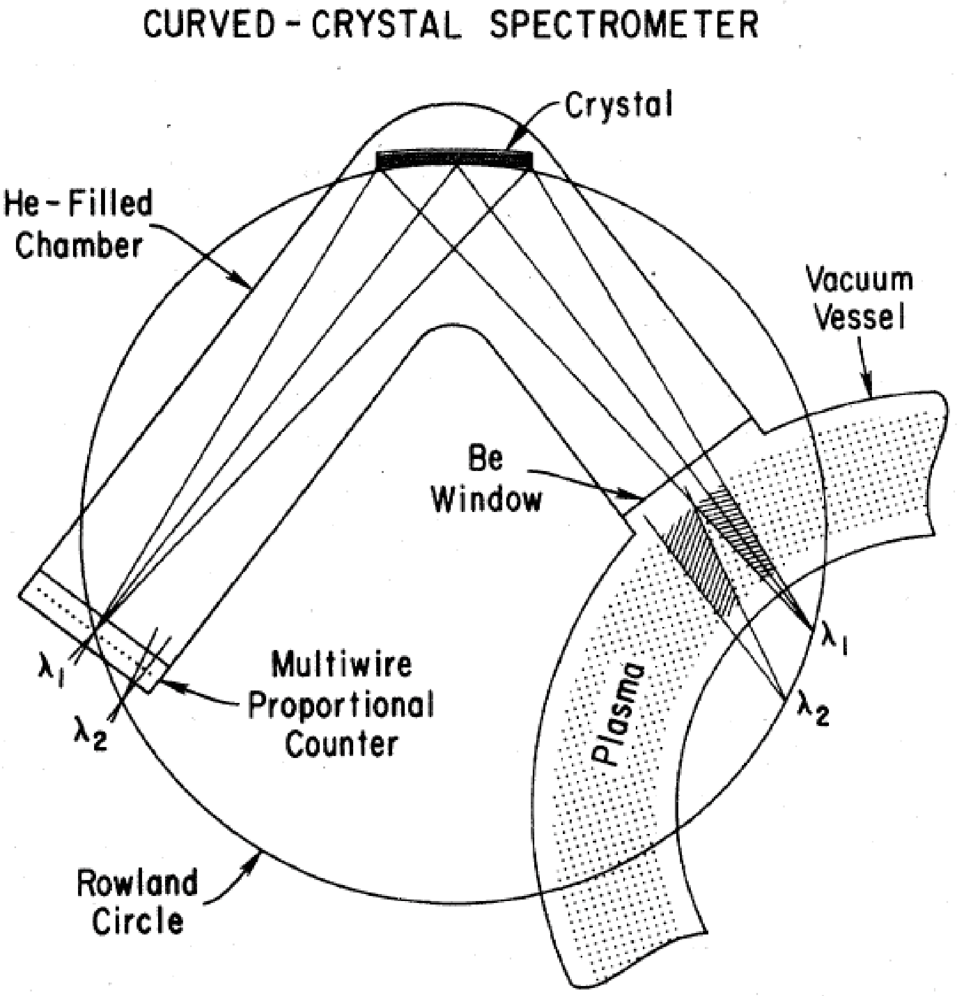

FIG. 28. Schematic of curved crystal spectrometer used on PLT. (From Hill *et al.*[199] Reprinted with permission from K. W. Hill *et al.*, Phys. Rev. A **19**, 1770 (1979). Copyright 1979 by the American Physical Society.)

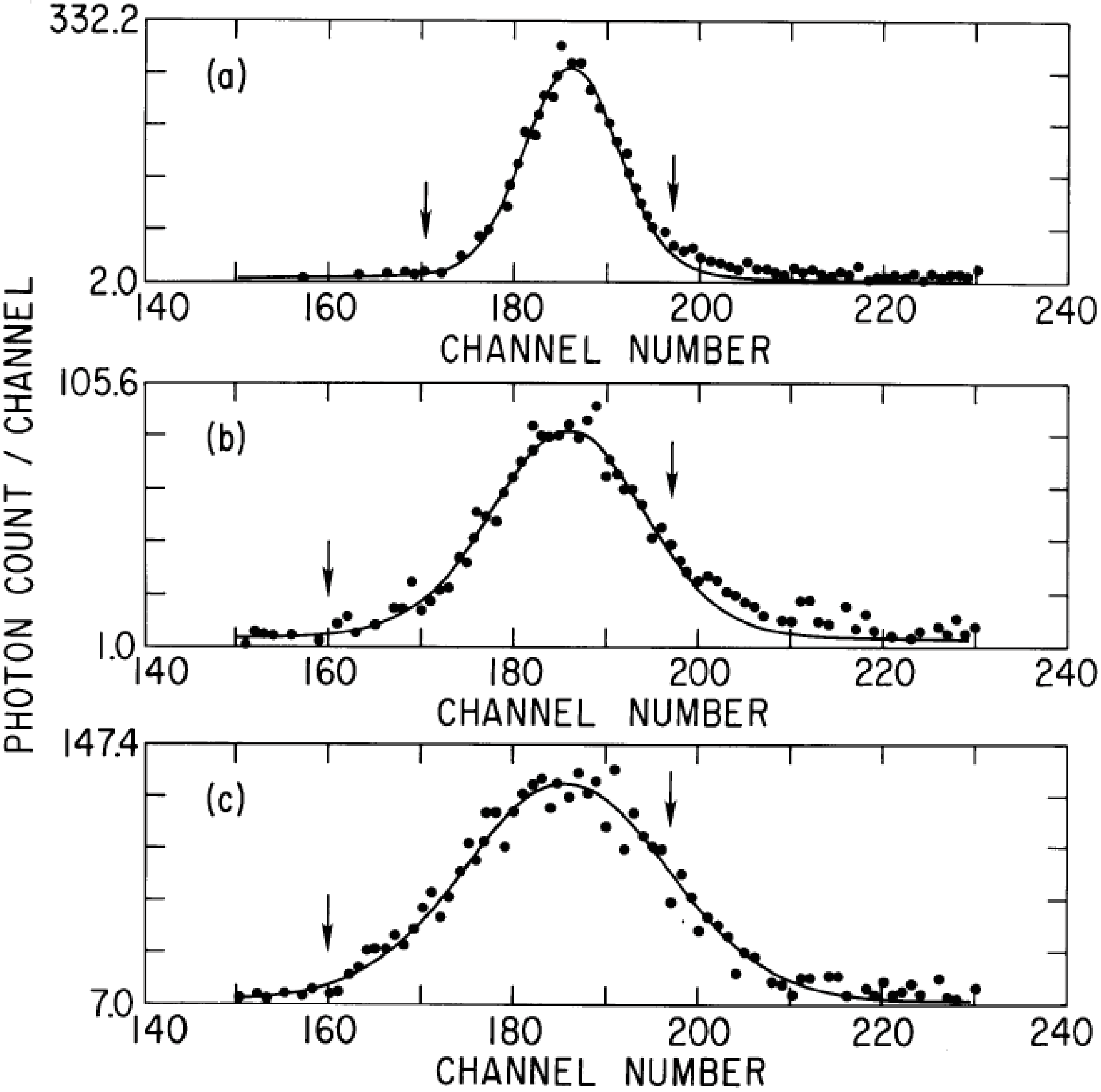

FIG. 29. Line profiles of the Fe^{24+} resonance line (*w*) measured before (a) and during (b, c) neutral beam injection on PLT. The increased Doppler broadening due to the increase in ion temperature during neutral beam injection is apparent. (From Bitter *et al.*[108] Reprinted with permission from M. Bitter *et al.*, Phys. Rev. Lett. **42**, 304 (1979). Copyright 1979 by the American Physical Society.)

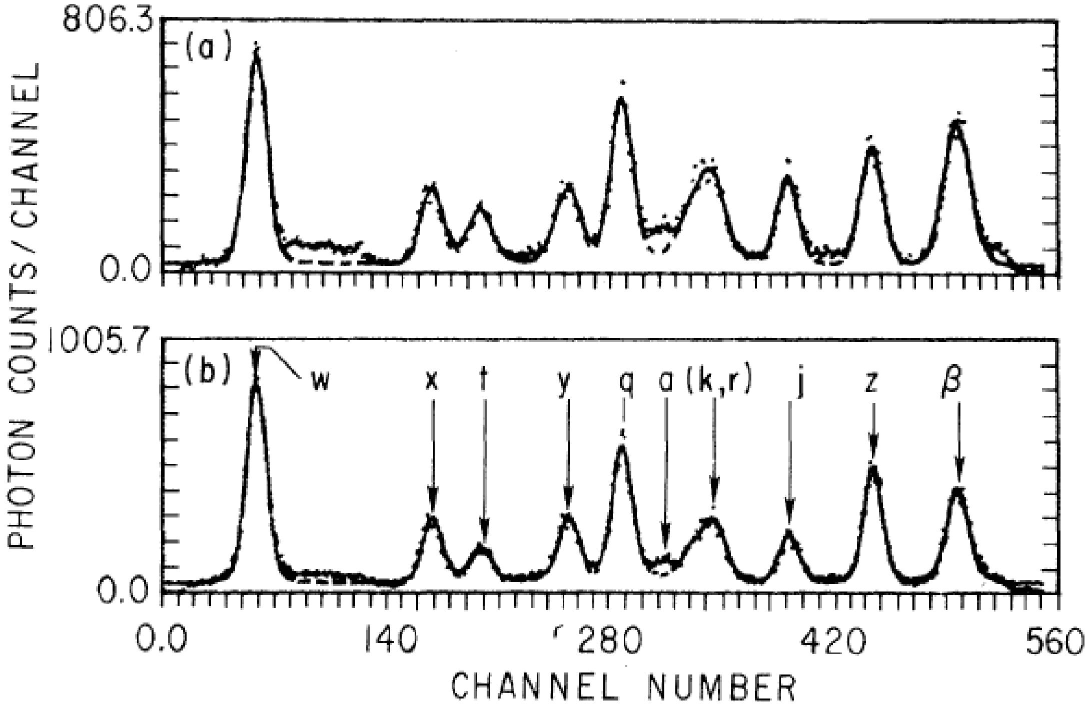

FIG. 30. Dielectronic satellite spectra of Fe^{24+} from PLT plasmas with electron temperatures of 1.65 keV (a) and 2.30 keV (b). The points represent the measurements and the solid curves are the theoretical spectra. The lines are labeled according to the nomenclature of Gabriel. (From Bitter *et al.*[207] Reprinted with permission from M. Bitter *et al.*, Phys. Rev. Lett. **43**, 129 (1979). Copyright 1979 by the American Physical Society.)

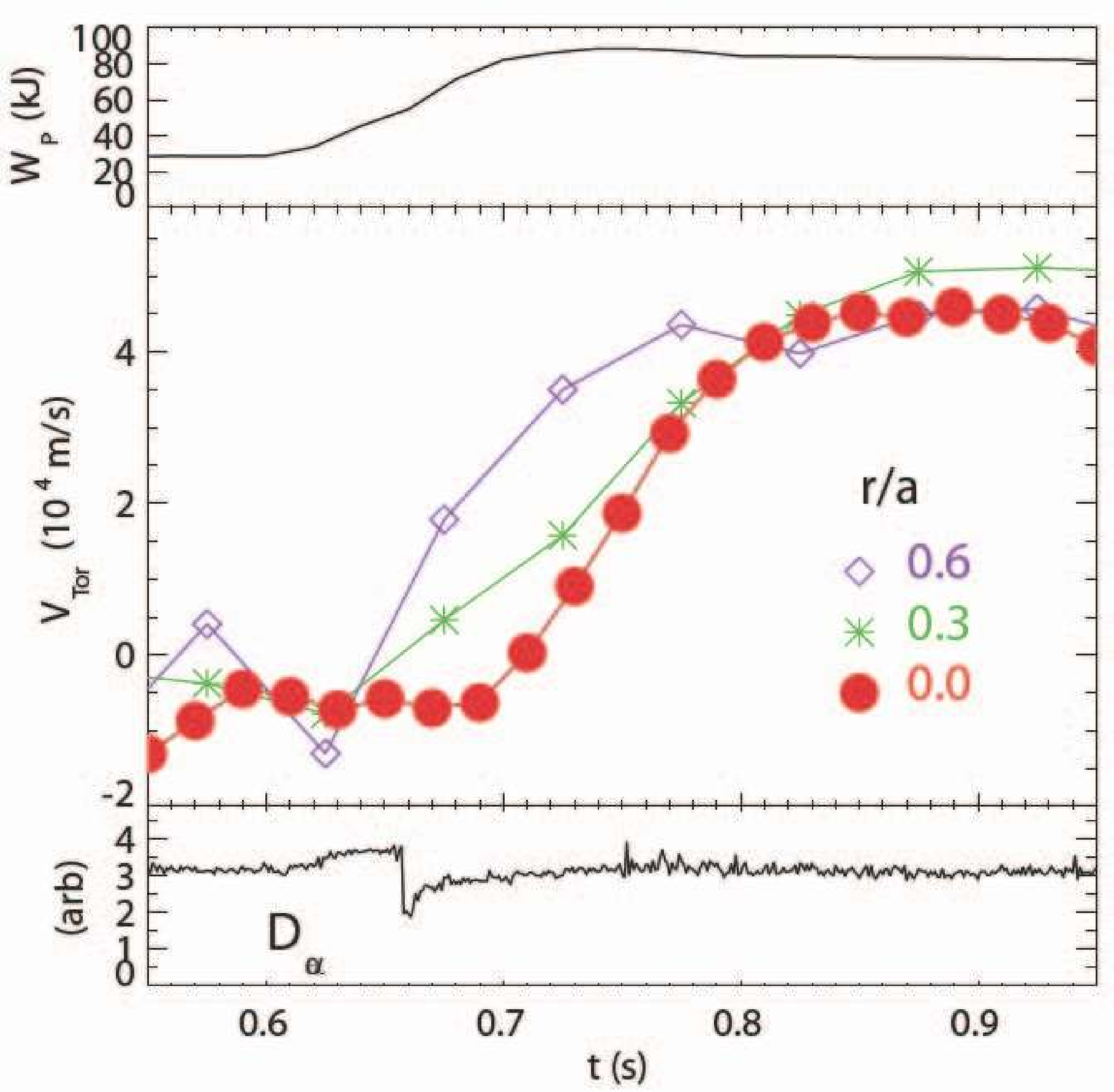

FIG. 31. The plasma stored energy, toroidal rotation velocity at four radii measured by X-ray crystal spectroscopy, and D_α emission in an Alcator C-Mod discharge. The onset of toroidal rotation with no external momentum input following the transition into the EDA H-mode (indicated by the drop in the D_α emission) is clear. (From Rice *et al.*[222]. Reprinted with permission from the International Atomic Energy Agency.)

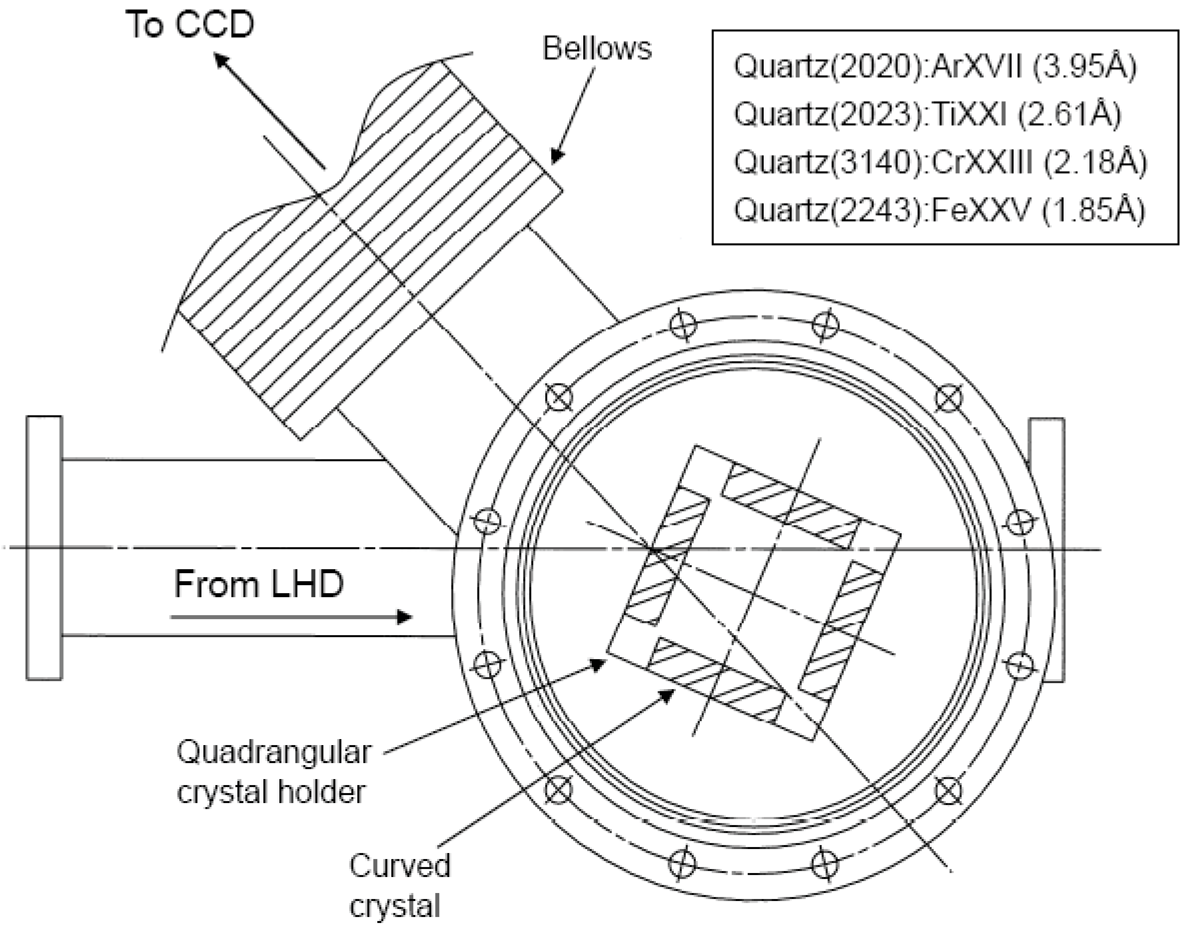

FIG. 32. Schematic of X-ray crystal spectrometer on LHD. (From Morita and Goto.[244] Reused with permission from S. Morita, Review of Scientific Instruments, **74**, 2375 (2003). Copyright 2003, American Institute of Physics.)

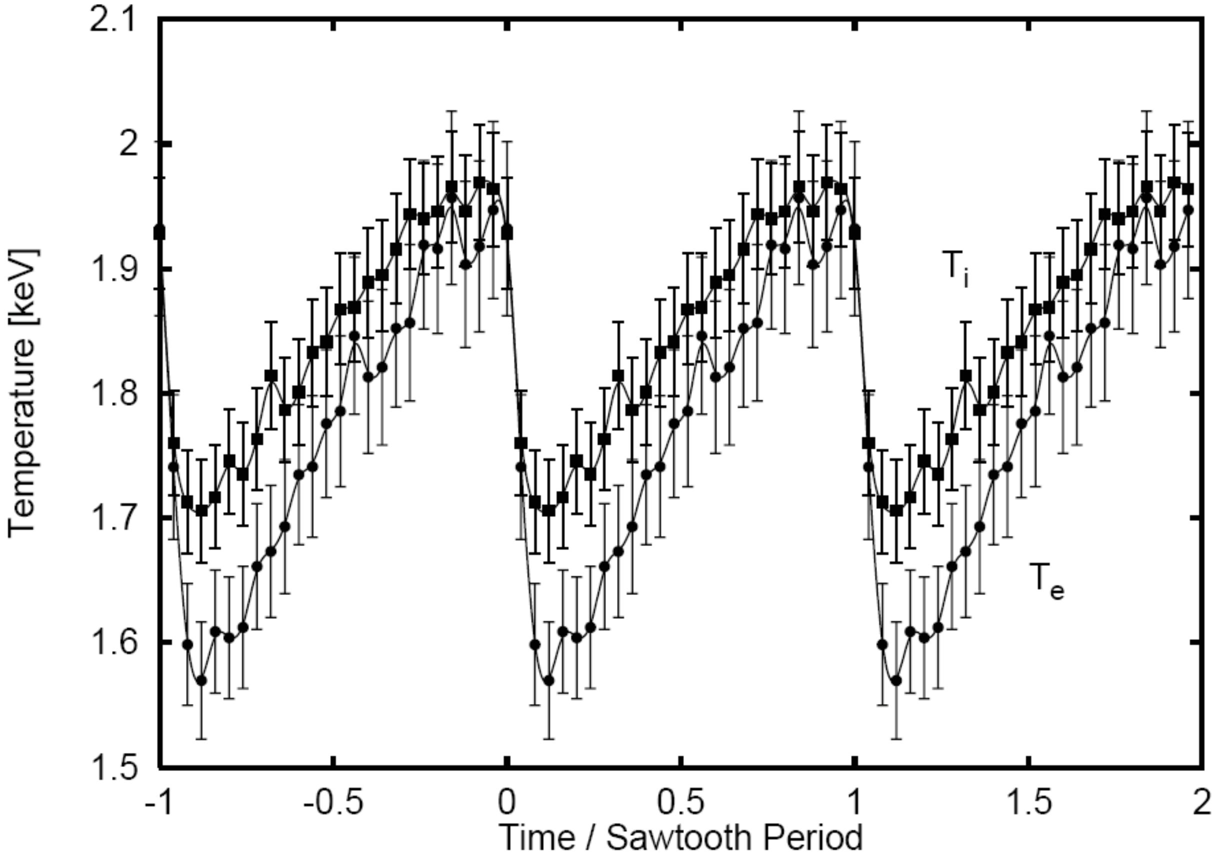

FIG. 33. Time evolution of ion temperature measured by X-ray spectroscopy during sawteeth on TEXTOR-94. (From Bertschinger *et al.*[248] Reprinted with permission of Institute of Physics Publishing.)

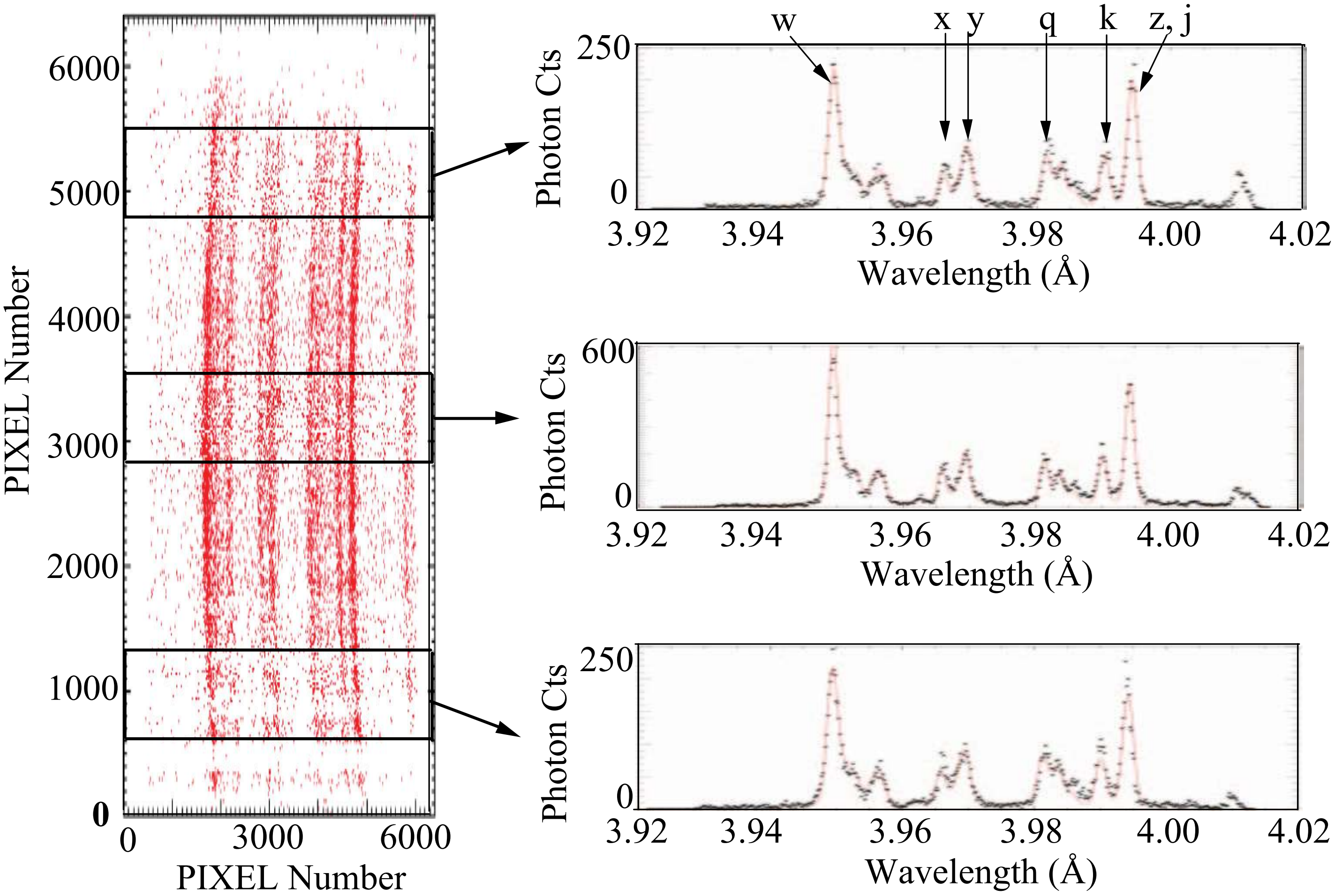

FIG 34. Spatially resolved spectrum of Ar^{16+} from imaging X-ray crystal spectrometer on NSTX.

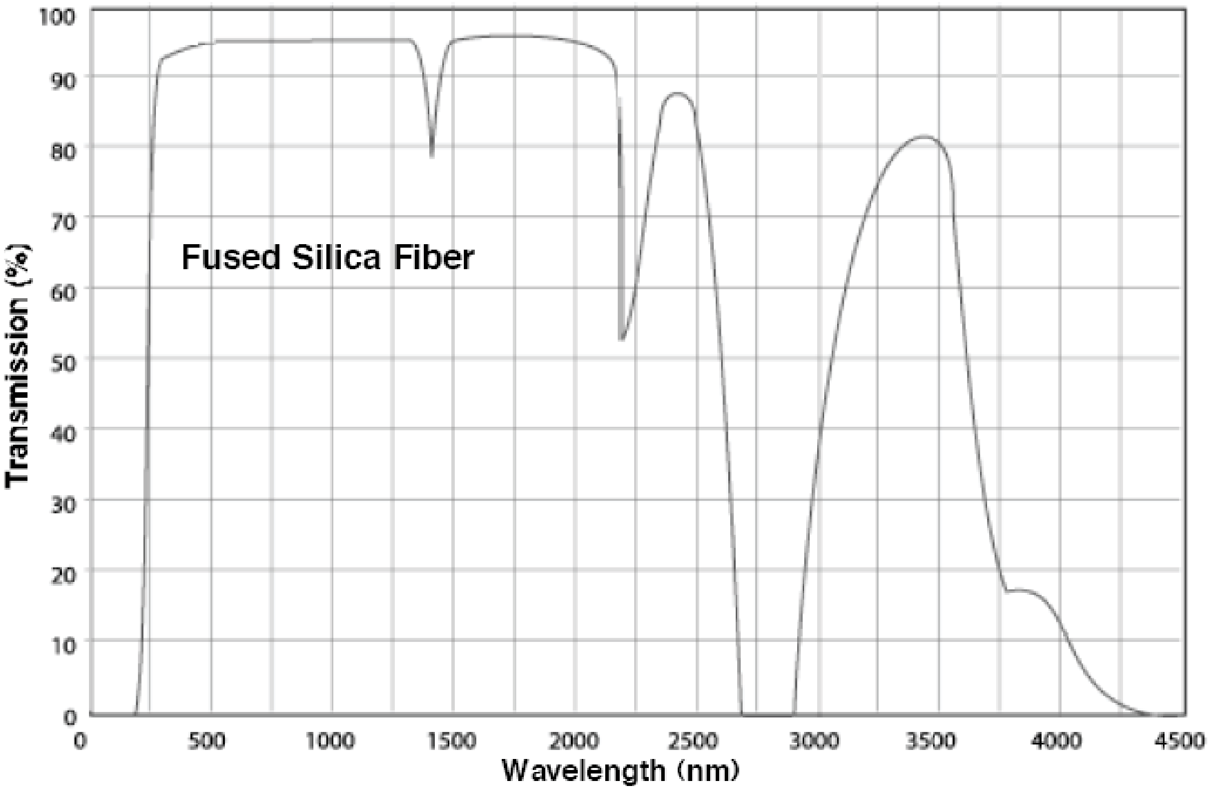

FIG. 35. Transmission curve of a fused silica optical fiber versus wavelength.

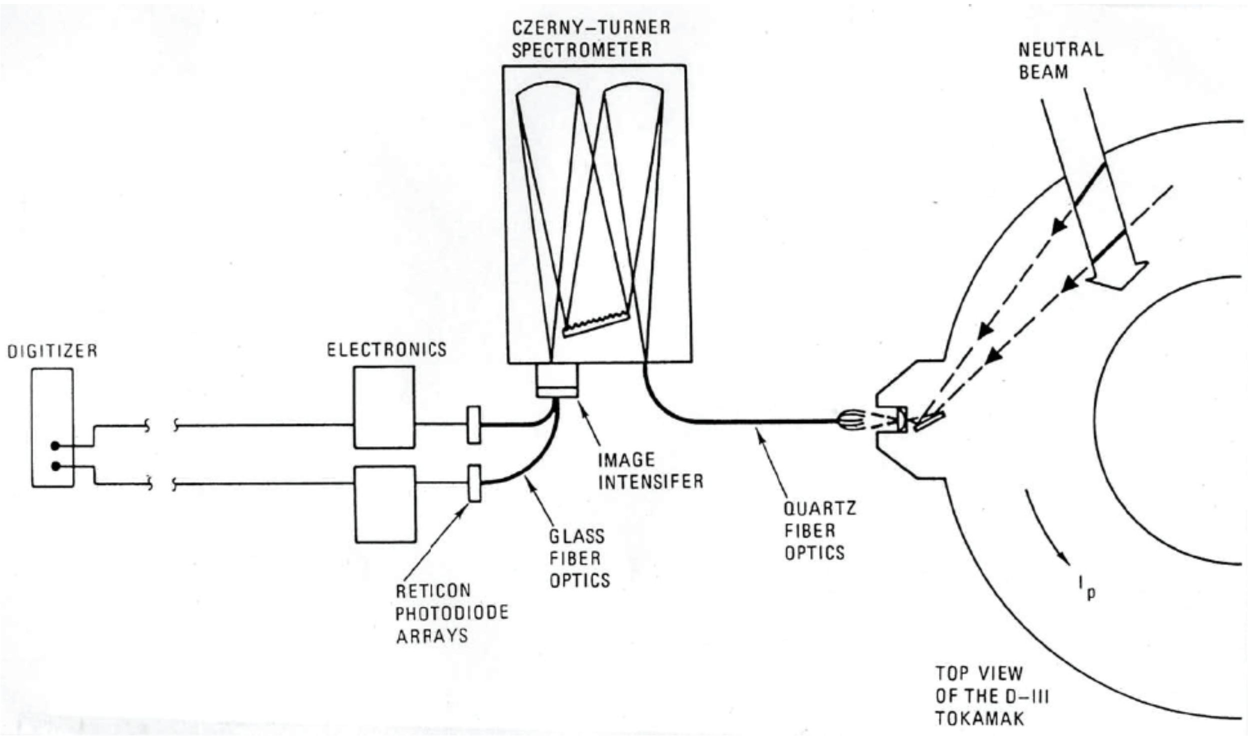

FIG. 36. The use of fiber optics, a Czerny-Turner spectrometer, and a photodiode detector array to view impurities on DIII-D. (From Seraydarian *et al.* [298] Reused with permission from R. P. Seraydarian, Review of Scientific Instruments, **57**, 155 (1986). Copyright 1986, American Institute of Physics.)

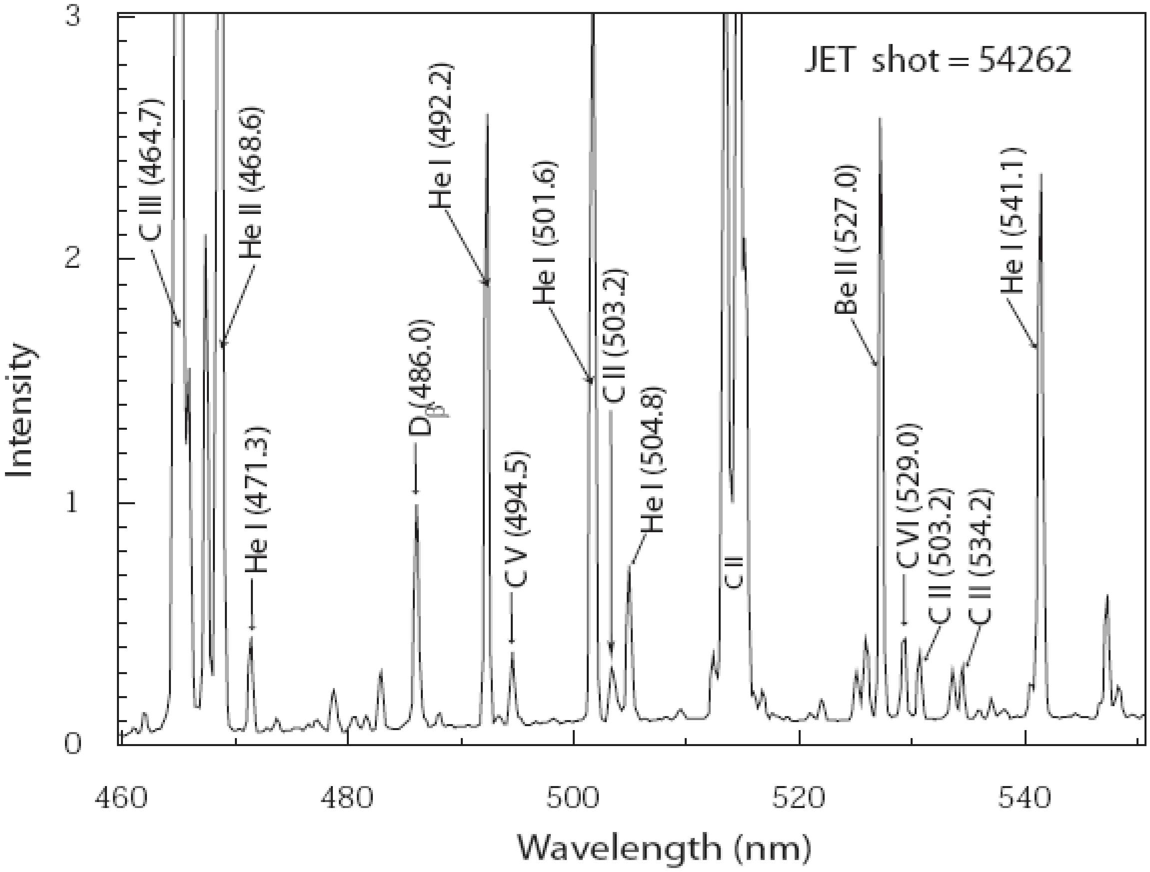

FIG. 37. A typical spectrum from a Helium discharge in JET with wall materials of Be and Carbon. (Figure courtesy of M. Stamp.[300])

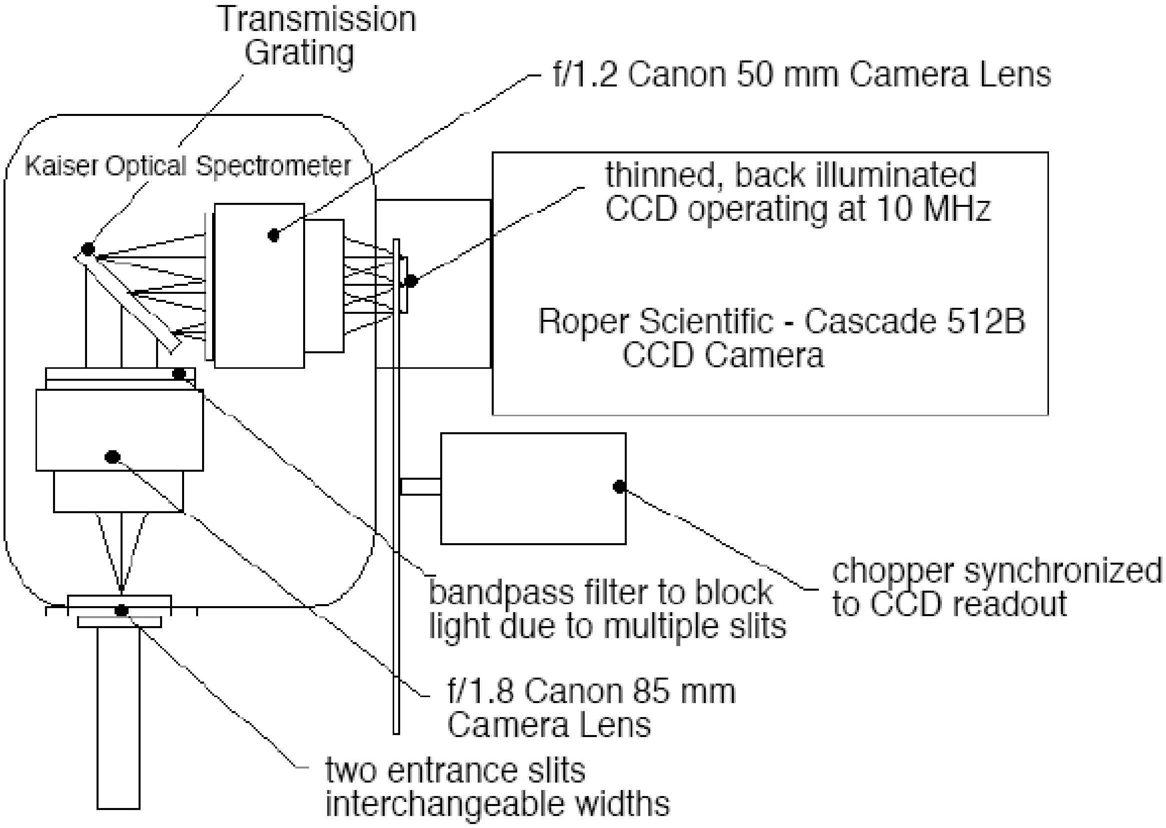

FIG. 38. Schematic of high-throughput transmission grating spectrometer, chopper wheel, and CCD detector (From D. L. Hillis *et al.*[305] Reused with permission from D. L. Hillis, Review of Scientific Instruments, **75**, 3449 (2004). Copyright 2004, American Institute of Physics.)

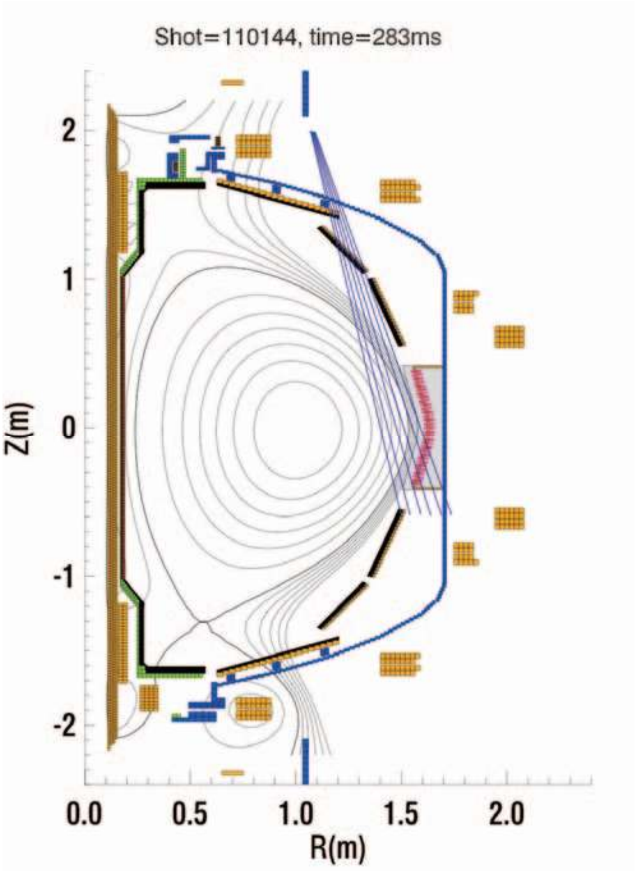

FIG. 39. Poloidal cross section of the NSTX vacuum vessel showing magnetic surfaces and the poloidal edge rotation diagnostic sightlines. (From T. M. Biewer *et al.*[306] Reused with permission from T. M. Biewer, Review of Scientific Instruments, **75**, 650 (2004). Copyright 2004, American Institute of Physics.)

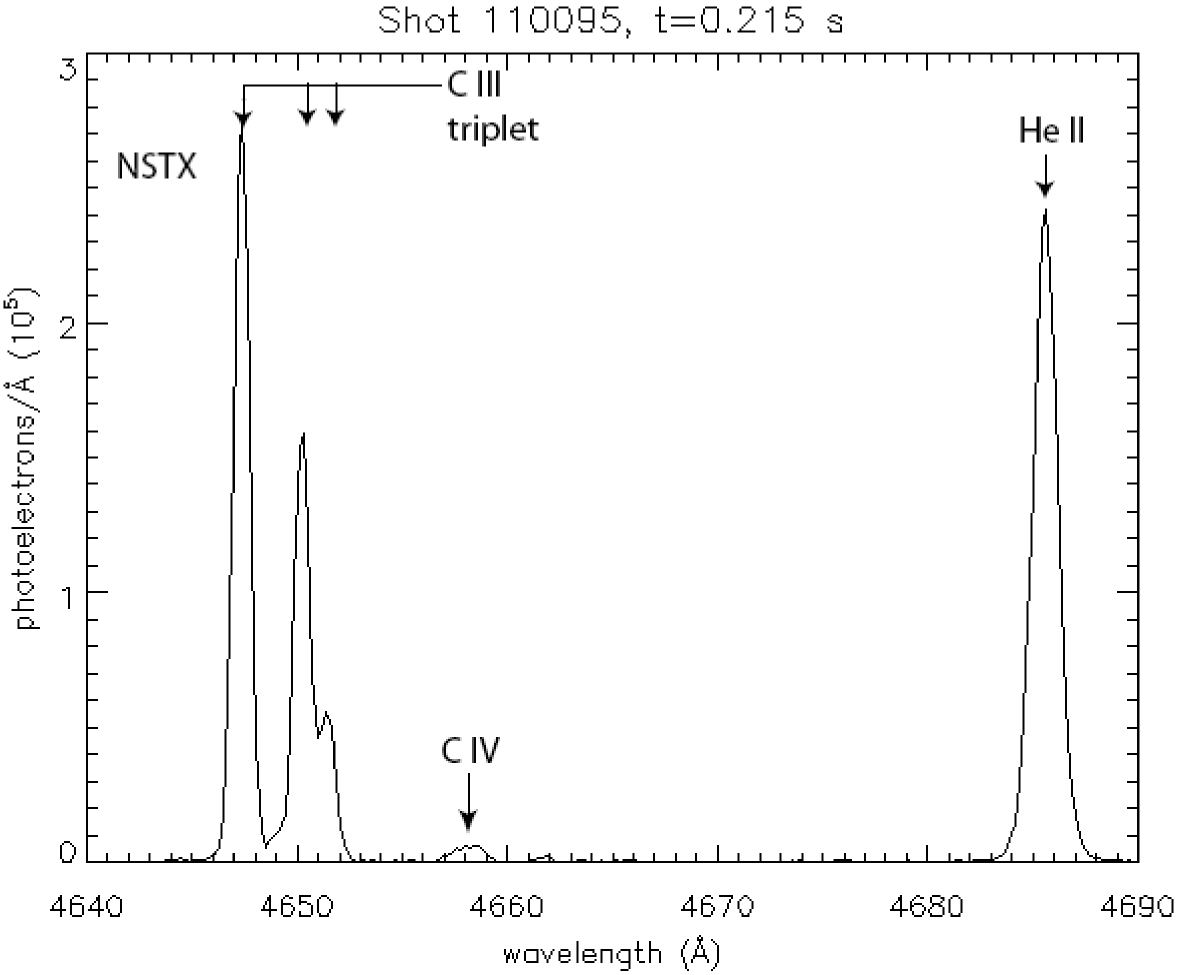

FIG. 40. Sample spectrum from the edge region of NSTX. (From T. M. Biewer *et al.*[306] Reused with permission from T. M. Biewer, Review of Scientific Instruments, **75**, 650 (2004). Copyright 2004, American Institute of Physics.)

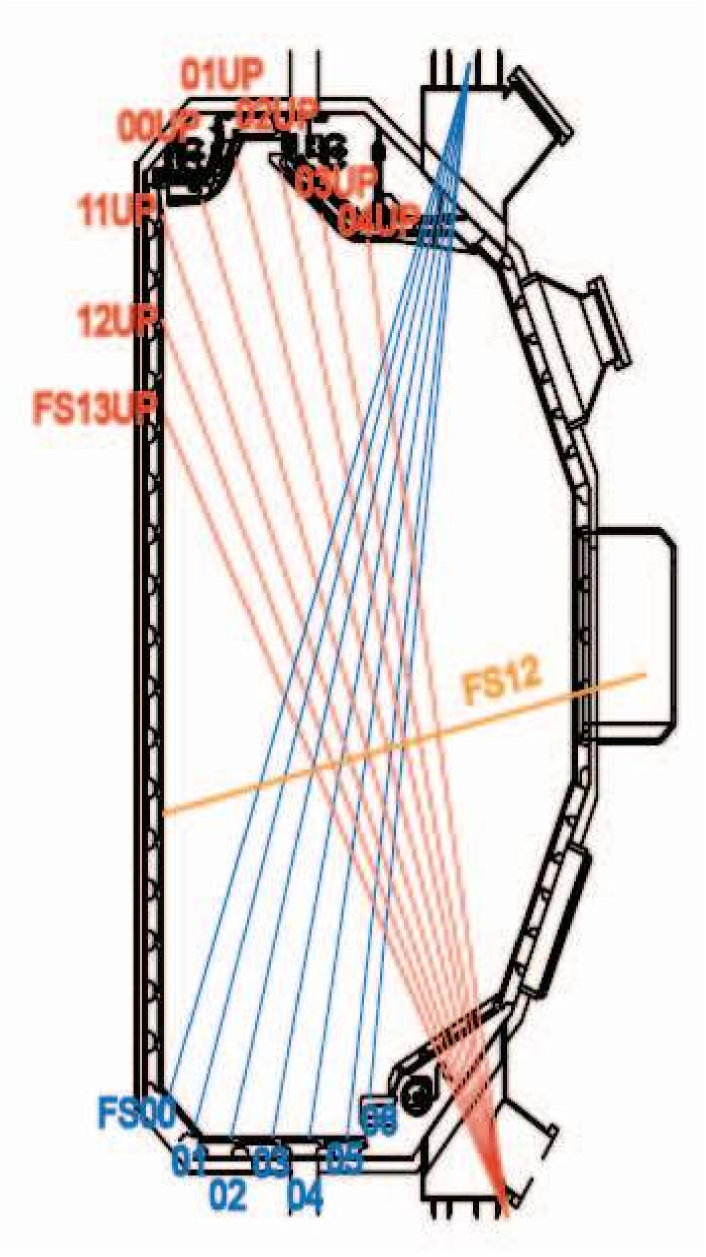

FIG. 41. Arrangement of the filterscope sight lines on the DIII-D tokamak. Lower divertor sightlines end on the lower carbon tiles, and upper divertor sightlines on the upper tiles. One view (FS12) is directed toward the inner wall. (From R. J. Colchin *et al.*[323] Reused with permission from R. J. Colchin, Review of Scientific Instruments, **74**, 2068 (2003). Copyright 2003, American Institute of Physics.)

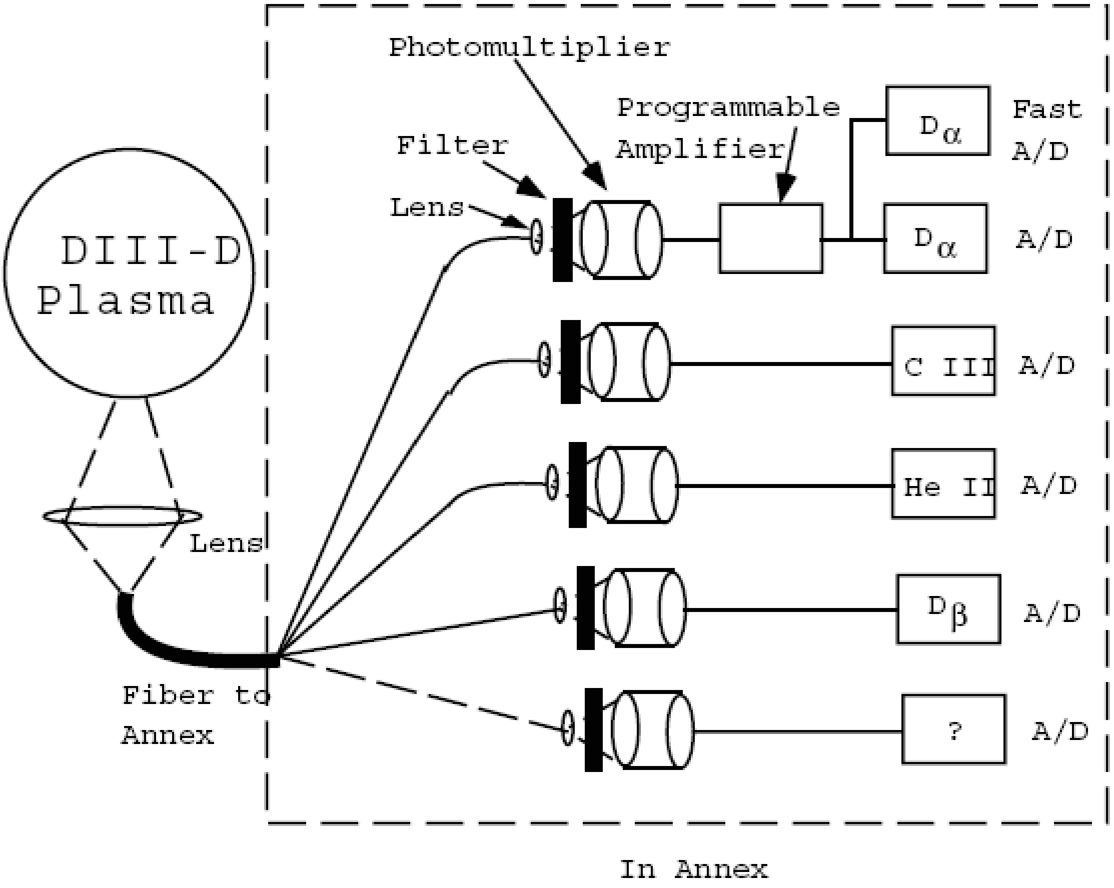

FIG. 42. Schematic of the filterscope system for one optical fiber. Light imaged from the plasma into one fiber is subsequently split 5 ways and filtered by optical band-pass filters. Light from the filters is sensed by photomultipliers and the resulting signal is converted to digital data. The fifth channel is a spare. (From R. J. Colchin *et al.*[323] Reused with permission from R. J. Colchin, Review of Scientific Instruments, **74**, 2068 (2003). Copyright 2003, American Institute of Physics.)

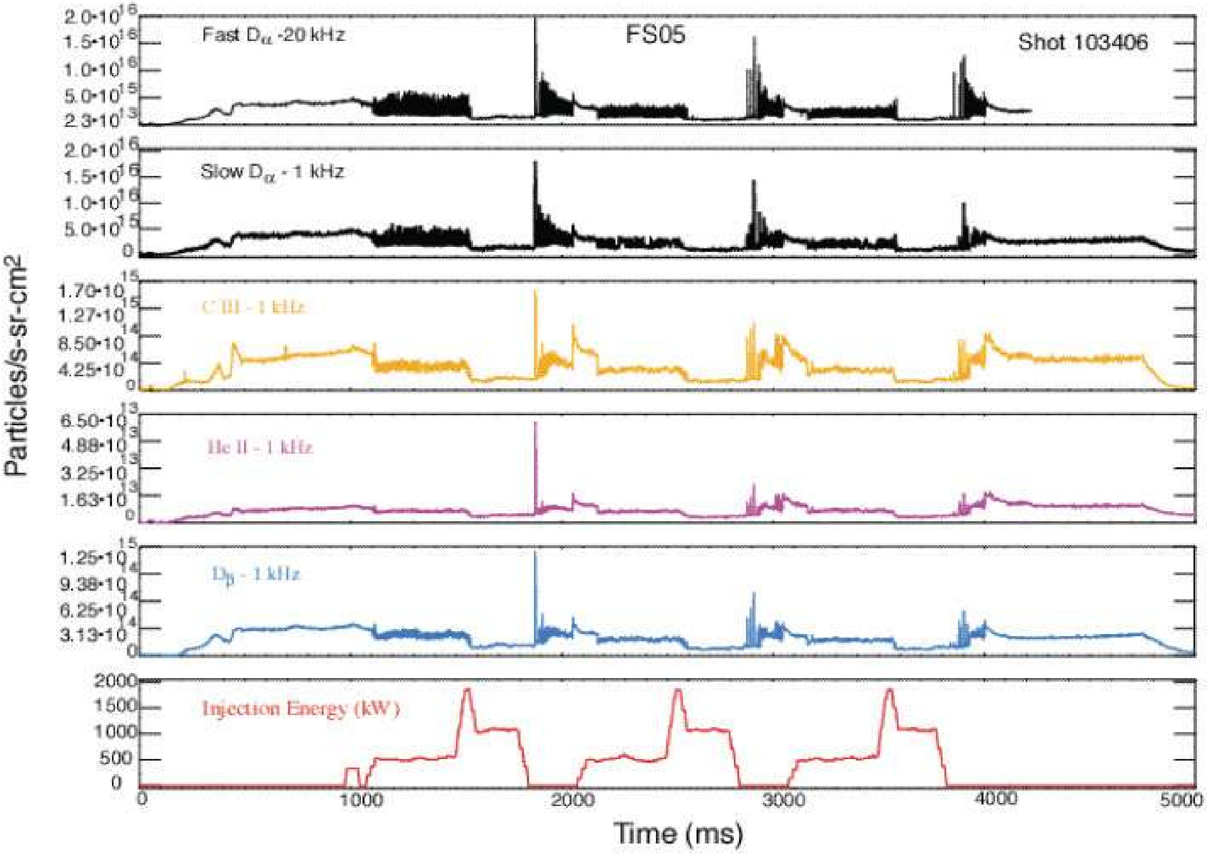

FIG. 43. Divertor Filterscope signals from a single viewing chord on DIII-D. Both slow and fast D_α are acquired, as well as C III, He-II, and D_β line emission. (Figure courtesy R. J. Colchin.[327])

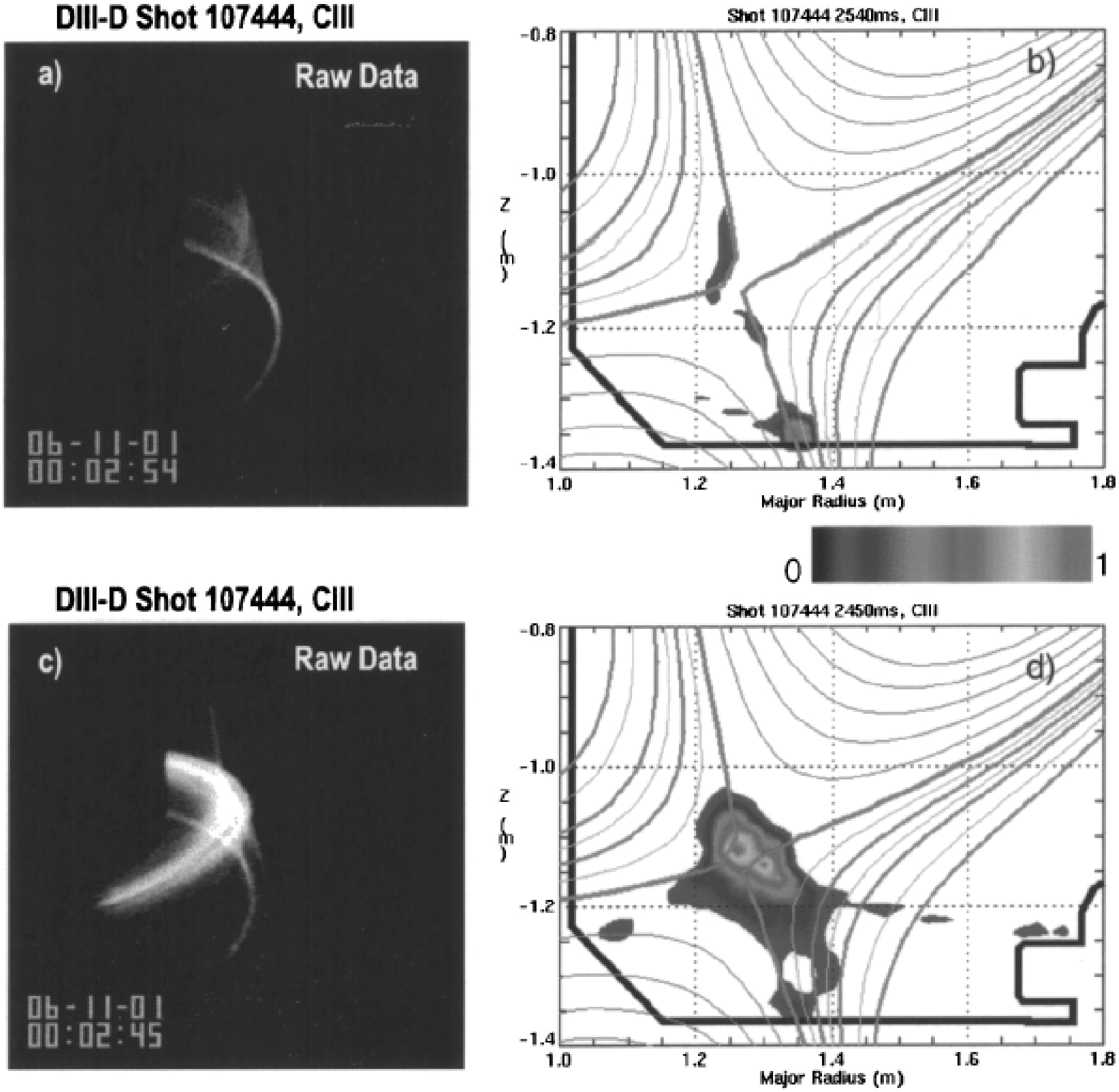

FIG. 44. Variation of the C-III emission during the ELM evolution. The 3-D image data (a,c) were taken at different times during the ELM cycle. The reconstructed 2-D poloidal emission profiles (b,d) imply an attached divertor plasma (b) and a detached divertor plasma (d). (From M. Groth *et al.*[332] Reused with permission from M. Groth, Review of Scientific Instruments, **74**, 2064 (2003). Copyright 2003, American Institute of Physics.)

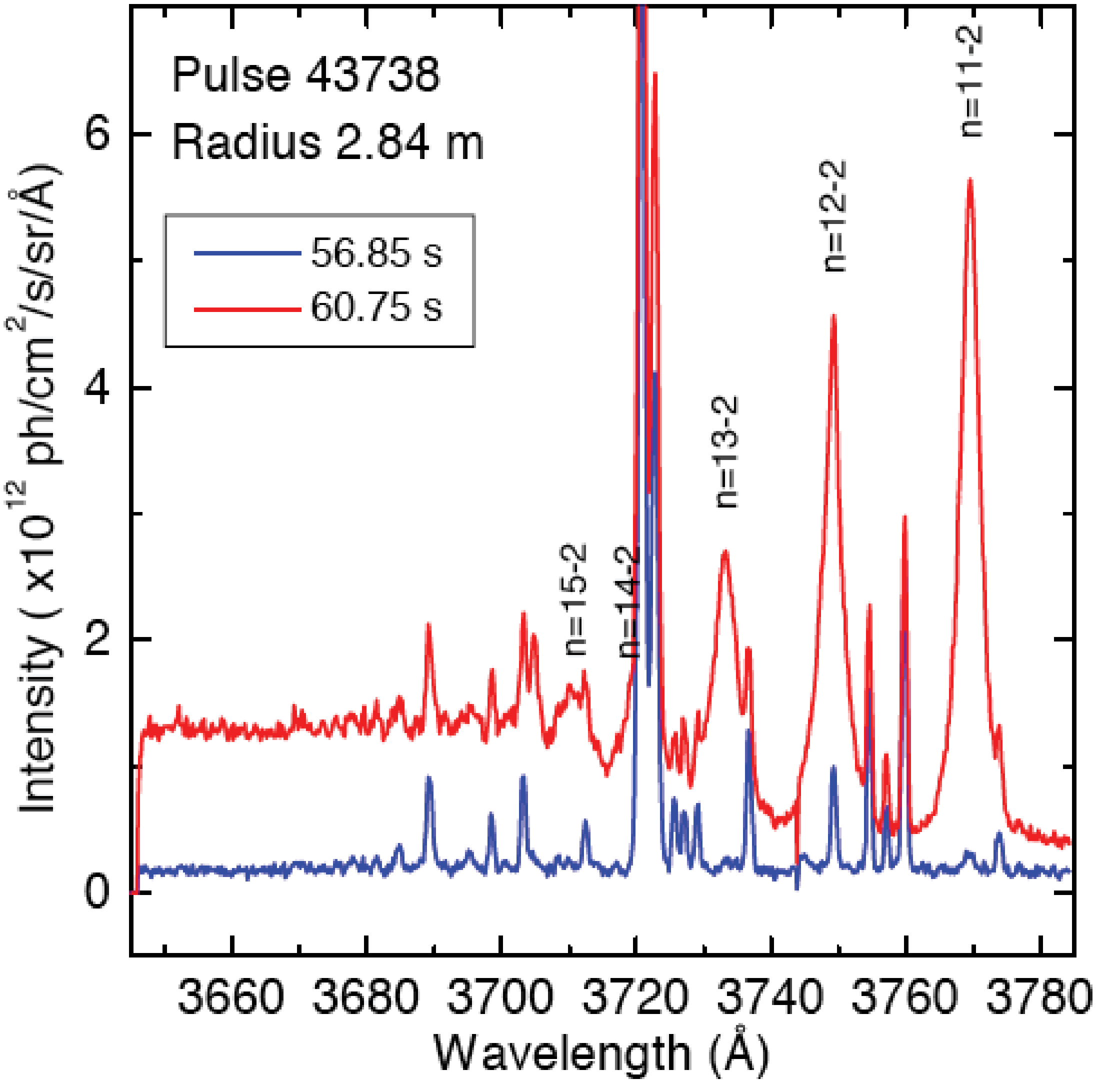

FIG. 45. Spectra from a vertical target L-mode density limit discharge with *PNBI* = 2 MW. n_e is approximately 2.3×10^{19} m^{-3} for low recombination (56.95 s, lower curve) and 3.5×10^{19} m^{-3} for high recombination (60.75 s) spectra. (Figure from A. Meigs *et al.*[352])

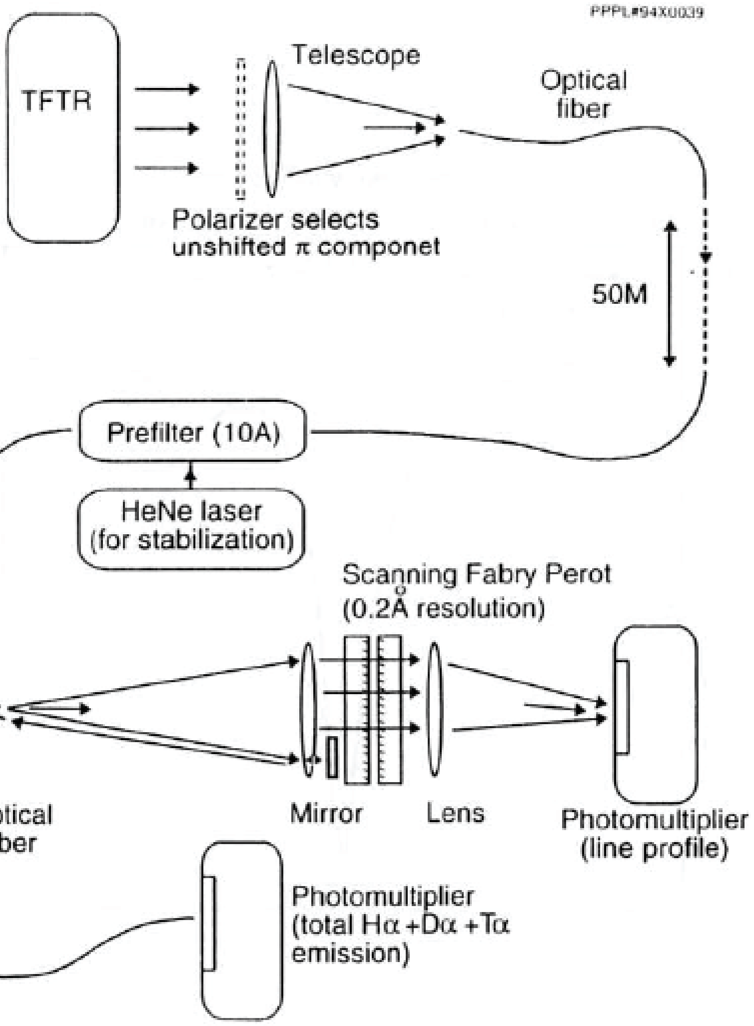

Fig. 46. Experimental arrangement for TFTR Fabry-Perot spectrometer for H_α, D_α, and T_α recycling measurements. (From Skinner *et al.*[344] Reused with permission from C. H. Skinner, Review of Scientific Instruments, **66**, 646 (1995). Copyright 1995, American Institute of Physics.)

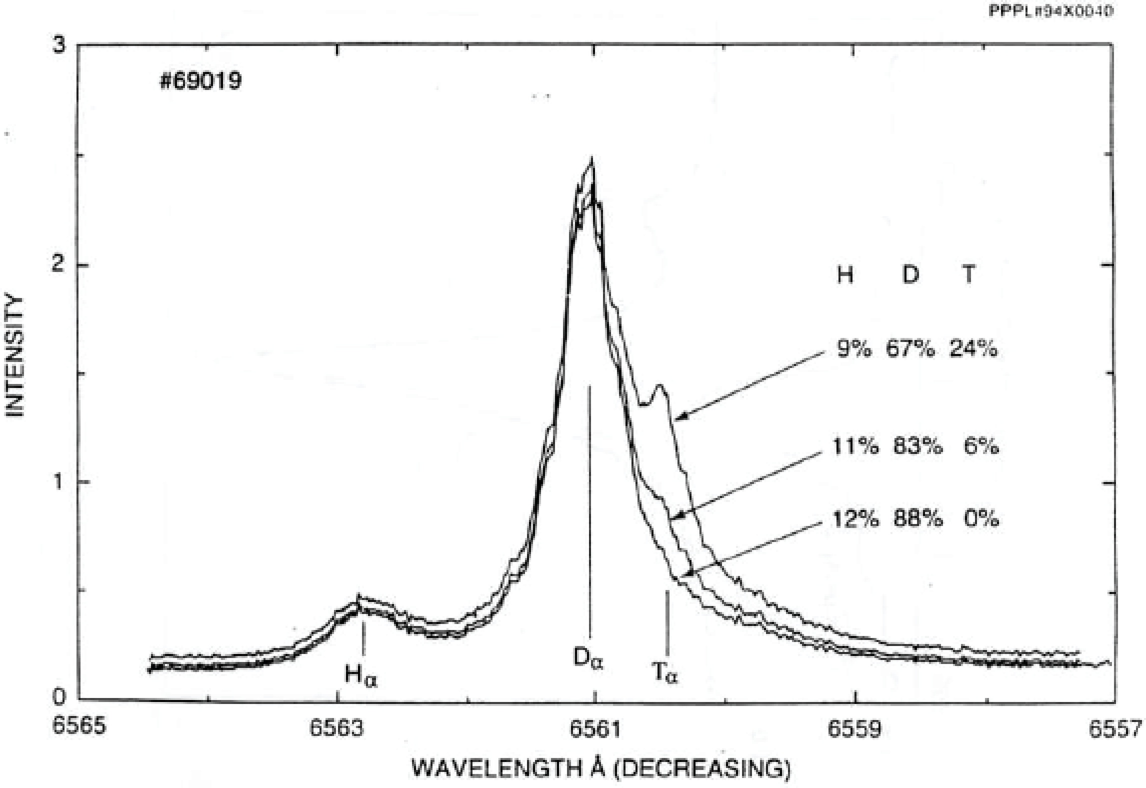

Fig. 47. The lowest trace is the Hα and Dα spectrum observed in TFTR before tritium operations. The upper traces simulate the addition of 6% and 24% Tα , respectively. (From Skinner *et al.*[344] Reused with permission from C. H. Skinner, Review of Scientific Instruments, **66**, 646 (1995). Copyright 1995, American Institute of Physics.)

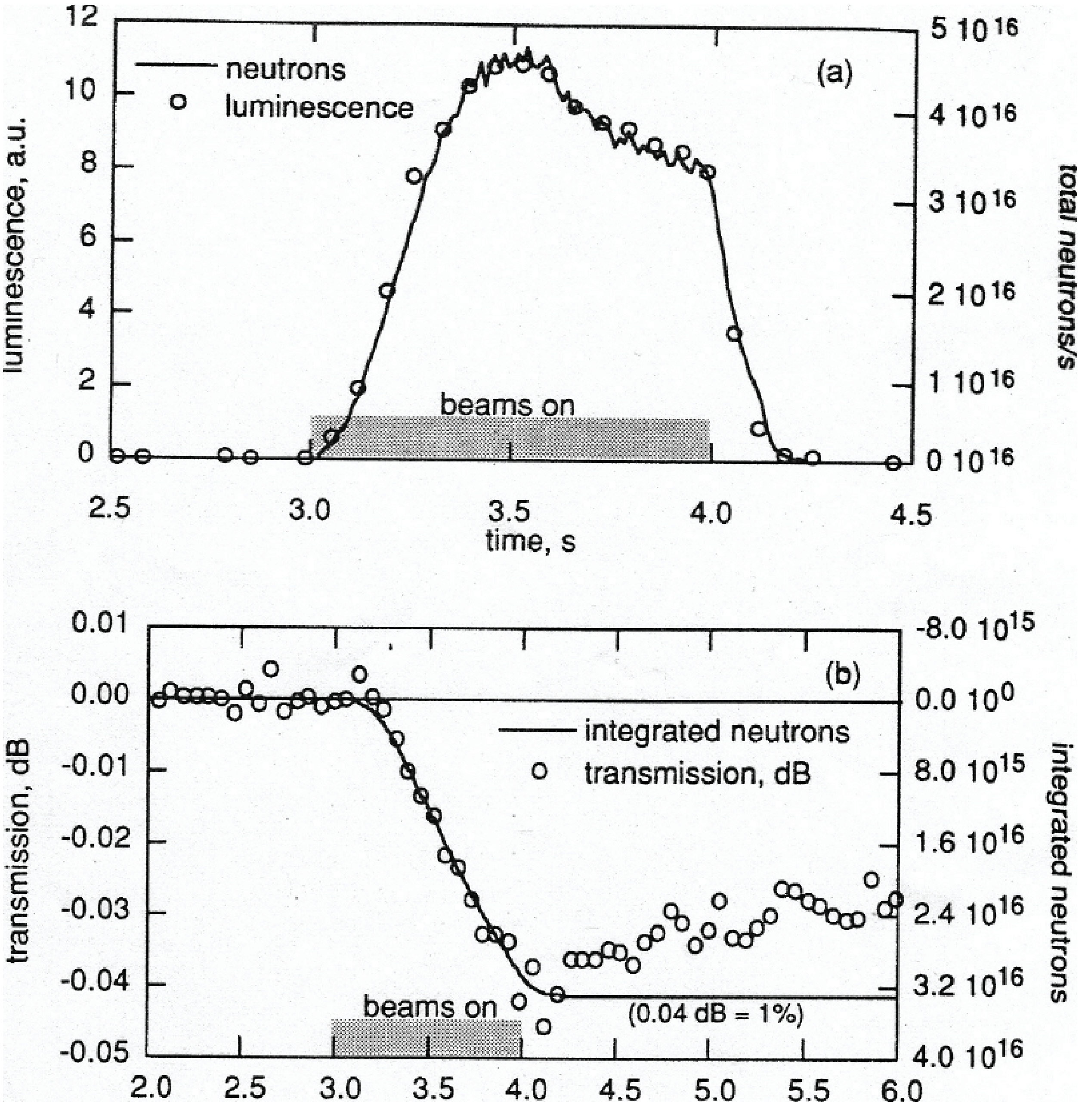

Fig. 48. Luminescence and transmission loss in an optical fiber during a DD plasma discharge. (a) shows the luminescence overlaid with the total neutron production rate. (b) shows the loss of transmission with the integrated neutron rate. (From Ramsey.[356] Reused with permission from A. T. Ramsey, Review of Scientific Instruments, **66**, 871 (1995). Copyright 1995, American Institute of Physics.)

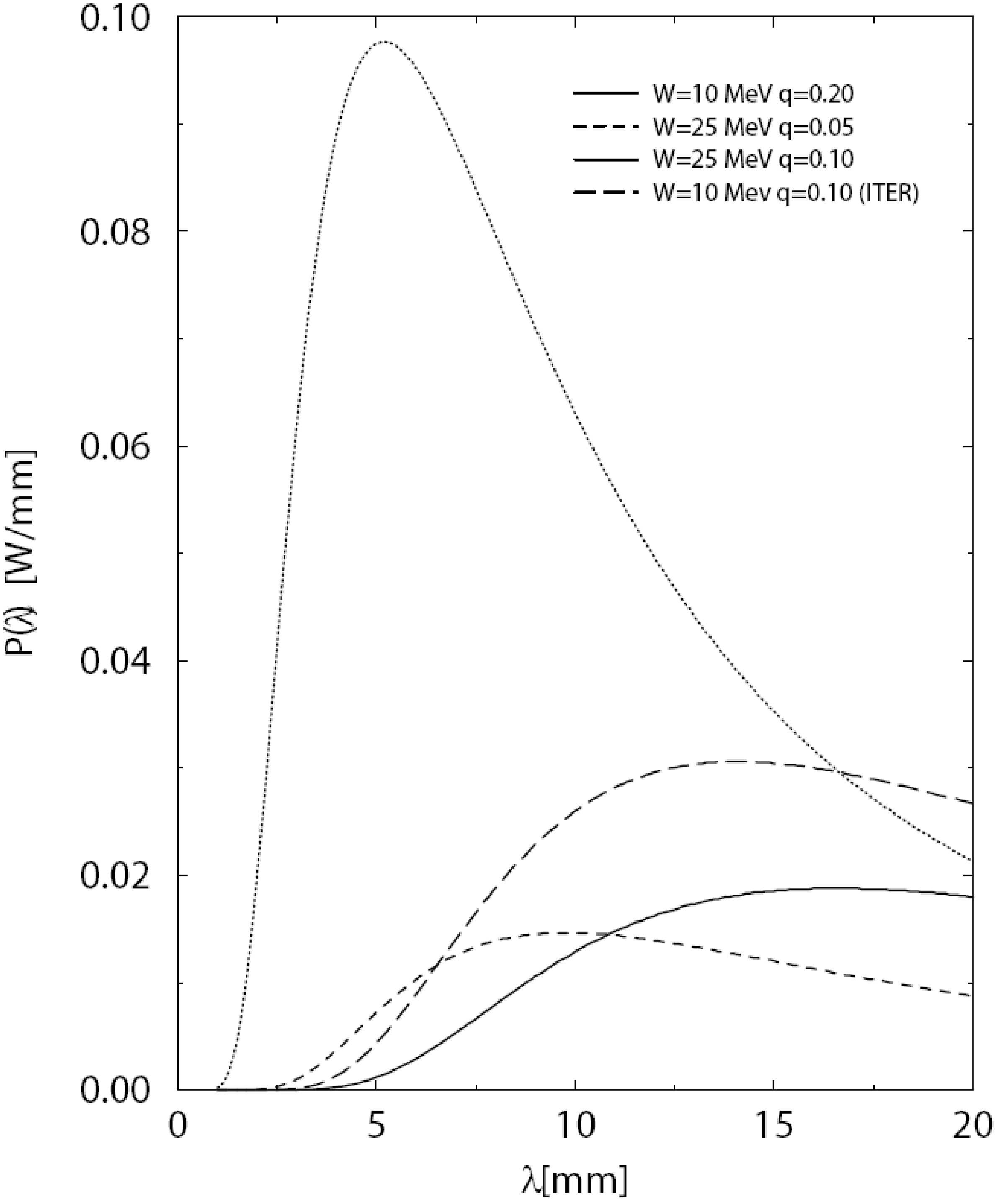

FIG.49. Synchrotron radiation spectrum for a single electron calculated for TEXTOR-94 and for ITER for various values of the electron energy, w, and pitch angle, θ. (From R. Jaspers *et al.*[367] Reused with permission from R. Jaspers, Review of Scientific Instruments, **72**, 466 (2001). Copyright 2001, American Institute of Physics.)

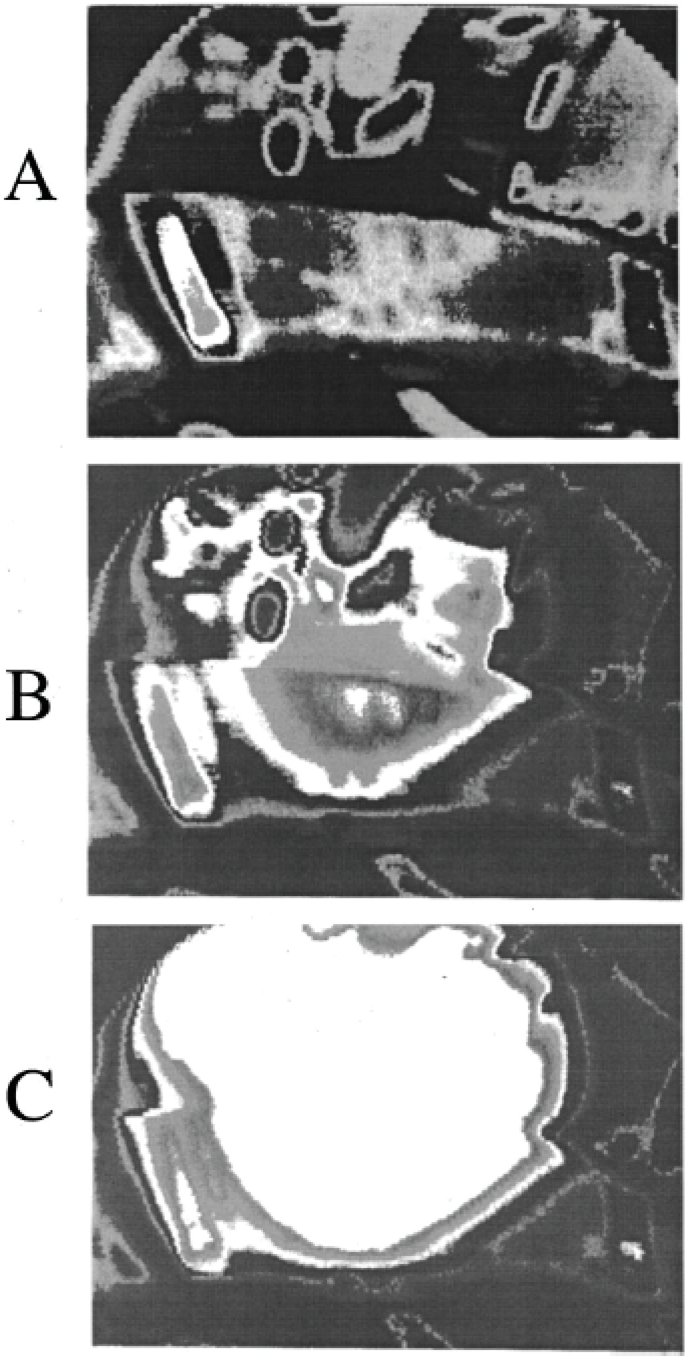

FIG. 50. Images obtained using a tangentially-viewing infrared camera during a low-density discharge in TEXTOR-94. (A): before the runaway electron population developed showing emission from plasma-facing surfaces. (B): early development of runaway electron population. (c): runaway electron population fully developed. (From R. Jaspers *et al.*[367] Reused with permission from R. Jaspers, Review of Scientific Instruments, **72**, 466 (2001). Copyright 2001, American Institute of Physics.)

The Princeton Plasma Physics Laboratory is operated
by Princeton University under contract
with the U.S. Department of Energy.

Information Services
Princeton Plasma Physics Laboratory
P.O. Box 451
Princeton, NJ 08543

Phone: 609-243-2750
Fax: 609-243-2751
e-mail: pppl_info@pppl.gov
Internet Address: http://www.pppl.gov